An Analysis of the Stability of Deep Drilling Systems

A DISSERTATION
SUBMITTED TO THE FACULTY OF THE GRADUATE SCHOOL
OF THE UNIVERSITY OF MINNESOTA
BY

Carlos Eduardo da Fonseca

IN PARTIAL FULFILLMENT OF THE REQUIREMENTS
FOR THE DEGREE OF
MASTER OF SCIENCE

ADVISER
Emmanuel Detournay

CO-ADVISER
Nathan van de Wouw

July, 2015

Acknowledgements

First of all, I want to express my sincere gratitude to Petróleo Brasileiro S.A - Petrobras, which supported in many ways my travel to the Minneapolis, and my time at the University of Minnesota.

My sincere thanks to my adviser Prof. Emmanuel Detournay for the continuous support, patience, and understanding about everything that had happened during these two years. Also, my sincere thanks to my co-adviser Prof. Nathan van de Wouw, who was always ready to teach and help.

Also I have to thanks my new friends. Anna Liakou, who helped me a lot during my first semester as a student, and throughout my entire journey. To Julien Marck, for the uncountable number of great discussions we had. To Yaneng Zhou, who always inspired me to be a nicer person. And Kaixao Tian, who joined us recently, and has been a wonderful person.

I can not forget about the great number of people who I met and helped me to make the Minnesota weather more enjoyable. Even though their names are not listed here, they will always be part of my memories and my life. And last but not least, my family and friends in Brazil, who has been supporting and waiting for us.

Dedication

I dedicate my dissertation to my family, who accepted the challenge to change to a completely new life. My wife Fabiana, who came with the compromise of bringing our new baby to us. Gabriel, who had no idea what was about to come, and enjoyed it a lot. And Julia, who just arrived within this time in Minneapolis.

My family dedicate this journey to my dad, José Geraldo, who left before we came to Minneapolis.

Also my family dedicate this work to Regina, who left before we went back to Rio de Janeiro.

Abstract

This thesis has focused on analyzing the coupled axial-torsional dynamics of a drilling structure, due to its importance within the drilling activity. This work builds upon earlier published work on the coupled axial-torsional dynamics of drilling systems, which addressed the problem by means of either low-order or finite element models. During the course of this study we realized that the spatial discrete representation of the drilling system plays an important role in the model stability properties; in particular the model tends to become more unstable when it is represented by a larger number of DOF's (i.e. a finer discretization). Ultimately, such a lack of stability can be an inherent property of the drilling system. If the observed instability of the drilling system is indeed an inherent property, only significant changes to the dynamics can provide system stability. Focusing on that aspect, a finite element model was used to investigate the value of the use of a simple (industrial) angular velocity drive system control (Soft Torque) to mitigate stick-slip. The Soft Torque controller can be represented by a spring-dash pot surface boundary condition which is tuned to damp the first torsional natural frequency of the drill string. From the results in the thesis, it can be concluded that the coupled axial-torsional dynamics, with the bit/rock interface, cannot in general be stabilized by the Soft Torque controller. This is likely to be related to the fact that higher modes of the drill-string dynamics play a role in instabilities leading to stick-slip oscillations. Motivated by this observation, this study took on the challenge of investigating which level of discretization provides and accurate description in the dynamics.

To understand the role of spatial discretization of the drill-string dynamics, discrete models were developed to understand stability properties and to study the overall time-domain behavior. Based on a time scale separation argument (between the axial and torsional dynamics), 1-DOF, 2-DOF, and multi-DOF lumped parameter models describing only the axial dynamics of the drill-string were studied. Subsequently, the coupled dynamics of one and two identical oscillators were investigated. In all cases, the increasing number of oscillators led to a more unstable system.

Contents

List of Tables

List of Figures

Chapter 1

Introduction

Wellbore construction is one the most expensive investment in oil and gas production, and thus makes it an important activity throughout the exploitation chain. Construction of a wellbore consists of three main tasks: (1) drilling (removing rock down to the hydrocarbon reservoir), (2) casing (protecting the wellbore previously drilled with pipes), and (3) completion (installing suitable equipment for hydrocarbon production control) [7, 13, 28].

To drill a well, the surface drive system imposes axial and angular velocities at the drill pipe (DP) top end, which are transmitted to the bit. In the lower section of the drill string, thicker pipes (drill collars) push the bit downward and are the main features in the bottom hole assembly (BHA). Figure 1.1.1 shows a typical drilling site with drive system, drill string (DP and BHA), and the bit.

1.1 Drilling Dynamics

Classically, the vibration modes of the drill string and of the bit are classified as bit bounce, stick-slip, and whirl. Bit bounce is characterized by a loss of contact between the bit and the rock, due to axial vibrations. Stick-slip is a particular torsional oscillatory pattern. During the bit stick phase, the bit stops rotating due to the bit/rock reaction torque, while the drive system still imposes rotation to the top of the drill string. When the drill-string torque overcomes the

resisting bit/rock torque, the bit and drill string accelerate sharply in the slip phase leading to high torsional velocity. Whirl is the out-of-center rotation of the bit and drill string due to lateral vibrations; it can be forward or backward compared to the bit rotation orientation. The three modes of vibrations are illustrated in Figure 1.1.1b.

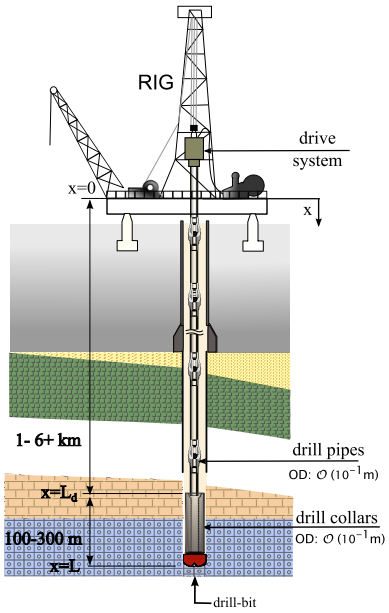

(a)

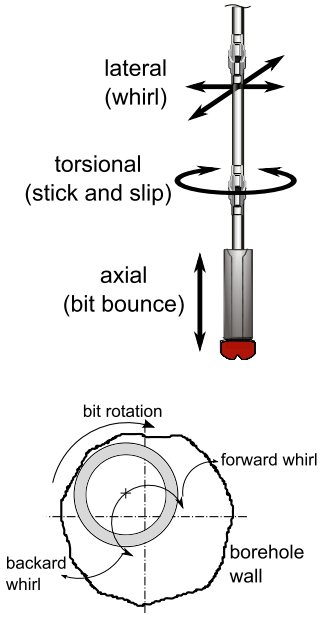

(b)

Figure 1.1.1: Drilling system dynamics: (a) Simplified drilling system including driving system, drill pipes, drill collars (BHA), and drill bit. The reference system is fixed at the surface and points downward; relevant characteristic dimensions are presented. (b) Schematics showing the modes of vibrations (top), bore hole cross section with forward and backward whirl path (bottom). The sketches are not to scale and bit and drive system are in reality small compared to the drill string length.

The development of downhole data acquisition sensors has been the key to understand drilling

dynamics, as well as the coupling between weight-on-bit (WOB) and torque-on-bit (TOB). In the pioneering efforts described in [62], the downhole sensor was capable of measuring the WOB and the triaxial accelerations. During field tests, the measured WOB fluctuations (due to axial vibrations) were at lower frequencies than the first axial natural frequency of the drill string, and the expected resonance did not occur. Moreover, under these conditions the magnitude of the WOB increased slowly and dropped down abruptly, as can be seen in Figure 1.1.2b. This response does not suggest that the drill string is vibrating in its first natural mode. The authors recognized that the bit/rock interface was the key to explain this difference, and suggested that the overall system dynamics, including bit/rock interaction, had lower natural frequency than the drill string itself.

Figure 1.1.2a shows sensor data recorded during the test, and Figure 1.1.2b depicts a detailed correlation between WOB and TOB. When WOB dropped down to zero, the accumulated drill string torque was released, with backward rotation in some occasions (negative torque). With the engaged bit, *i.e.* increasing WOB, the torque started building up again. Another important observation is that no significant lateral acceleration (bending moment) was measured, even though there were high axial and angular (tangential) accelerations.

Figure 1.1.2a also shows that under high WOB (and TOB) fluctuations, the bending moment remained almost constant. Bending moment is a direct measure of lateral vibrations (whirl), and is not associated with high WOB fluctuations, suggesting that these modes of vibrations are not coupled. Therefore, axial and torsional motion must be coupled to understand overall system dynamics. But lateral vibrations are not important for those modes.

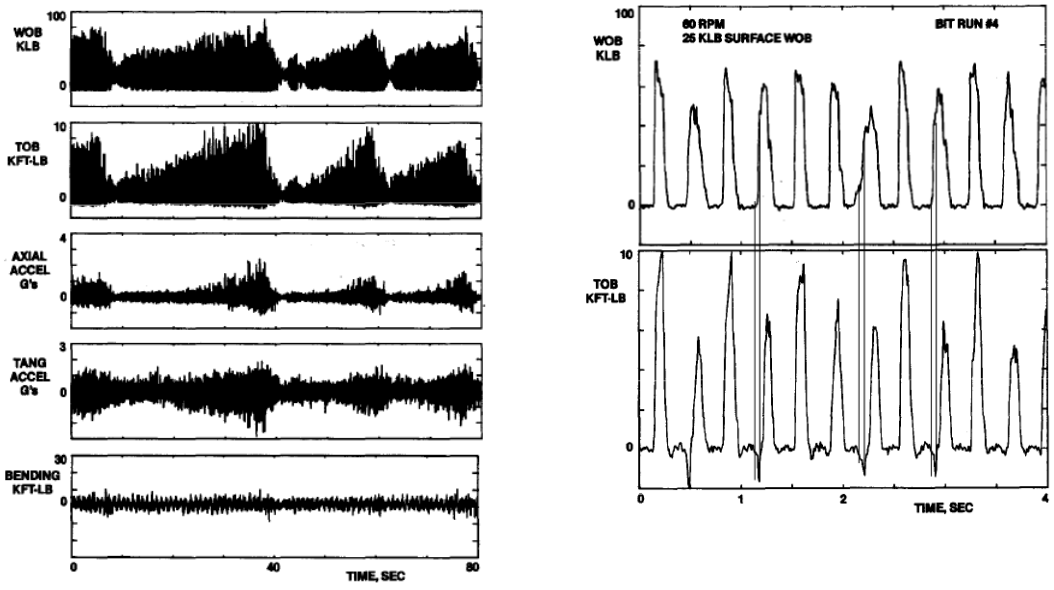

(a)

(b)

Figure 1.1.2: Downhole measurements (from [62]): (a) shows sensor data record, and (b) shows that WOB and TOB are related between each other.

Many authors have explored the importance of drilling dynamics in oil and gas wells drilling [14, 46, 43, 61]. Some have related drilling dynamics to BHA failures [14, 46, 43, 61], or highlighted the opportunity of increasing rate of penetration (ROP) with proper vibration management [25], as depicted in Figure 1.1.3a.

In [61], the authors analyzed data gathered from drilling operations between 2003 and 2005 in 44 locations worldwide, together representing 15 million feet of drilled hole. Vibration was pointed out as the main root cause for failure for 385 analyzed cases, representing 23% of all reported failures. Within all cases 13% of failures did not have a clear indication of the root cause, and debris representing only 6% was the second most important cause. A summary of main root causes of BHA failure is depicted in Figure 1.1.3b, which shows the importance of an effective vibration mitigation technique.

Hence, large vibrations directly impact drilling performance by causing unplanned delays to replace BHA components or reducing ROP. Therefore, this thesis addresses the challenge of modeling and analyzing drill string dynamics, in particular the coupled axial-torsional motions, to support further understanding of the mechanisms involved in the generation of these vibrations. A concise overview of existing work related to the study of stick-slip is given in the next section.

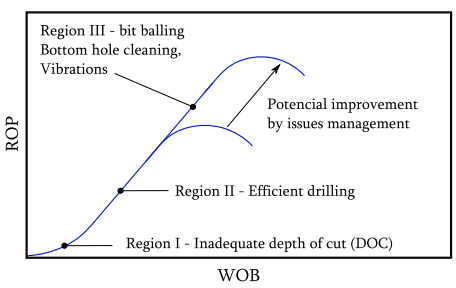

(a)

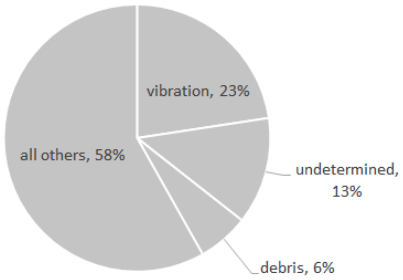

(b)

Figure 1.1.3: Vibration importance in oil and gas wellbore drilling: (a) shows schematic performance improvement by vibration management (adapted from [25]), and (b) main root causes leading to BHA failure. Vibration is the most relevant root causes, and debris is the second identified cause and responsible for only 6% of failures (from [61]).

1.2 Stick-slip Modeling Approaches

Within this sub-section we present the two usual approaches adopted to study drilling dynamics, and in particular the stick-slip phenomena. First we present what we call the classical approach, where the study of stick-slip comes from the adoption of a weakening torque-velocity relationship, which is usually uncoupled from the axial motion. Then we present a model of the self-excited drill string vibrations, which assumes that the bit/rock interface presents a regenerative effect that couples axial and torsional motions.

1.2.1 Weakening torque-velocity relationship

The classical approach to study the stick-slip phenomena has been to assume a bit/rock interface law characterized by a weakening torque-velocity response, as for instance in [15, 59, 24]. In [59] the response is described by a non-linear analytical relationship between frictional torque and angular velocity Ω_o, such as depicted in Figure 1.2.1b. Such a response is akin to the negative damping observed in drilling jobs. Indeed torque measurements while drilling suggest that the resisting torque at the bit decreases with increasing Ω_o. More specifically [15] presents some results where reduced torque is associated with increasing angular velocity under constant WOB (Figure 1.2.1a), and points out that it is an inherent PDC bit characteristic. The conclusion from this study was that stick-slip mitigation is possible by reducing torque through increasing Ω_o or decreasing WOB. However, in [15] there is no explanation for the reasons behind such torque behavior.

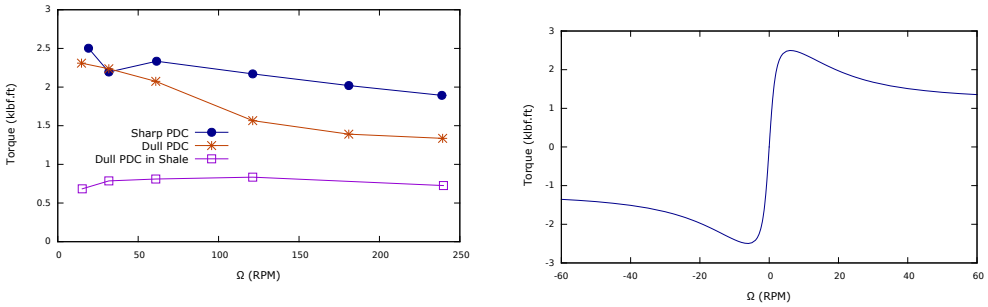

(a)

(b)

Figure 1.2.1: Torque-friction relationship: (a) Test results from [15], and (b) non linear analytical approximation from [59],

There are two concerns with the weakening torque-velocity relationship approach. First, it does not account for the coupling between axial and angular dynamics, even though its importance is recognized [62]. Second, experiments with kinematic control with single PDC cutter and tricone bits [27] do not support the weakening torque-velocity relationship. In the

latter, the resulting torque is almost constant with increasing Ω_o as shown in Figure 1.2.2.

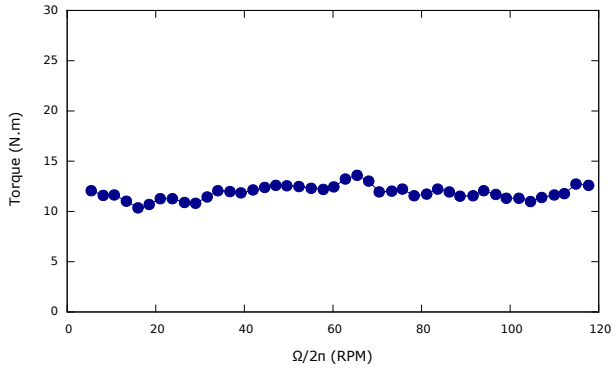

Figure 1.2.2: Torque variation with angular velocity for drilling test with a tricone bit and kinematic control from [27].

1.2.2 Self-excited vibrations

Another approach to model axial and torsional vibrations is to introduce the regenerative effect into the bit/rock interface law. The regenerative effect has widely been used in models involving metal cutting to study self-vibrations of machining tools [58, 4, 5, 56]. The insertion of the regenerative effect to describe the cutting forces results in delay differential equations (DDE) [55, 10, 26].

To our knowledge, only a few authors have considered the regenerative effect for self-excited drilling dynamics. For example [17] studied the uncoupled torsional motion of drilling system using DDE, but not the axial motion. Interestingly, in [39] the coupled axial and torsional bit dynamics is numerically evaluated by taking into account the actual forces acting on each PDC cutter. The coupling between axial and torsional motion was made through the bit/rock relationship. However, there is no mention about the use of DDE's as a modeling framework.

In [48], the author explored a more comprehensive approach to study the stick-slip problem, including the regenerative effect, and coupling axial and torsional motions. The lumped model,

denoted here as the RGD model [52], is characterized by a set of delay differential equations [10] for axial and torsional motion coupled by the bit/rock relationship. Moreover, the authors could show that the weakening torque-velocity relationship is a consequence of the system behavior, rather than an intrinsic property of the drilling system as pointed by [15]. After [48], others authors developed further studies, as for instance [49, 50, 32, 29, 52, 30, 19, 31, 18], and their works are used as a basis in this thesis. The previous studies were done for the torsional oscillator with 2-DOF. In [30] a finite element model was used to understand stick-slip conditions in time domain simulations.

1.3 Objectives

This thesis addresses the study of the stick-slip phenomena using a phenomenological model based on the regenerative effect. This phenomenological model, imposed as boundary condition at the bit, couples the axial and torsional motion of the drill string through the variable depth-of-cut d. A simple angular velocity control system at the surface is compared to a standard drive system as a stick-slip mitigation solution, even though the control set up is made upon torque-velocity weakening assumptions.

The role of spatial discretization appeared to be of crucial importance. This issue is addressed by means of simple models with axial oscillators. Afterwords, the discretization study is extended to the coupled axial and torsional oscillators, where a hypothetical case of semi-infinite drill string is also studied. The stability study of these discrete system, and their time domain behavior, are the key to understand stick-slip oscillations, and mitigation possibilities.

1.4 Thesis Structure

This thesis is organized from the continuous system representation to the semi-discretization problem.

Chapter 2 presents first a simplified description of a drilling system with relevant information for the current study. Then the imposed drilling parameters at the surface, and some possible alternatives to actual rigs are briefly introduced. A phenomenological bit/rock interaction law

[22] is then presented. This law, in conjunction with a dynamic model of the drilling system, leads to the formulation of a model described by delay differential equations. The drill string is modeled as a continuous wave-propagating medium, on which the imposed boundary conditions are the drilling parameters at the surface, and the bit/rock interaction law at the bit. The steady-state problem solution is provided, and dimensionless formulation for the perturbed dynamics is presented.

The governing equations presented in Chapter 2 are then semi-discretized in Chapter 3, based on a finite element formulation. The semi-discrete governing equations, representing the perturbed axial and torsional displacements, are used to understand the evolution of the drilling dynamics over time, and the conditions leading to stick-slip vibrations. The stability the semi-discrete form is not assessed, for reasons discussed in the beginning of Chapter 3 and further explored in Chapter 6.

Chapters 4 and 5 discuss the importance of the spatial discretization used to describe the dynamics of the drilling system. We start with a simplified model to understand how the discretization changes the axial drilling dynamics, based on a time scale separation approach presented in [52]. Lumped models with 2 and 3 oscillators have their stability assessed. The time behavior based on its stability charts are presented. Time simulation for a 10 axial oscillators model is presented.

Chapter 6 discusses the main results and limitations of the current study, as well as suggestions for future work.

Chapter 2

Drill String Dynamics Model

This chapter is structured in two main sections. The first section describes a simplified drilling system that represents the main features relevant for this study. The second section presents a general formulation of the drilling system dynamics, with the imposed surface boundary conditions and the bit/rock interface relationship that establishes the boundary conditions at the bit. Finally, a dimensionless model formulation is presented and the stationary and perturbed motions are introduced.

2.1 Drilling System Description

The system described here consists of the main components necessary to drill a well: the surface drive system, the drill string, and the drill-bit. The drive system (rotary table or top drive) imposes the hook load H and the angular velocity Ω at the surface. The drill string, composed mainly of drill pipes and drill collars, transmits the vertical force and torque imposed at the surface to the bit, which drills the rock. The closed-loop circulation drilling fluid removes the cuttings, whose effects are not considered in the present study. Figure 2.1.1a shows a PDC bit with a view of a PDC cutter, and Figure 2.1.1b illustrates an idealized drill bit of the type considered in this study.

The coordinate system x is aligned with the borehole, pointing downward. Its origin is at

the surface. The boundary conditions imposed at the surface, *i.e.,* at $x = 0$, are the vertical force (or hook load) H and angular speed Ω.

A bit/rock interface law describes the lower boundary condition (at the bit, *i.e.,* at $x = L$). This interface law describes the relationship between the amount of rock removed by the bit and the applied weight (axial force) and torque on bit (W and T, respectively). The drill-bit is considered to be rigid and its dimensions can be disregarded in comparison with the total length of the drill-string (the total length L is the sum of the drill-pipes and BHA lengths, respectively denoted by L_d and L_b).

The system dynamics is described in terms of the axial and angular displacements (denoted by $U(x,t)$ and $\Phi(x,t)$, respectively), which are measured from a fixed reference at the surface. The drill string effective weight provides the applied weight on bit W. The applied vertical force H is chosen based on the desired weight on bit W ($W = \int_0^L A(x) f_u dx - H$, with f_u being the effective weight per unit volume and $A(x)$ the cross sectional area of the drill string) to drill the well. The axial force $F(x,t)$ and torque $T(x,t)$ fields are the sum of the quasi-static force and torque (F_s and T_s) and those arising from the dynamical motion (F_d and T_d).

It is important to recognize that, although the length of the drill string increases (by adding more pipes at the surface), the overall dynamics is established during an interval over which the drill string length is almost constant. In a practical sense, it means that we can evaluate the entire dynamics of the system for a given wellbore depth or drill string length L.

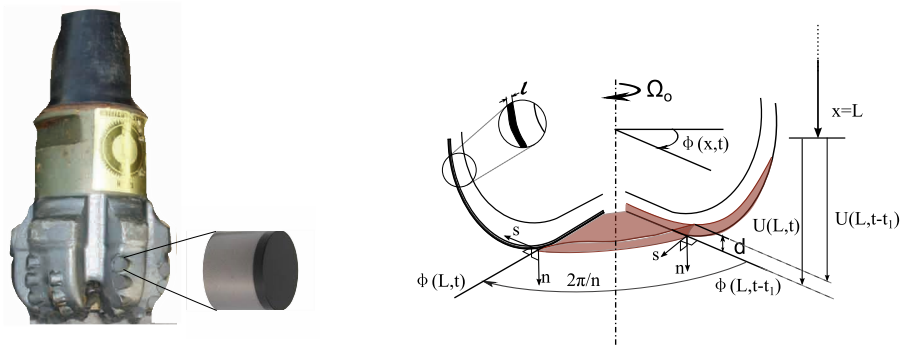

(a) (b)

Figure 2.1.1: Drill-bit: (a) PDC drill bit with PDC cutter in detail, (b) Idealized drill bit showing two blades, local frame of reference $s-n$, depth of cut $d(t)$, worn length ℓ, axial and angular displacement $U(L,t)$ and $\Phi(L,t)$ with respectively delayed displacements $U(L,t-t_1)$ and $\Phi(L,t-t_1)$ displacements.

2.2 Controllable Parameters and Interface Law

2.2.1 Controllable Parameters

Conventional drive systems attempt to keep the hook load H and drill string angular speed Ω constant at the surface. If the system exhibits vibration, both H and Ω oscillate due to the complex nature of the BC at the rig. However, the BC are often simplified to a constant hook load $H(0,t) = H_o$ and constant angular velocity $\Omega(0,t) = \Omega_o$, as in [48], for example.

An alternative approach is to consider the presence of the so-called "Soft-Torque" (ST) [3, 37] controller in the drive system. ST was designed to be installed in drive systems to mitigate stick-slip oscillations. The ST system is an angular velocity controller that is represented within this thesis by a torsional spring and dash-pot at the top boundary condition. The ST system attempts to damp the dominant (first) torsional mode for stick-slip. A schematic view of a drive system with ST is shown in Figure 2.2.1. Herein, the drive system [2] is assumed to be a rectangular block with mass $M_{DS} = 18160$ kg, cross-sectional dimensions equal to $l_1 = 1.867$ m

and $l_2 = 1.722$ m, and moment of inertia $I_{DS} = M_{DS}/12\left(l_1^2 + l_2^2\right)$.

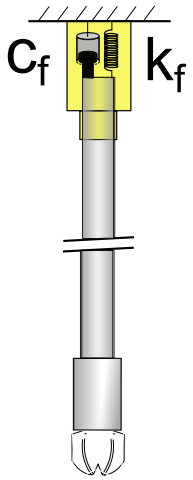

Figure 2.2.1: Soft torque scheme, after [37, 1].

2.2.2 Bit-rock Interface Law

Before we describe the bit/rock interface law, we introduce the forces acting on a single cutter under controlled conditions. Experimental observations conducted during single cutter tests form the basis for the development of the drag bit/rock interface law. The extrapolation for the cutting behavior of the drill bit is presented next.

Single cutter-rock interface behavior. During drilling, the power delivered to the drag bits is used in part to break the rock and also to overcome the friction due to the contact underneath the cutters. Detournay and Defourny [22] described the cutting process by means of a phenomenological model stating that the cutter action consists of two independent processes: (a) cutting of rock and (b) a frictional contact at the wear flat/rock interface. The cutting force $\mathbf{F^c}$ is proportional to the instantaneous depth of cut d, and the frictional contact force $\mathbf{F^f}$ is function of the contact stress σ_f underneath the cutter.

The forces applied by the cutter on the rock, $\mathbf{F^c}$ and $\mathbf{F^f}$, are described as functions of the

intrinsic specific energy (ε), depth-of-cut d, the contact stress (σ_f), and the cutter geometry (cutter width w and blunt length ℓ) [22]:

$$\mathbf{F^c} = \left\{ \begin{array}{c} \mathrm{F_n^c} \\ \mathrm{F_s^c} \end{array} \right\} = \varepsilon w d \left\{ \begin{array}{c} \zeta \\ 1 \end{array} \right\}, \tag{2.2.1}$$

$$\mathbf{F^f} = \left\{ \begin{array}{c} \mathrm{F_n^f} \\ \mathrm{F_s^f} \end{array} \right\} = \mathrm{F_n^f} \left\{ \begin{array}{c} 1 \\ \mu \end{array} \right\}. \tag{2.2.2}$$

The positive sign means that these forces act in the same direction as the cutter velocity, and the local coordinate system (at the cutter) is defined by the unit vertical axis **n** pointing downwards, and the unit horizontal axis **s** pointing in the same direction as the cutter velocity. The intrinsic specific energy ε can be understood as the amount of energy necessary to remove an unit volume of rock, while the parameter ζ characterizes the ratio between the vertical and horizontal component of force acting on the cutting face. Both ε and ζ can be measured from single cutter tests.

Now considering that frictional forces are developed under the blunt wear flat, the vertical friction force is a function of contact stress σ_f and the area of contact (ℓw). The vertical and horizontal friction forces can be related through the rate-independent coefficient of friction μ:

$$F_s^f = \mu F_n^f = \mu \sigma_f \ell w. \tag{2.2.3}$$

The contact stress assumed is to be constant if the axial velocity $V > 0$. If there is no contact, $F_s^f = 0$.

Bit-rock interface behavior. The concept developed above for a single cutter can be extended to a drag bit (see Figure 2.1.1.). The weight **W** and torque **T** on bit (now on called weight- and torque-on-bit, respectively) are comprised by cutting and friction at contact (superscripts f and c) and forces and torques are written as follows:

$$\mathbf{W} = \mathbf{W^f} + \mathbf{W^c}, \tag{2.2.4}$$

$$\mathbf{T} = \mathbf{T^f} + \mathbf{T^c}. \tag{2.2.5}$$

The cutting forces are proportional to the depth of cut d and are stated as a function of the bit radius a, intrinsic specific energy ε, and the depth of cut d, and the number of blades n_b.

The frictional forces are proportional to the stress underneath the cutters (or blades) σ_f, and the contact area. Decomposing the force and torque and assuming that the contact stress σ_f is constant throughout the cutters or blades we have the forces acting in the vertical direction:

$$W^c = n_b \zeta \varepsilon a d, \tag{2.2.6}$$

$$W^f = n_b a \ell \sigma_f. \tag{2.2.7}$$

The torque will be proportional to the developed forces acting on the bit on horizontal direction (both cutting and frictional contact).

$$T^c = \frac{1}{2} n_b \varepsilon a^2 d, \tag{2.2.8}$$

$$T^f = \frac{1}{2} n_b a^2 \mu \gamma \ell \sigma_f, \tag{2.2.9}$$

where the constant γ embodies the influence of the bit design on its mechanical response. If γ is equal to one it means that the blades are perpendicular to the axis of revolution. The contact length ℓ (Figure 2.1.1b) and the bit radius a defines the frictional contact area under the bit.

2.3 Drill String Model

Consider the drill string shown in Figure 2.3.1. The coordinate system x refers to a drill string cross section position and $U(x,t)$ represents its longitudinal displacement. The axial stress varies over the element, due to body forces or to accelerations. The quantity $q_x := q(x,t)$ represents the axial body and damping forces per unit volume. The linear momentum balance for the differential element with constant cross sectional area A, density ρ, and elastic modulus E reads:

$$\rho A \frac{\partial^2 U}{\partial t^2} - EA \frac{\partial^2 U}{\partial x^2} + q_x = 0 \tag{2.3.1}$$

Similarly, the angular momentum balance for constant moment of inertia J, and shear modulus G reads :

$$\rho J \frac{\partial^2 \Phi}{\partial t^2} - GJ \frac{\partial^2 \Phi}{\partial x^2} + q_\phi = 0, \tag{2.3.2}$$

where $\Phi(x,t)$ denotes the angular displacement.

The axial and torsional wave velocities are defined by $c_u = \sqrt{E/\rho}$ and $c_\phi = \sqrt{G/\rho}$. The term q_x in Equation (2.3.1) can be rewritten as $q_x := q\left(x, \dot{U}(x,t)\right) = f_u - \varsigma_u \dot{U}(x,t)$, with f_u being the drill string buoyed weight per unit volume and $-\varsigma_u \dot{U}(x,t)$ representing a damping force proportional to the cross sectional axial velocity. In the same way, the torsional damping can be introduced as $q_\phi := q\left(\dot{\phi}(x,t)\right) = -\varsigma_\phi \dot{\Phi}(x,t)$. The parameters ς_u and ς_ϕ are the damping proportionality factors. If $q_x = q_\phi = 0$, Equations (2.3.1) and (2.3.2) are the so-called wave equations.

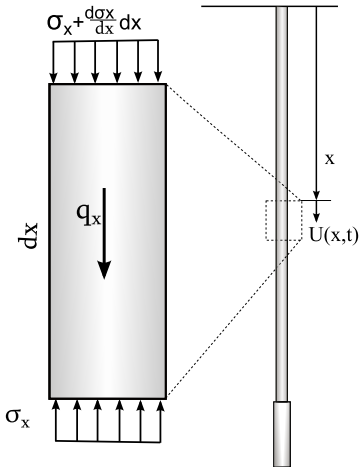

Figure 2.3.1: Drill string with coordinate system x and axial displacement $U(x,t)$ for a particular section. The stresses and forces acting on an differential element of length dx are presented on the left hand side. The force $q_x := q(x, U, t)$ can represent the body forces, damping forces, or the sum of both.

The boundary conditions at $x = 0$ are herein assumed to be a constant axial force H_o and a constant angular velocity Ω_o. The boundary conditions at the bit are the vertical or axial components of the actual weight W defined by Equations (2.2.4), (2.2.6), and (2.2.7) and the torque on bit T resisting the angular motion defined by Equations (2.2.5), (2.2.8), and (2.2.9). These boundary conditions are written as follows:

$$EA_b \left.\frac{\partial U}{\partial x}\right|_{x=L} = -W, \qquad GJ_b \left.\frac{\partial \Phi}{\partial x}\right|_{x=L} = -T \tag{2.3.3}$$

2.3.1 Stationary Solution

First we assume that the axial force H_o and angular velocity Ω_o, imposed at the surface, result in a constant (nominal) penetration rate V_o. Then the drill-string (axial and torsional) nominal displacement is the sum of its initial position and the displacement due to the constant velocity (V_o and Ω_o). The initial drill-string position in the coordinate frame presented in Figure 2.1.1 is $U(x,0)$ and $\Phi(x,0)$ for $0 \leq x \leq L$, where L is the borehole length.

Assuming constant depth-of-cut over one blade, the "height" of rock in front of each blade, indicated by d_o for nominal motion, is function of the current and past drill-bit position, and can be written as $d_o = U_o(L,t) - U_o(L,t-t_1)$, where $U_o(L,t)$ denotes the nominal axial displacement. The time lag or delay t_1 is the time taken by the bit with n_b blades to rotate an angle of $2\pi/n_b$. For constant angular velocity Ω_o, the time lag is constant and equal to $2\pi/\Omega_o n_b$. If in addition the axial velocity is constant, the bottom-hole profile projection on the cylindrical surface represented by the borehole wall is a straight line (Figure 2.3.2) between blades. Therefore, all blades face the same depth-of-cut d_o. The axial drilling speed is then evaluated from the actual equilibrium depth-of-cut d_o and angular speed Ω_o. The total axial displacement after one revolution is $n_b d_o$, and the axial steady-state motion can be written as

$$V_o = \frac{n_b d_o \Omega_o}{2\pi},$$
$$U_o(x,t) = U(x,0) + V_o t. \tag{2.3.4}$$

The drill-string angular position is derived from the initial angular position $\Phi(x,0)$ and the constant angular velocity as follows:

$$\Phi_o(x,t) = \Phi(x,0) + \Omega_o t. \tag{2.3.5}$$

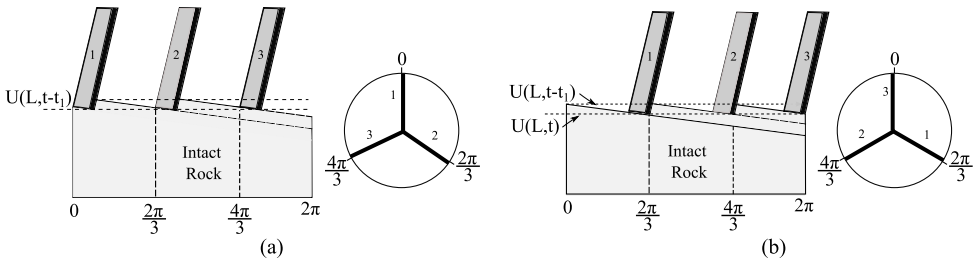

Figure 2.3.2: Well bore schematic linear representation and top view during steady-state drilling showing that all blades (three in this example) face the same depth-of-cut d_o: (a) The position of blade 1 is $\Phi = 0$ at time $t - t_1$ and, (b) the position of blade 1 is $\Phi = {}^{2\pi}/_{3}$ at time t.

To derive the actual steady-state depth-of-cut d_o we have to determine first the applied equilibrium weight on bit from $W_o = \int_0^L f_u dx - H_o$. Once the nominal applied weight on bit is known, the equilibrium depth of cut thus can be derived from the bit/rock interaction law presented earlier. The equilibrium weight on bit W_o corresponds to the sum of forces acting on the cutters in the vertical direction. The vertical component of cutting and friction forces (W^c and W^f, respectively) balances the applied weight on bit W_o. From vertical force balance and Equations (2.2.4) and (2.2.6) we can write the equilibrium depth-of-cut d_o as:

$$d_o = \frac{W^c}{n_b \zeta a \epsilon} = \frac{W_o - W^f}{n_b \zeta a \epsilon} = \frac{2\pi V_o}{n_b \Omega_o}, \tag{2.3.6}$$

which is valid only if $W_o > W^f$, otherwise there is no drilling (all force is then consumed by the frictional contact).

2.4 Dimensionless Model Formulation

We present in this section the dimensionless parameters first introduced by [22] (later extended by [48]), while developing the trivial motion response. Then, the perturbed dimensionless variables used in [49, 51, 29, 19] are presented and the equations governing the non-trivial response are formulated. These equations form the basis of the models developed within this dissertation, *i.e.* the response presented in this section is inherent to the drilling system and not to a particular model.

2.4.1 Dimensionless Parameters

To define the dimensionless parameters characterizing the dynamics (see for example [48, 32, 29, 30]) we first introduce the following characteristic quantities: time t_*, depth-of-cut d_*, weight on bit W_*, and torque on bit T_*. These quantities are described in terms of the rock and drill-bit properties through the bit/rock interaction law, drill pipe polar moment of inertia J_p defining global torsional drill pipe stiffness $C = {}^{GJ_p}/_{L}$ and BHA inertia I as follows:

$$t_* = \sqrt{\frac{I}{C}},\ d_* = \frac{2C}{\varepsilon a^2},\ W_* = \zeta \varepsilon a d_*,\ T_* = \frac{1}{2} a W_*. \tag{2.4.1}$$

The dimensionless axial coordinate system ξ is defined as:

$$\xi = \frac{x}{L}. \tag{2.4.2}$$

The dimensionless instantaneous and equilibrium depth-of-cut (δ and δ_o), torque and weight on bit ($\mathcal{T}$ and $\mathcal{W}$) are defined using the related characteristics quantities defined above:

$$\delta = \frac{d}{d_*},\ \delta_o = \frac{d_o}{d_*} = \frac{V_o t_1}{d_*},\ \mathcal{T} = \frac{T}{T_*},\ \mathcal{W} = \frac{\mathrm{W}}{\mathrm{W}_*}. \tag{2.4.3}$$

The numbers defining bluntness [48] and bit/rock interaction [22], λ and β are respectively given by:

$$\lambda = \frac{\ell a^2 \sigma_f}{2\zeta C},\ \beta = \mu\gamma\zeta. \tag{2.4.4}$$

2.4.2 Stationary Solution

The stationary or nominal response corresponds to constant axial and angular velocity, with the motion defined by Equations (2.3.4) and (2.3.5). In order to express the steady-state motion in terms of dimensionless variables, we define dimensionless time τ, and the dimensionless nominal torsional and axial velocity, ω_o and v_o, respectively. Let δ_o be the dimensionless nominal depth-of-cut, and the dimensionless equilibrium weight-on-bit $\mathcal{W}_o$ and torque-on-bit $\mathcal{T}_o$ are defined by inserting W_o and T_o into Equation (2.4.3). Using the parameters defined earlier we obtain by Equation (2.4.1):

$$\tau = \frac{t}{t_*},\ \omega_o = \Omega_o t_*,\ v_o = \frac{V_o t_*}{d_*} = \frac{\omega_o}{2\pi}\left(\mathcal{W}_o - n_b\lambda\right),\ \tau_{1,0} = \frac{2\pi}{\omega_o n_b}. \tag{2.4.5}$$

$$\mathcal{W}_o = n_b\left(\delta_o + \lambda\right), \quad \mathcal{T}_o = n_b\left(\delta_o + \lambda\beta\right). \tag{2.4.6}$$

The constant dimensionless time delay $\tau_{1,0}$ represents the dimensionless time necessary for the bit to rotate the angle spanned by two consecutive blades and equal to $2\pi/n_b$ during steady state motion. In the dimensionless coordinate frame of reference defined by Equation (2.4.2), the drill-bit is always at $\xi = 1$ and moving with constant velocity υ_o defined by Equation (2.4.5).

2.4.3 Perturbed Solution

Now, we consider the fact that the system can undergo a motion that is not stationary. In this case, perturbations can occur around the nominal motion. We define the dimensionless perturbed axial and angular displacements as follows [52, 30, 21]:

$$u = \frac{U - U_o}{d_*},\ \varphi = \Phi - \Phi_o. \tag{2.4.7}$$

The variables U_o and Φ_o which are described by Equations (2.3.4) and (2.3.5), and represent the nominal axial and angular displacements. The variables U and Φ represent the total motion, therefore Equation (2.4.7) describes the perturbed motion. Using the defined dimensionless variables, Equations (2.3.1) and (2.3.2), the equations governing the linear and angular perturbation waves propagation read:

$$\frac{\partial^2 u}{\partial \xi^2} + \mathcal{Q}_u = \mathcal{G}_u \frac{\partial^2 u}{\partial \tau^2} \tag{2.4.8}$$

$$\frac{\partial^2 \varphi}{\partial \xi^2} + \mathcal{Q}_\varphi = \mathcal{G}_\varphi \frac{\partial^2 \varphi}{\partial \tau^2}. \tag{2.4.9}$$

The parameters $\mathcal{G}_u$ and $\mathcal{G}_\varphi$ are defined as $\mathcal{G}_u = \frac{1}{c_u^2}\left(\frac{L}{t_*}\right)^2, \mathcal{G}_\varphi = \frac{1}{c_\varphi^2}\left(\frac{L}{t_*}\right)^2$ [30]. The functions $\mathcal{Q}_u$ and $\mathcal{Q}_\varphi$ are the perturbed damping forces. They are usually difficult to establish in practice. Equations for $\mathcal{Q}_u$ and $\mathcal{Q}_\varphi$ are presented in Chapter 3, assuming they are proportional to inertial and elastic forces (i.e. Rayleigh damping).

We introduce the variables $\upsilon(\xi, \tau)$ and $\omega(\xi, \tau)$ as the perturbed axial and angular velocities. These are related to the perturbed displacements by the following relationships:

$$\upsilon(\xi, \tau) = \frac{\partial}{\partial \tau} u(\xi, \tau),\ \omega(\xi, \tau) = \frac{\partial}{\partial \tau} \varphi(\xi, \tau).$$

Although the axial velocity is not constant and the bottom hole profile is irregular, all blades are still facing the same depth-of-cut. Figure 2.4.1 below shows that each blade removes the

same amount of rock, as they are uniformly positioned. As stated before, the depth-of-cut is the difference between the current and delayed bit axial positions, namely $U(t)$ and $U(t-t_1)$ respectively. The dimensionless depth-of-cut is written as $\delta = \delta_o + \hat{\delta}$, where the perturbation is $\hat{\delta} = u(1,\tau) - u(1,\tau-\tau_1) + \upsilon_o\hat{\tau}_1$. An expression for the perturbed time delay $\hat{\tau}_1$ is presented later.

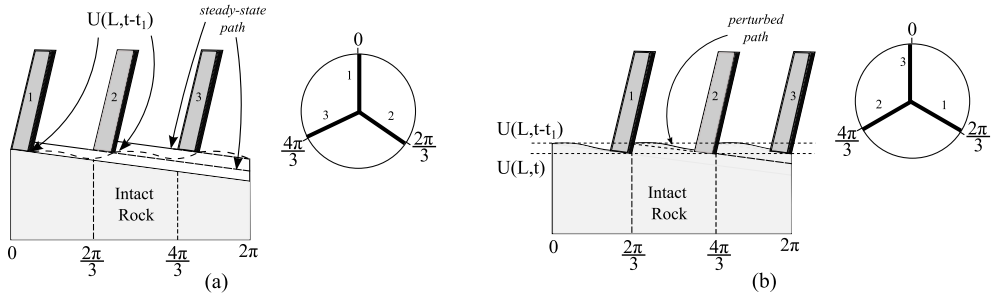

Figure 2.4.1: Well bore schematic linear representation and top view during drilling with vibration, showing that all blades (three in this example) face the same depth-of-cut d_o: (a) Blade 1 position is $\Phi = 0$ at time $t - t_1$ and, (b) blade 1 position is $\Phi = {}^{2\pi}/_{3}$ at time t.

With the perturbed axial and angular displacements, both weight-on-bit and torque-on-bit on bit vary. These variations, described here as $\hat{\mathcal{W}}$ and $\hat{\mathcal{T}}$, are the sum of the cutting and friction at contact force components variations. The perturbed dimensionless weight and torque on bit can be described as:

$$\hat{\mathcal{W}} = \hat{\mathcal{W}}_c + \hat{\mathcal{W}}_f = n_b\left[u(1,\tau) - u(1,\tau-\tau_1) + \upsilon_o\hat{\tau}_1\right] - n_b\lambda g(\upsilon) \tag{2.4.10}$$

$$\hat{\mathcal{T}} = \hat{\mathcal{T}}_c + \hat{\mathcal{T}}_f = n_b\left[u(1,\tau) - u(1,\tau-\tau_1) + \upsilon_o\hat{\tau}_1\right] - n_b\lambda\beta g(\upsilon) \tag{2.4.11}$$

The set-valued function $g(\upsilon)$ defines the friction at contact force acting underneath the cutters. If $\upsilon > -\upsilon_o$, $g(\upsilon) = 0$, and $g(\upsilon) = 1$ for $\upsilon < -\upsilon_o$. For the case where $\upsilon = -\upsilon_o$, $g(\upsilon) \in [0,1]$ and is evaluated from the force equilibrium $\mathcal{W}_o = n_b(\delta + \lambda g(\upsilon))$ in the axial direction.

The bottom BC are described in terms of the dimensionless perturbation of weight-on-bit $\hat{\mathcal{W}}$ and torque-on-bit $\hat{\mathcal{T}}$ as follows:

$$\left.\frac{\partial u}{\partial \xi}\right|_{\xi=1} = -\psi_u \hat{\mathcal{W}}, \ \left.\frac{\partial \varphi}{\partial \xi}\right|_{\xi=1} = -\psi_\varphi \hat{\mathcal{T}}, \tag{2.4.12}$$

with $\psi_u = \zeta \varepsilon a L/EA_b$, $\psi_\varphi = CL/GJ_b$.

The surface boundaries conditions are assumed to be a constant hook load H_o and a constant angular velocity, Ω_o, which corresponds to $\partial u/\partial \xi = 0$ and $\varphi = 0$, respectively. Another possibility within this thesis is to assume a constant axial velocity, i.e., impose $\nu_o = \partial u/\partial \tau = 0$ instead of $\partial u/\partial \xi = 0$.

To complete our description, we need to define the time delay. Once the angular speed is not constant, the time delay becomes dependent of the state. The state-dependent delay can be obtained from an implicit algebraic equation, and is equal to the elapsed time for the bit to rotate a fixed angle $^{2\pi}/_{n_b}$. Figure 2.4.2 depicts the total angular bit position Φ as function of the (dimensionless) time τ. The dashed line represents the steady-state response ($\Phi_o = \Omega_o t = \omega_o \tau$). The continuous line represents the response other than the trivial motion. The current dimensionless time delay τ_1 can be larger or smaller than the constant time delay $\tau_{1,0}$ from the stationary solution. The implicit algebraic equation defining the current time delay $\tau_1 := \tau_1(\phi)$ is (see [48, 52]):

$$\varphi(1,\tau) - \varphi(1,\tau-\tau_1) + \omega_o \tau_1(1,\tau) = \frac{2\pi}{n_b}, \tag{2.4.13}$$

or in terms of perturbed time delay $\hat{\tau}_1(1,\tau) = \tau_1(1,\tau) - \frac{2\pi}{\omega_o n_b}$, and reminding that $\tau_{1,0} = \frac{2\pi}{\omega_o n_b}$ is the time delay in the equilibrium conditions (see Equation (2.4.5)):

$$\varphi(1,\tau) - \varphi(1,\tau-\tau_1) + \omega_o \hat{\tau}_1(1,\tau) = 0. \tag{2.4.14}$$

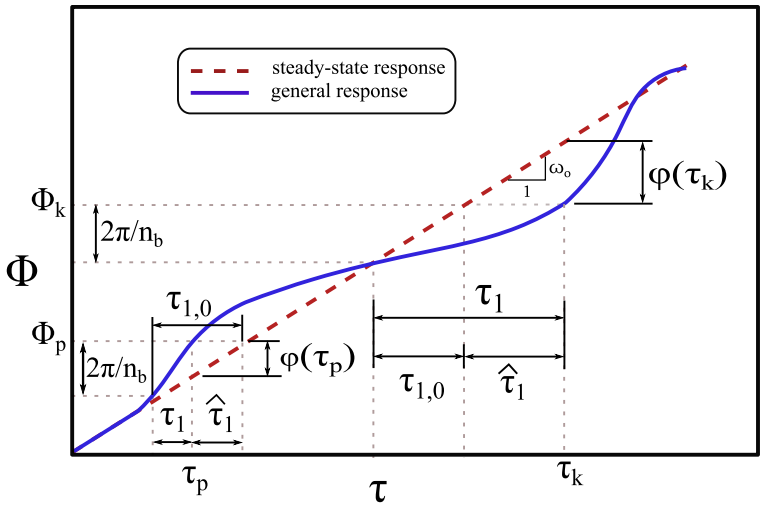

Figure 2.4.2: Schematic graph showing how the current (dimensionless) time delay τ_1 relates to the constant time delay $\tau_{1,0}$ from the stationary motion and its perturbation $\hat{\tau}$, based on the total angular position $\Phi(\tau)$. The perturbed angular displacement for two particular times are shown. In such cases $\varphi_p := \varphi(\tau_p) > 0$ and $\varphi_k := \varphi(\tau_k) < 0$.

2.5 Summary

In this chapter we presented a general formulation for the nominal solution, where axial and torsional motion are linearly proportional to the velocities, based on the regenerative effect as bit/rock BC. Then the formulation based on the dimensionless axial and torsional displacements perturbations was presented, in which it was possible to write down the governing equations of the propagating perturbation in the drill string. To complete the problem formulation, the dimensionless BC at the top (constant hook load and torsional velocity, or constant axial and torsional velocities), and at the bottom (weight and torque-on-bit perturbations) were presented. The latter is described by delay differential equations, with state dependent delay. In order to solve the problem, a spatial discretization is proposed in the next chapter, based on the finite element formulation. As will be seen, the stability of the problem is dependent on the spatial discretization choice, which is addressed later in this thesis.

Chapter 3

Finite Element Model Formulation

3.1 Introduction

This chapter presents the semi-discrete form of Equations (2.4.8) and (2.4.9), developed based on a finite element formulation [47, 44]. Stability of the semi-discrete system of equations describing the drill string dynamics is not analyzed here. There are still unresolved issues in regard to the role of the discretization on the stability of the system of equations, as first shown by Liu *et* al [40]. These authors studied the stability of a discrete system composed of axial and torsional oscillators (consisting of a mass and a spring) with dash pots representing the drilling system with the same bit rock interface law presented here, as depicted in Figure 3.1.1.

The stability study, which was based on the semi-discretization method [34], indicates that the stable area in the parameter space $\omega_o - v_o$ reduces when increasing the number of degrees of freedom. The stability result is shown in Figure 3.1.2, with n_d and n_b being the number of axial and torsional oscillators representing the DP and BHA, respectively. For instance, a discrete system with 5 oscillators has a much smaller stability region compared to a system with only 1 oscillator. For 24 oscillators, there is only a narrow area characterizing stable operating conditions in terms of ν_o and ω_o.

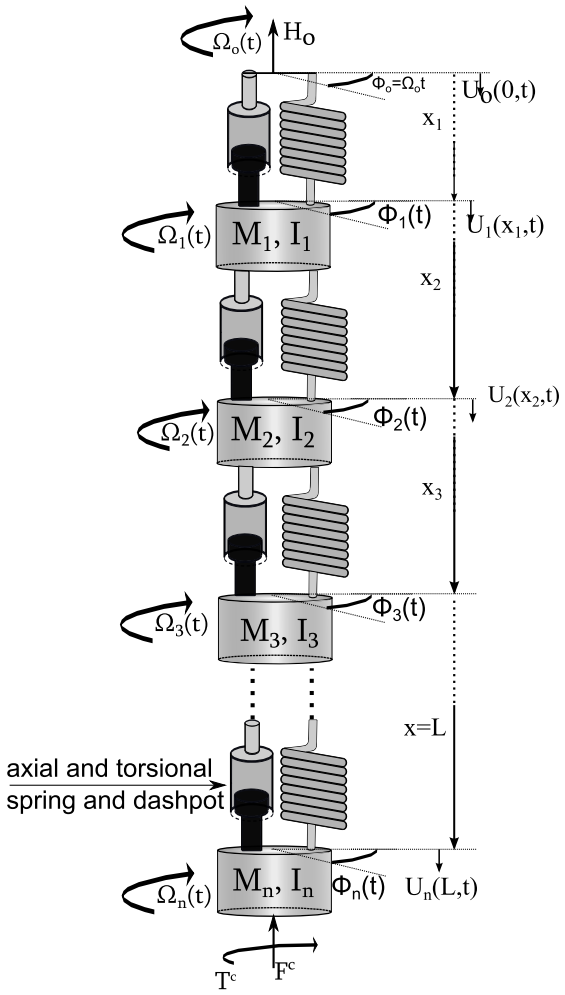

Figure 3.1.1: Discrete system representation of drilling system with masses-springs-dash pots for axial and torsional motions (adapted from [40]).

In Chapters 4 and 5, we study in more detail the effects of the spatial discretization on the stability of the resulting DDE system of equations. In this current chapter, we only investigate the occurrence of stick-slip based on time simulations. The benchmark drilling system is the one already studied in [30]. In doing so, we also study the dynamics of an equivalent system with ST, which exhibited unstable motion but with slower growth of angular oscillations when compared to a conventional drive system.

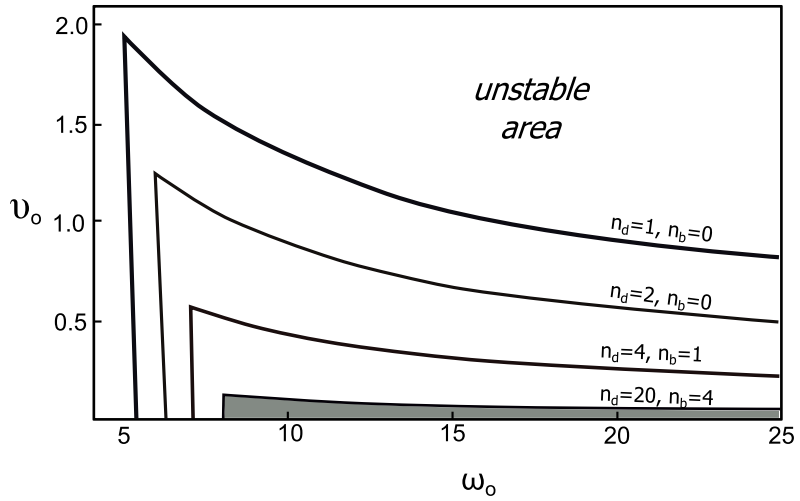

Figure 3.1.2: Stable region (high-lighted by shaded area for $n_d = 20$ and $n_b = 4$) in the dimensionless parameter space $\omega_o - \upsilon_o$ with different number of degrees of freedom, where n_d and n_b are the number of oscillators representing the DP and BHA, respectively (adapted from [40]).

3.2 Semi-discrete Model Formulation

To solve Equations (2.4.8) and (2.4.9) subject to the boundary conditions at the surface ($\xi = 0$) and at the bit ($\xi = 1$), the governing equations are discretized into $n - 1$ elements, where n is the number of nodes. The node labeled as 1 is located at the surface and the one labeled as n is located at the bit. For more details about the semi-discrete formulation, refer to Appendix A.1, and also [47, 44, 30]. We can rewrite Equations (2.4.8) and (2.4.9) in semi-discrete form as follows:

$$\mathcal{G}_u \mathbf{M}\ddot{\mathbf{u}} + \chi_u \mathbf{D}\dot{\mathbf{u}} + \mathbf{K}\mathbf{u} = \mathbf{F} \tag{3.2.1}$$

$$\mathcal{G}_\varphi \mathbf{J}\ddot{\mathbf{\Phi}} + \chi_\varphi \mathbf{E}\dot{\mathbf{\Phi}} + \mathbf{C}\mathbf{\Phi} = \mathbf{T}, \tag{3.2.2}$$

where the matrices and forcing vectors for one element with linear interpolating weighty functions are given in Appendix A.1, and the assembled matrices $\mathbf{M}$, $\mathbf{J}$, $\mathbf{K}$, and $\mathbf{C}$ are given by Equations (A.1.17)-(A.1.20).

Due to the difficulty in defining the damping factors χ_u and χ_ϕ, axial and torsional damping matrices $\mathbf{D}$ and $\mathbf{E}$ are assumed to be of Rayleigh damping type, *i.e.* a linear combination of the mass $\mathbf{M}$ ($\mathbf{J}$) and stiffness $\mathbf{K}(\mathbf{C})$ matrices by the following relationships: $\chi_u\mathbf{D} = \eta_u\mathbf{M} + \vartheta_u\mathbf{K}$ and $\chi_\varphi\mathbf{E} = \eta_\phi\mathbf{J} + \vartheta_\phi\mathbf{K}$. The force $\mathbf{F}$ and torque $\mathbf{T}$ vectors are nonzero at the bit and at the surface only (the latter depending on the imposed boundary conditions). The reaction force F_1 and torque T_1 at the surface are evaluated for the imposed surface displacement as boundary conditions. Alternatively, displacements u_1 and ϕ_1 at the surface are evaluated for imposed force and torque boundary conditions at the surface. The applied forces at the bit were derived in Chapter 2. Equation (2.3.3) defines the bottom BC in terms of total displacements, while Equation (2.4.12) defines it in terms of dimensionless displacement perturbations.

For both the standard (without any angular velocity controller) and the ST drive system, the assumed imposed BC is a constant hook load H_o and angular velocity Ω_o. But for ST, it is assumed that internal torque from the drive system (from the equivalent spring-dash pot system) acts like external torques applied in node 2 (node 1 has prescribed constant torque), and the drive system mass and inertia (defined in section 2.2.1) are concentrated at node 2.

The external torque acting at node 2, which corresponds to the torque applied by the drive system is then described by:

$$GJ_d \left.\frac{\partial \Phi_2}{\partial x}\right|_{x=x_1} = k_f\Phi_2 + c_f\dot{\Phi}_2, \tag{3.2.3}$$

which gives the following dimensionless torque perturbation:

$$\left.\frac{\partial \varphi_2}{\partial \xi}\right|_{\xi=\xi_1} = \frac{L}{GJ_d}\left(k_f\varphi_2 + \frac{c_f\dot{\varphi}_2}{t_*}\right). \tag{3.2.4}$$

Following the proposal in [37], the ST gives optimum performance when its first natural torsional frequency is equal to the drill-string first natural torsional frequency, given that the drive system damper c_f is small. Defining the drive system spring stiffness as $k_f = I_{DS}/t_*^2$, the proposed optimum damping ratio in [37] is $\xi_{opt} \approx \sqrt{\Gamma/2} = 0.06$, with $\Gamma = I/I_{DS}$. That allows us to define the damping parameter as $c_f = I_{DS}/2\xi_{opt}$. This design of the ST system in fact aims do damp the first torsional resonance mode of the drill-string dynamics.

3.3 Time Simulation Results

Time simulations for the benchmark case described by Germay *et al* [30] were performed to compare the differences between a drive system without and with ST. The system has a $1,000$ m long DP, and 200 m long BHA and both cross sectional geometries are described in Appendix D.1. The spatial discretization has 58 elements (10 representing the BHA), and a forward finite difference scheme was used for the time integration. The Newmark time integration method [6] with the parameters proposed by [8] was also implemented to solve the problem. For the used small time step size $\left(\Delta\tau = 10^{-4}\right)$, there was no difference between the results obtained with these two time integration methods, and we opted for the simple forward Euler method. Other relevant drilling system properties can be found in Appendix D.1. The axial and torsional damping factors ϑ_u and ϑ_ϕ were assumed equal to 5.10^{-4} and 1.10^{-4}, respectively. Both η_u and η_φ were assumed to be zero. The drill bit has 6 blades, with $n_b\lambda = 5.0$, and applied weight on bit $WOB = 15kN$. The imposed nominal velocities are $\nu_o = 0.47$ and $\omega_o = 3.74$, and initial perturbations $\{u, \upsilon, \varphi, \omega\}^T = \{0.01, 0.01, 0.1, 0.1\}^T$ were instantaneously imposed to the system at $\tau = 0$.

The drill bit can present both axial and torsional stick. If axial stick occurs, the axial contact force is obtained from the force balance by $\hat{\mathcal{W}}_f = \mathcal{W} - \mathcal{W}_c$, $\hat{\mathcal{W}}_f \leq n_b\lambda$. During axial sticking the bit can still be rotating.

It is assumed that there is no drilling with angular stick, and axial velocity is also set to zero in such case. Backward rotation is not allowed, and when the bit presented a (small) negative angular velocity, it is set to zero. The bit slips when the applied torque on bit overcomes the reacting bit-rock interface law torque. The torque on bit is evaluated from the system of equations describing the angular motion.

The time delay τ_1 is state-dependent. To solve for the current time delay, it is necessary to solve the implicit Equation (2.4.14). For the numerical implementation, we search for the angular bit position equal to the current angular position minus $2\pi/n_b$. When looking for the delayed state $u\left(\tau_p - \tau_1\right)$ and $\varphi\left(\tau_p - \tau_1\right)$, with τ_p being the time at current time step p, we looked first for the position q in the vector of total angular displacement $\mathbf{\Phi}$ such that $\Phi_q \leq \Phi_p - 2\pi/n_b$, since the blades are assumed to be evenly distributed. For the adopted small time step size, linear

interpolation was used to find out $\tau_p - \tau_1$, $u(\tau_p - \tau_1)$ and $\varphi(\tau_p - \tau_1)$ when $\Phi_q \neq \Phi_p - 2\pi/n_b$. A schematic view of the search procedure is shown in Figure 3.3.1. To check the method, the implicit Equation (2.4.14) must be satisfied, which means that the residual of its left hand size must be close to zero.

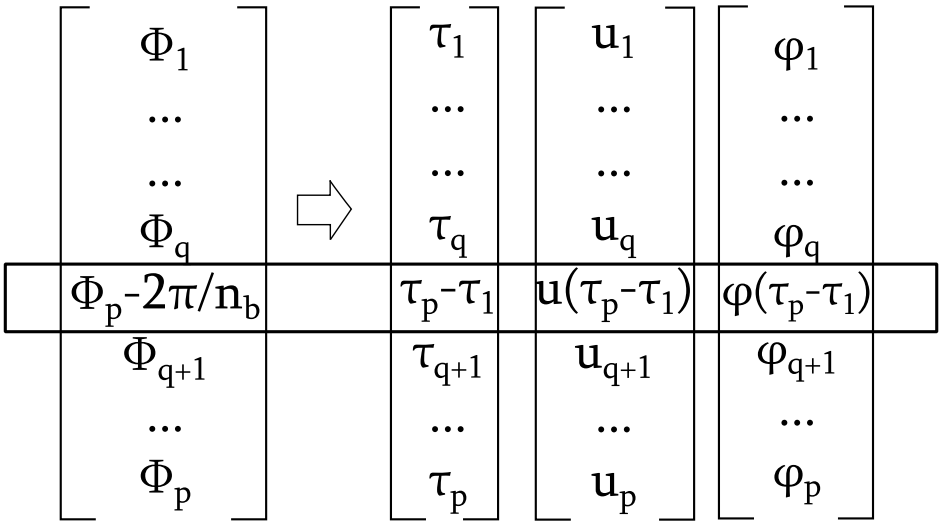

Figure 3.3.1: Time and state delay search based on total angular displacement vector $\mathbf{\Phi}$. First the position q of $\Phi_q \leq \Phi_p - 2\pi/n_b$ is determined, relating the position of the delayed states and making possible to define time delay. The values to be evaluated are shown inside the box. This method avoid the need to solve implicit Equation (2.4.14) by numerical methods.

In both cases (without and with ST system), the drill system dynamics showed the three phases described in [30]: (i) fast axial growth, with axial stick, (ii) increasing angular oscillations, and (iii) occurrence of stick-slip, as depicted in Figures 3.3.2 and 3.3.3. For the standard drive system case, it is possible to notice that first the axial velocity goes to zero, while the angular velocity oscillates within limited amplitudes, despite the larger applied initial angular perturbations. After some time, the angular velocity vanishes meaning that the bit enter a stick phase in both axial and angular motion. As the angular velocity is still applied at $\xi = 0$, the torque on bit increases with time, on average linearly, to eventually overcome the reaction

torque, causing the system to exit the stick phase. Then, the bit accelerates in the slip phase.

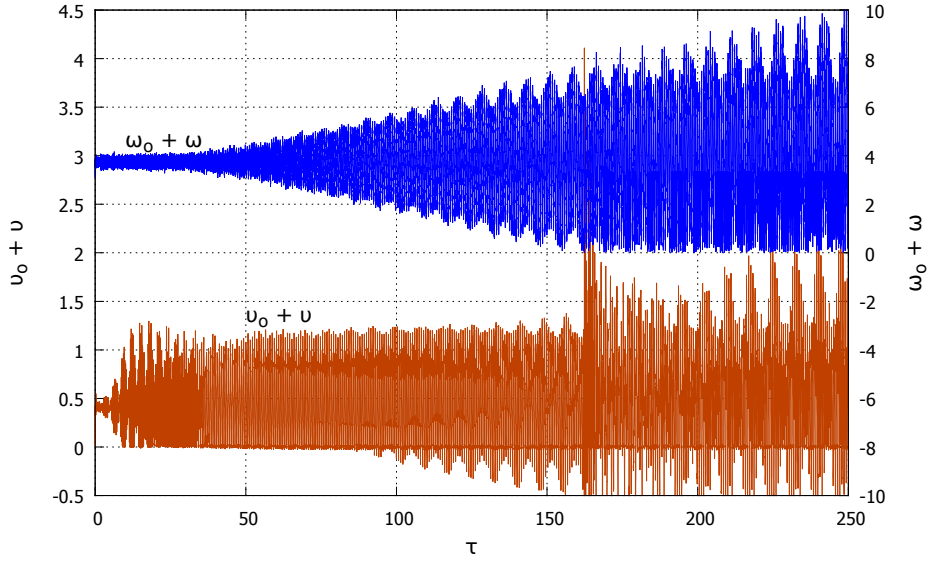

Figure 3.3.2: Evolution of bit velocities. The dynamics evolves in three phases: (i) axial stick, (ii) increasing angular oscillations, and (iii) angular stick-slip. Left vertical axis shows axial velocity, and right one shows angular velocity.

With soft torque, even using the optimum factor proposed by [37], the system still presents increasing oscillations. It was expected that the ST could minimize, or even mitigate torsional stick-slip. As evidenced by the simulations results in Figure 3.3.3, fast axial growth still happens. What is interesting is that there is less upward bit movement compared to the standard drive system (see 3.3.2). Also the axial amplitude oscillations are smaller. Angular oscillations show a slower growth rate compared to the previous case. We recall that soft torque only targets (the damping) of the first torsional flexibility mode and the fact that it has been claimed before (see for example [60]) that torsional flexibility modes at higher frequencies can still trigger stick-slip oscillations even in the presence of the ST system. Note that, in contrast to the above publications, which focus on torsional dynamics only and employ a phenomenological velocity-weakening torque as bit/rock interface law, the results above were obtained for axial-torsional

drill string dynamics coupled by the bit/rock interface law introduced in Chapter 2.

The analysis presented above confirms the importance of higher flexibility modes for the modeling and analysis of stick-slip oscillations also in the scope of the type of model presented in Chapter 2. This observation calls for further research into models for (axial and torsional) drill-string dynamics including multiple flexibility modes and raises the question on what model complexity is needed to reliably describe such dynamics. The latter is the subject of the investigation reported in Chapters 4 and 5.

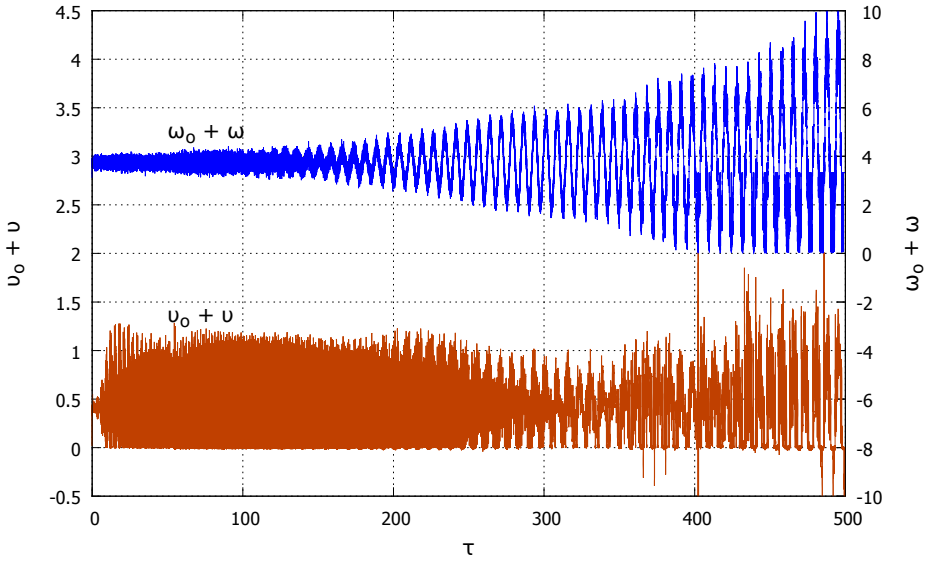

Figure 3.3.3: Bit velocities evolution with ST. The three phases are also presented here. Left vertical axis shows axial velocity, and right one shows angular velocity.

Figure 3.3.4 shows the low residual obtained by substituting the delayed state and time delay perturbation in the implicit Equation (2.4.14). Both cases are presented, but for $\tau \leq 250$ is only possible to notice the standard drive system case. The overall low residual indicates that the method provides accurate results.

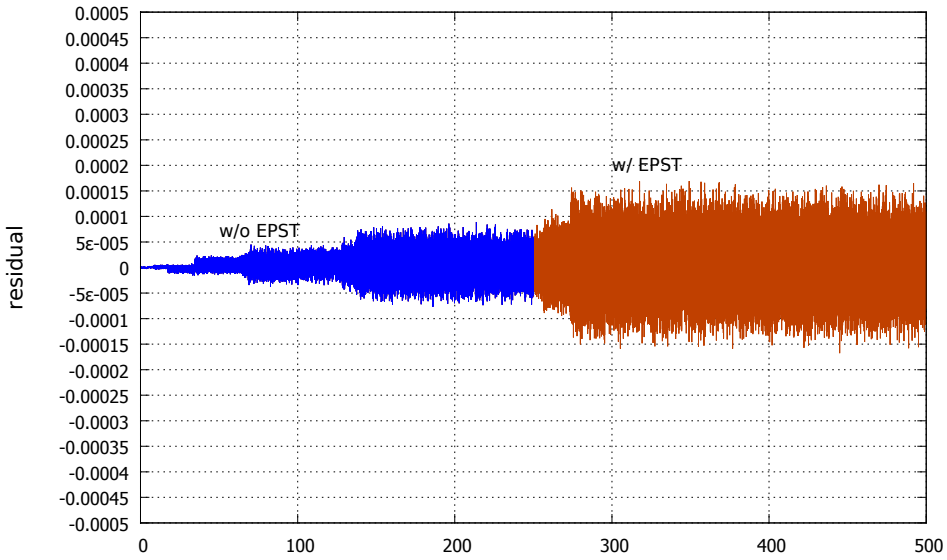

Figure 3.3.4: Search procedure method check for drill system without ST ($\tau \leq 250$) and with ST. The delay state must satisfy Equation (2.4.14), with small residual.

3.4 Discussion

The drilling system described by German *et. al.* [30] was chosen as benchmark case to study ways to manage and mitigate stick-slip. But, during our literature review, we faced the spatial discretization problem, which is that the spatial discretization choice has direct impact on the system stability. For this reason, the stability of the semi-discrete system of equations based on finite element formulation was not studied. Hence, vibration mitigation by the choice of the imposed axial and angular velocities was not possible.

Another option to manage vibrations was to consider a drive system with angular velocity control, or Soft-Torque. The ST control was implemented as an actual spring and damper elements connecting the drive system to the upper drill string end, according to [37]. Both time domain simulations presented the same pattern, with fast development of axial oscillations,

resulting in axial stick. The angular velocity oscillations grow slowly compared to axial oscillations. In particular, the ST delayed the angular oscillations growth compared to the standard drive system. But, the ST case presented backward rotation, and then the simulation stopped.

Regarding to the numerical time integration scheme, we tested simple Forward Euler and Newmark's method. For the small step size used, they did not present differences in the results. But for the Newmark's method, the integration parameters proposed by [8] introduces a (slight) numerical damping into the scheme. For that reason, we kept the Forward Euler as the numerical integration scheme.

A numerical integration based on event driven and variable time step size [9, 54, 16] should be implemented, especially because of the occurrence of stick phases. The current scheme sets the angular velocity equals to zero when it is sufficiently close to it. But with the fixed time step, the axial state correction is compromised. Also the event driven scheme will be very useful to look for backward rotation and bit bounce.

In order to solve for the state dependent delay, instead of solving the implicit non-linear Equation (2.4.14), we looked for the time delay based on the drill-bit angular position. It corresponds to the time taken for the bit to rotate the (constant) angle spanned by two consecutive blades. The evaluated time delay and angular delayed state obeyed Equation (2.4.14) with low residual, showing that the scheme worked as expected.

Chapter 4

Axial Dynamics of Discrete Drilling Models

In this chapter, we address the following question: how does the choice of the drill string spatial discretization impacts its stability? This question arises from the observations of [40], that were briefly presented at the beginning of Chapter 3. To understand the impact of the spatial discretization, first we present the stability of axial motion based on time scale separation (see for example [26]) of the RGD model [29], which allow us to study a simplified partially uncoupled axial and torsional system. The well-known stability for a lumped axial one DOF system is first introduced. Then the stability and time behavior of discrete systems representing the axial dynamics of the drill string is presented, on the basis of a 2 and 3 DOF representation. The behavior of a multi-DOF system is also analyzed. For 2 and 3 DOF, the stability analysis is assessed using semi-analytical tools. For larger order models, stability is conducted with numerical tools, as the use of analytical tools in such case becomes too complicated. Time simulation results for all these models display an interesting phase locking behavior.

The analysis of lumped MDOF models is also interesting from another perspective. Namely, Chapter 3 has revealed that higher flexibility modes are important to describe the instabilities leading to stick-slip oscillations. This raises the question of how the representation of the system with additional DOF (introducing additional flexibility modes) affects such instabilities. This

question is interesting in its own right, but also bears relevance in the scope of constructing models serving as a basis for the future development of controllers outperforming ST, although the latter is outside the scope of this thesis.

4.1 RGD Model

The drill-string in the RGD model is represented by a torsional pendulum for the angular motion and a dead load on a cable for the axial motion (see Figure 4.1.1a), which is excited by the bit-rock interaction law introduced in Section 2.2.2. This model exhibits self-excited vibrations caused by the regenerative effect (and is formulated in terms of delayed differential equations or DDE's). The axial and torsional equations of motion are given by:

$$\frac{\partial^2 u}{\partial \tau^2} = -\psi n_b \left[u\left(1,\tau\right) - u\left(1,\tau-\tau_1\right) + \upsilon_o \hat{\tau}_1\right] - n_b \lambda g\left(\upsilon\right), \tag{4.1.1}$$

$$\frac{\partial^2 \varphi}{\partial \tau^2} + \varphi = -n_b \left[u\left(1,\tau\right) - u\left(1,\tau-\tau_1\right) + \upsilon_o \hat{\tau}_1\right] - n_b \lambda \beta g\left(\upsilon\right). \tag{4.1.2}$$

If we think of the drill-bit physics, oscillations in the axial direction will lead to oscillations in depth-of-cut d (see Figure 2.4.1). Oscillations in d result in oscillations of force W^c and torque T^c (see Equations (2.2.6) and (2.2.8)). Also axial oscillations can result in loss of contact underneath the cutters if the drill bit is moving upward, introducing an additional and important variation in force $\mathbf{W^f}$ and torque $\mathbf{T^f}$ (see Equations (2.2.7) and (2.2.9)). It means that the self-excitation at the bottom-end of the drill-string is oscillatory.

The results from [52] shown in Figure 4.1.1b suggest that axial oscillations trigger angular oscillations as confirmed by a stability analysis [52, 31]. The study of axial motion as an independent system comes from the recognition that the RGD model presents a clear time scale separation between axial and torsional dynamics if the system number ψ is large, as is usually the case. Figure 4.1.1b illustrates the RGD model response for a typical drilling system [52]. The dimensionless quantities describing the problem are $\nu_o = 1.74$, $\omega_o = 5$, $\lambda = 5$, $\beta = 0.3$. The axial motion presents a much smaller period (time scale) than the torsional one. Also in the early time the axial dynamics is well established while the torsional mode has no significant variation. Therefore understanding the axial dynamics is helpful to understand the overall system behavior.

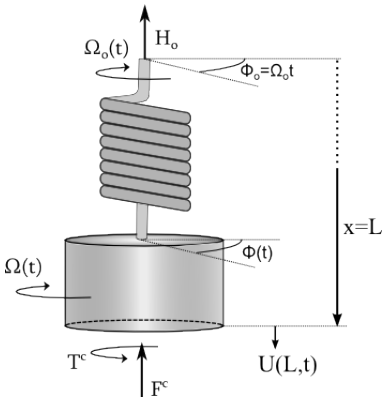

(a) RGD model.

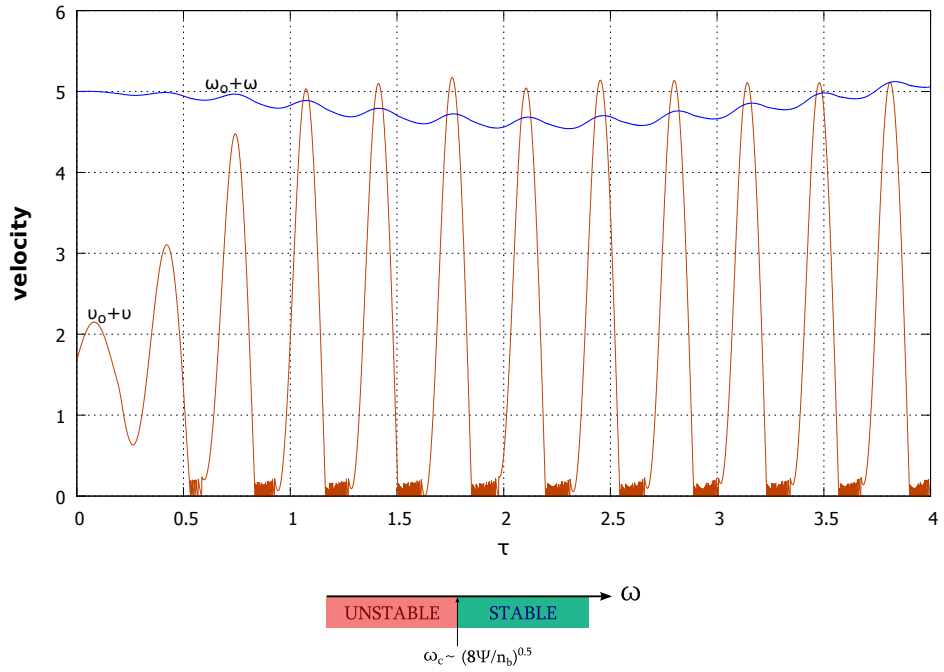

(b) Time scale separation.

Figure 4.1.1: RGD model: (a) system representation, and (b) time evolution with time scale separation for $\mathcal{W}_o = 7$, $\lambda = 5$, $\omega_o = 5$, $\psi = 50$, $\beta = 0.3$, $n_b = 6$, after [52]. Axial motion presents higher frequency compared to torsional one (bottom left), while around the equilibrium point the bit angular speed ω is nearly a constant for a few axial oscillations (bottom right). The axial motion stability can be assessed based on critical angular speed ω_c.

In view of the time scale separation, there is an initial short time when the axial vibrations develop under almost constant angular velocity. Under these conditions we can decouple Equations (4.1.1) and (4.1.2) assuming that within this interval the time delay (i.e. the torsional velocity) is almost constant. Then, for the axial motion, the system is (marginally) stable for an applied angular speed ω_o larger than the critical angular speed $\omega_o^c = \sqrt{8\psi/n_b}$. Otherwise, the system is unstable [52].

The stability of coupled axial and torsional RGD model was further investigated by [20], following the linearization procedure from [36]. Basically the authors concluded that the linear system describing the RGD model always presents unstable motion. On the one hand, if the imposed angular speed ω_o is larger than a critical angular speed ω^c, the system is in a slow regime of instability that is associated with the torsional dynamics. On the other hand, if ω_o is smaller than a critical angular speed ω^c, the system is dominated by the axial dynamics in the so-called fast regime, which is characterized by a fast growth of the oscillations compared to the torsional mode. The critical speed ω^c calculated in [19] was close to the one with constant time delay ω_o^c obtained in [52, 31].

The stability of some classes of second-order autonomous DDE with constant delay was studied by [12, 33], who analytically developed stability charts for DDE based on Pontrjagin conditions [45].

The stability chart for systems described by DDE of the type

$$\ddot{u}(\tau) + p\dot{u}(\tau) + au(\tau) - bu(\tau - 1) = 0$$

is shown in Figure 4.1.2, noting that the scaling of time is such that the time delay is 1. RGD model axial dynamics is defined by Equation (4.1.1), and has the same form of the DDE presented above with $a = b = \psi\left(2\pi/\omega_o n_b\right)^2$ and $p = 0$. Based on the stability chart depicted in Figure 4.1.2, the RGD axial dynamics is marginally stable for $\psi \leq 0.25\left(\omega_o n_b\right)^2$ or unstable for all other values of ψ (noting that $\psi > 0$).

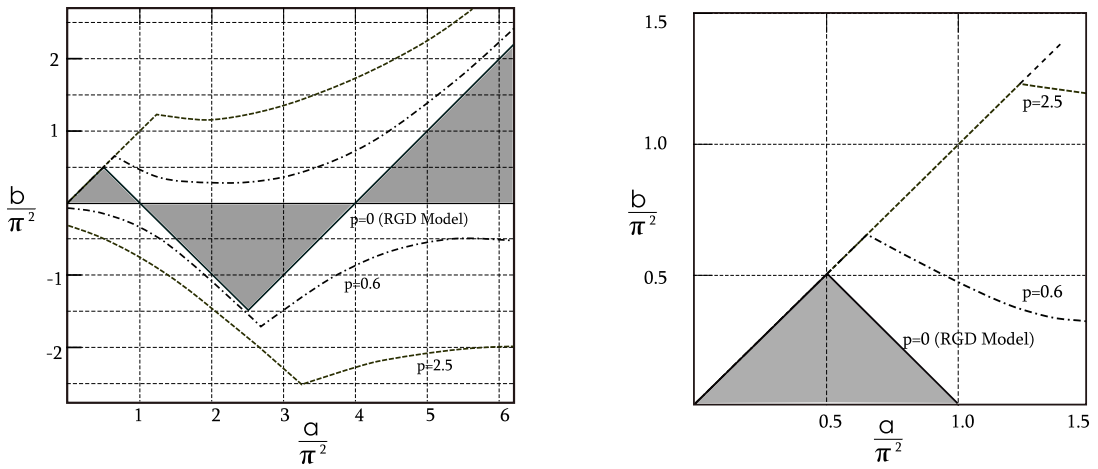

Figure 4.1.2: Stability chart for systems with constant delay $\tau_1 = 1$ and governing equation of type $\ddot{u}(\tau) + p\dot{u}(\tau) + au(\tau) - bu(\tau - \tau_1) = 0$. Inside the curves, the shaded area represents stable region for $p = 0$, and for $p > 0$ the stable region is within curves (adapted from [12, 33]). Close view on the right, making possible to define RGD model instability boundary.

According to the stability chart shown in Figure 4.1.2, the system is asymptotically stable if the parameters fall within the shaded area. A lumped model with $a > b$ describes a system with an axial spring linking the mass to the top boundary condition [11, 42]. Hence, the axial dynamics can be stable if the axial displacement is imposed at the surface, instead of a force. For such a case, the axial equation of motion is written as $\ddot{u}(\tau) + (\psi + \kappa_d)\, u(\tau) - \psi u(\tau - \tau_1) = 0$ for constant angular velocity and $\kappa_d > 0$ represents the presence of the spring. In particular, if $k_d < 0$ (or $a < b$), the spring presents a negative stiffness, which is not physically relevant. We also can see that an introduction of a damping-like term into the second order DDE enlarges the stable area (the curves for which $p \neq 0$).

4.2 Axial Motion of a 2 DOF System

4.2.1 Equations of Motion

In the previous section, we described how the axial dynamics triggers the system instability in the RGD model. The stability and time evolution for a 2 axial DOF model is now studied. This model, depicted in Figure (4.2.1a), represents a system with constant angular velocity Ω_o imposed at the surface and with masses M_1 and M_2 rotating at the same uniform velocity Ω_o. The total system mass and stiffness was kept constant, *i.e.* the 2 DOF discrete model is just another representation of the same drilling system already presented in the previous section. The equations of motion are described in terms of the parameters a and b to make it possible to compare this model with the 1 DOF model. The mass, whose position is given by $U_2(t)$ is excited by the force from the bit/rock interface for a sharp bit (no friction force component). The parameter ϵ describes the relation between the two masses and the system total mass M, *i.e.*, $M_1 = \epsilon M$, and $M_2 = (1-\epsilon) M$. Also ϵ relates the two spring stiffness to the overall stiffness k as $k_1 = k/\epsilon$ and $k_2 = k/(1-\epsilon)$. To conserve the system total mass and stiffness, ϵ is defined as $\epsilon \in (0,1)$.The governing equations are written in the following form:

$$\left\{ \begin{array}{c} \ddot{u}_1(t) \\ \ddot{u}_2(t) \end{array} \right\} + \mathbf{K} \left\{ \begin{array}{c} u_1(t) \\ u_2(t) \end{array} \right\} + \mathbf{B} \left\{ \begin{array}{c} u_1(t-1) \\ u_2(t-1) \end{array} \right\} = \left\{ \begin{array}{c} 0 \\ 0 \end{array} \right\} \tag{4.2.1}$$

$$\mathbf{K} = \left[\begin{array}{cc} \left(\frac{1}{1-\epsilon} + \frac{1}{\epsilon}\right) \frac{\kappa_d}{\epsilon} & -\frac{\kappa_d}{(1-\epsilon)\epsilon} \\ -\frac{\kappa_d}{(1-\epsilon)^2} & \left(\frac{1}{1-\epsilon}\right)\left(\frac{\kappa_d}{1-\epsilon} + n_b\psi\right) \end{array} \right], \; \mathbf{B} = -\left[\begin{array}{cc} 0 & 0 \\ 0 & \frac{n_b\psi}{1-\epsilon} \end{array} \right]. \tag{4.2.2}$$

In the above equations, $\kappa_d = t_*^2 EA_d/(L_{DP}M)$ represents the squared ratio of two time scales, i.e., one corresponding to t_* and the other to the first natural axial period of oscillations of the drill-pipes. For $\epsilon \to 0$ or $\epsilon \to 1$, we have $M_1 \to 0$ or $M_2 \to 0$ and $k_1 \to \propto$ or $k_2 \to \propto$, and we thus recover the 1-DOF model with a spring connecting the mass to the top prescribed boundary condition. To recover the original parameters from [12] we define $\epsilon \to 0$ or $\epsilon \to 1$, $\kappa_d + \kappa_r = a$, and $\kappa_r = n_b\psi = b$.

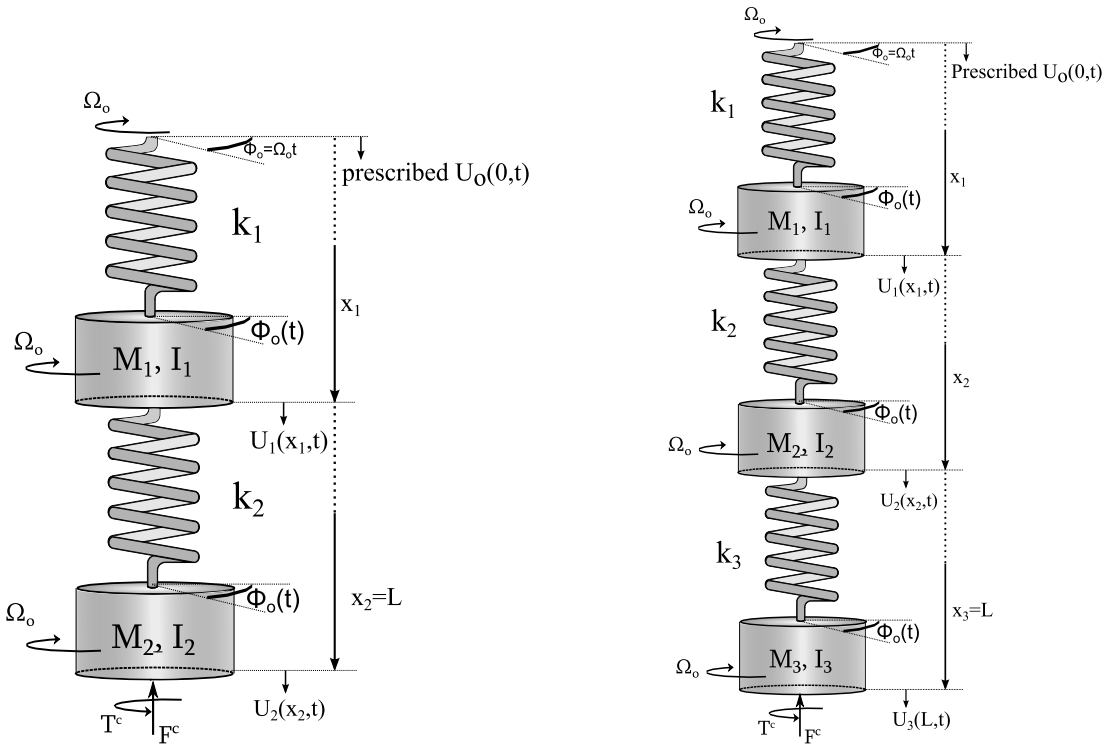

(a) 2-DOF axial model.

(b) 3-DOF axial model.

Figure 4.2.1: Multi DOF axial model: (a) Two axial oscillators model; (b) Three axial oscillators model.

4.2.2 Stability Analysis

The stability analysis has been performed based on Pontrjagin conditions [45], which is presented in more details in Appendix C.1. The D-subdivision method [34], giving the D-Curves, and a numerical method to find out the right-most eigenvalues of the characteristic polynomial-exponential [63] were also used when it was not possible to find the parameters satisfying Pontrjagin conditions for stability.

The D-Curves are a set of curves in the parameter space associated with a particular imaginary conjugate pair of characteristic exponents in the form $z = iy$, where y is the angular

frequency of oscillation. Inside a region bounded by two adjacent D-Curves the system is characterized by the same number of unstable exponents (the D-Curves correspond to a particular combinations of parameters for which the exponents cross the imaginary axes of the complex plane). Knowledge of the number of unstable exponents for one particular point inside a region limited by D-Curves in the parameter space is sufficient to define the system stability inside that region.

Pontrjagin conditions represent stability criteria for the characteristic exponential polynomial $H(z)$, $z \in \mathbb{C}$, that describes a delayed system. Assuming that $z = iy$, $y \in \mathbb{R}$, the characteristic exponential polynomial can be rewritten as $H(iy) = F(y) + iG(y)$. If $H(iy)$ has a principal (see Appendix C.1) term, then all the roots of $H(iy)$ have a negative real part if the following conditions are satisfied:

1. All zeros of $F(y)$ (or $G(y)$) are real, and;
2. For every zero of $F(y)$ (or $G(y)$) , $F'(y)G(y) < 0$ (or $F(y)G'(y) > 0$) holds.

For the characteristic polynomial pertaining to Equation (4.2.1), it is not difficult to show that all zeros of $G(y)$ are real. Then we have to look for which values of (a, b) condition 2 above holds to define the system stability. The stability analysis is then presented in the same parametric space (a, b) used to describe the single axial oscillator case, presented in Figure 4.1.2. We can define a as the term multiplying the current axial state $u(\tau)$, and b as the one multiplied by the delayed stated $u(\tau - \tau_1)$. The stability charts in the original parameter space (a, b) are shown below, for some values of ϵ. The triangle in black shows the stability boundaries, already presented in Figure 4.1.2, which allow us to compare the 2-DOF and 1-DOF approximations. The curves in both pictures represent loci where there are two imaginary eigenvalues, *i.e.* $z = \pm iy$, except for the line $a = b$ representing the locus where z is identically equal to zero.

We can see that for small values of ϵ the stability boundary is almost the same for the 1-DOF model. In fact, a small ϵ means that our system representation is really close to the 1-DOF one, with a really rigid upper spring connecting the imposed top boundary condition to a small mass. The lower mass M_2 and the lower spring k_2, which accounts for almost all system mass and compliance, are directly subjected to the excitation provided by the bit/rock interaction.

When ϵ increases, the stability sub-region near the origin of the parametric space becomes

itself disconnected. A narrow stability band exists close to the line $a = b$. This comes from the fact that the locus $z = \pm i\pi$ (see Figure 4.2.2) defined by the projection of a hyperbolic paraboloid on plane (a, b), goes apart with increasing ϵ.

Let us consider two similar representations, with $\epsilon = 0.2$ and $\epsilon = 0.8$, respectively. In both cases, the eigenvalue problem without the time delay term is the same. But the stability regions showed in Figure 4.2.2 changes drastically. This result suggests that the response is not only a function of the discrete system eigenmodes (otherwise the stability for these two cases should be the same). The delay introduced by the bit/rock relationship evidently plays a key role in the overall system stability.

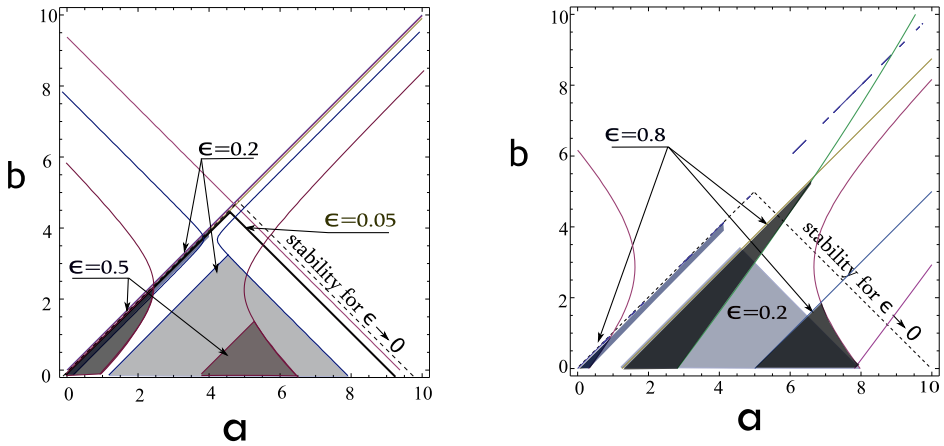

Figure 4.2.2: Stability charts for 2-DOF system in $a - b$ parameter space defined by Equation(4.2.1) with $\epsilon = 0.005, 0.2, 0.5$ on the left and $\epsilon = 0.2, 0.8$ on the right. On the left, darkest shadow represents stability for $\epsilon = 0.5$, while on the right, it represents stability for $\epsilon = 0.8$. The curves represent loci characterized by a pair of purely imaginary eigenvalues, exception for the line $a = b$, where the both real and imaginary parts are identically null (note: only selected curves are presented for the sake clarity).

The system with identical masses and springs ($\epsilon = 0.5$) was further studied, because it is the basis of the representation of the drilling system, with equal masses and springs. First we

extended the space parameter region, where we studied the stability. Figure 4.2.3a shows three disconnected areas representing stable regions for the axial system. Figure 4.2.3b shows a closer look of the parameter space and a more detailed stability chart. This figure shows two paths defined by lines $\mathcal{L}_1$ and $\mathcal{L}_2$ along which the evolution of the right-most eigenvalues was studied. It also shows the so-called D-Curves, which are labeled with the value of the corresponding imaginary eigenvalue pair. The only exception is for the line where $a = b$, in which there is only one eigenvalue crossing the imaginary axis. In this particular case, both real and imaginary parts are zero. This particular eigenvalue is here denoted as z_o.

To understand how the right-most eigenvalues evolve with the system parameters a and b, these two parameters were varied according to the paths defined by $\mathcal{L}_1$ and $\mathcal{L}_2$. Usually, at most one pair of eigenvalues crosses the imaginary axis within both $\mathcal{L}_1$ and $\mathcal{L}_2$. This eigenvalue pair is herein denoted z_1 and $\bar{z}_1$. Cases A_1 and A_2, depicted in Figure 4.2.3b, show where another eigenvalue pair, referred to as z_2 and $\bar{z}_2$, crosses the imaginary axis instead of z_1 and $\bar{z}_1$. A third eigenvalue pair was also found. This pair is always stable and its path is no longer studied.

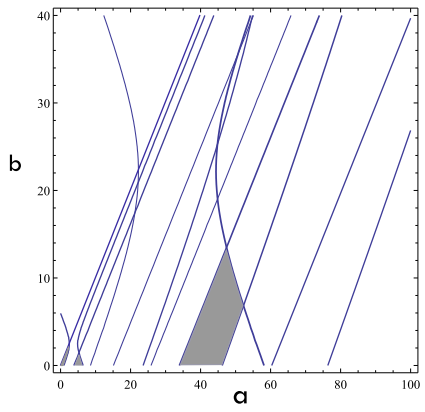

(a) Stability of two DOF model.

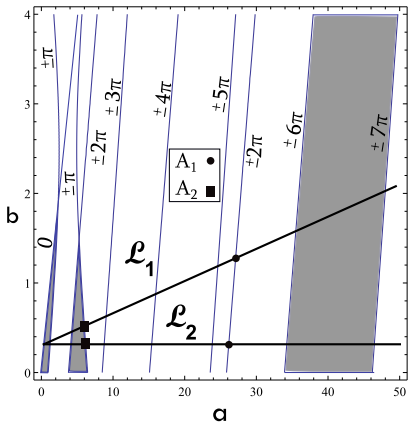

(b) Stability of two DOF model for extended parameter space.

Figure 4.2.3: Stability chart for 2-DOF of system with equal masses and springs: (a) stable regions defined by shaded areas, and (b) paths $\mathcal{L}_1$ and $\mathcal{L}_2$ over which the most-right eigenvalues evolution were studied. The values over the lines show $\Im(z)$ for which $\Re(z) = 0$. Most right eigenvalues for A_1 and A_2 are showed in detail in Figure 4.2.4.

The overall eigenvalues evolution along $\mathcal{L}_1$ and $\mathcal{L}_2$ is shown in Figure 4.2.4. The arrows shows the eigenvalues evolution for (a, b) moving from right to left. Cases A_1 and A_2 are depicted by diamonds. For unstable eigenvalues, the path is red. For stable, it is blue. The light green color means that the exponent z_2 is located on the imaginary axis, i.e., $\Re(z_2) = 0$. The detailed view in Figure 4.2.4a shows the location of eigenvalues z_1 and z_2 for case A_2, and in Figure 4.2.4b shows z_2 when (a, b) is at the right end of $\mathcal{L}_2$. Pair $(z_1, \bar{z}_1)$ crosses the imaginary axis six times at $\pm q\pi$, $q = 1, .., 7$, while $(z_2, \bar{z}_2)$ crosses only at $\pm\pi$ and $\pm 2\pi$.

Location of pairs $(z_1, \bar{z}_1)$ and $(z_2, \bar{z}_2)$ defines the stability of the system. If both are in the left-hand side of the complex plane, *i.e.* $\Re(z_p) < 0$, $p = 1, 2$, the system is defined as stable. The pair z_1 and $\bar{z}_1$ crosses most often the imaginary axis. Only at points A_1 and A_2 in Figure 4.2.3b, the crossing takes place for pair $(z_2, \bar{z}_2)$. If we are moving over paths $\mathcal{L}_1$ and $\mathcal{L}_2$ from right to left end, the pair $(z_2, \bar{z}_2)$ is stable until we reach point A_1. The first eigenvalues crossing is z_1 at $\pm 7\pi$, and the next crossing occurs when z_1 is at $\pm 6\pi$. Between these two crossings, $(z_1, \bar{z}_1)$ are stable, which means that the system is stable (remembering that z_2 and its conjugate are stable and did not cross the imaginary axis yet).

The next crossing point is defined by A_1, with z_2 ,$\bar{z}_2$ crossing at $\pm 2\pi$. From now on, the system is unstable until we reach A_2. The pair z_1,$\bar{z}_1$ crosses at $\pm 5\pi$, $\pm 4\pi$, and $\pm 3\pi$. At A_2, z_2 crosses to the left side of the complex plane at $\pm\pi$, and from now on z_2 and $\bar{z}_2$ are always stable. Also at point A_2, pair z_1,$\bar{z}_1$ is stable, so does the system. The last two $(z_1, \bar{z}_1)$ crossing are at $\pm 2\pi$ (becoming unstable) and $\pm\pi$ (becoming stable), respectively.

At $a = b$, $(z_1, \bar{z}_1)$ and $(z_2, \bar{z}_2)$ collapse to a single eigenvalue located at the real axis. Since z_o is always located over the real axis, in $a = b$ we have three eigenvalues over the real axis, and one of them is located at the origin. This condition is represented by the triangles of Figure 4.2.4.

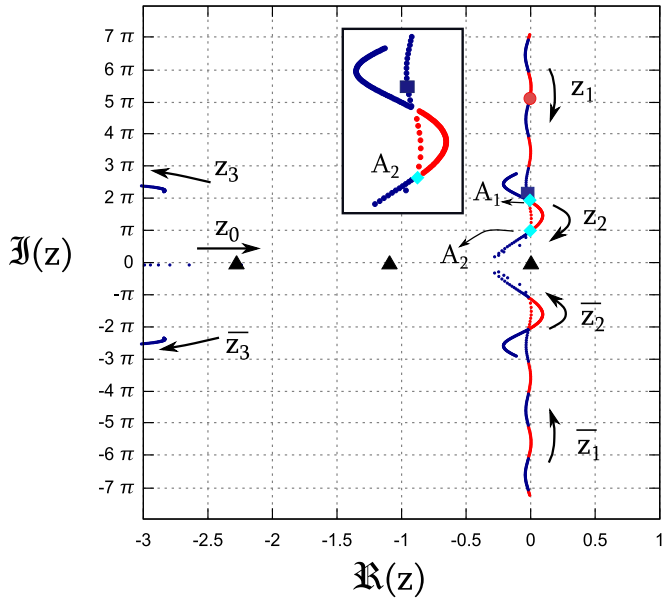

(a) Right-most eigenvalues for path $\mathcal{L}_1$.

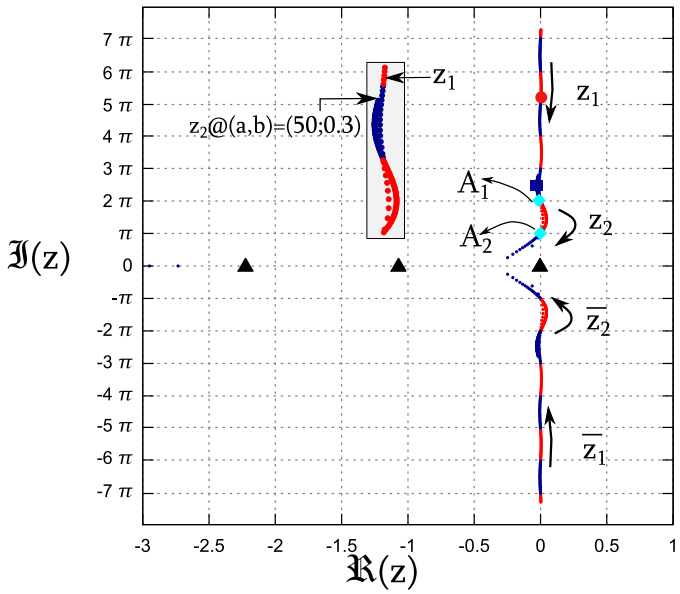

(b) Right-most eigenvalues for path $\mathcal{L}_2$.

Figure 4.2.4: Right-most eigenvalues evolution for (a, b) changing over lines $\mathcal{L}_1$ and $\mathcal{L}_2$ from right to left end. Diamonds represent positions of eigenvalues z_1 and z_2 at cases A_1 and A_2. Triangles represent the eigenvalues positions for $a = b$. Red and blue path represent instability and stability respectively. The diamonds represent locations at which $\Re(z_2) = 0$. (a) detail shows location of z_1 and z_2 for case A_2 in $\mathcal{L}_1$; (b) detail shows z_2 location for $(a, b) = (50; 0.3)$ in $\mathcal{L}_2$.

4.2.3 Time-Domain Simulations

Time-domain simulations were performed in reference to the stability diagrams presented above, and the solutions agreed with the stability conditions, as can be seen in Figures 4.2.5. Three different cases were studied in time-domain. Among then, only one case is located in a stable area in the stability chart (Figure 4.2.5e), while the other two are located in the unstable regions (Figures 4.2.5a and 4.2.5c). Interestingly the system presents phase locking, *i.e.,* the oscillators are vibrating at the same common frequency, with or without phase shift [53, 57]. For systems represented in the parametric space farthest from the origin, the oscillator are in phase, *i.e.*,$|\phi_i - \phi_j| \approx 0$. However, for parameter values closer to the origin, the oscillators present a phase shift, *i.e.,* $|\phi_i - \phi_j| \approx \pi$. Figure 4.2.5 shows the results for two different points in the parameter space. Figure 4.2.5a illustrates the response for a system represented by $(a, b) = (6.9, 2.96)$. It is an unstable system according to Figure 4.2.2, and the oscillations grow exponentially. But the two oscillators are in phase. Figure 4.2.5e shows the time response for a system with $(a, b) = (0.35, 0.3)$, which is stable according Figure 4.2.2. Indeed the time response is asymptotically stable, but the masses are vibrating with a π-phase shift before vanishing. For the case $(a, b) = (3.45, 2.96)$ the system is unstable and the oscillators are out-of-phase (see Figures 4.2.5c and 4.2.5d).

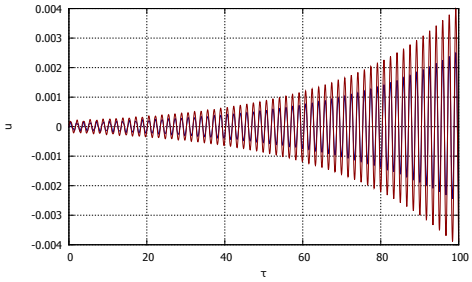

(a) Two-oscillator model in phase.

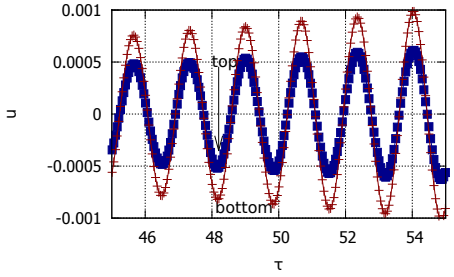

(b) Two-oscillator model in phase detail.

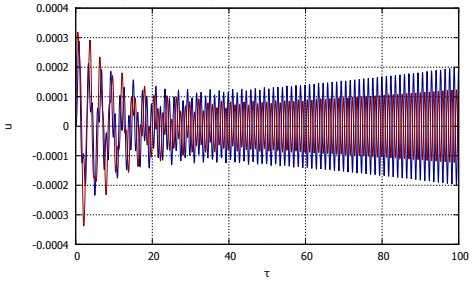

(c) Two-oscillator model out-of-phase.

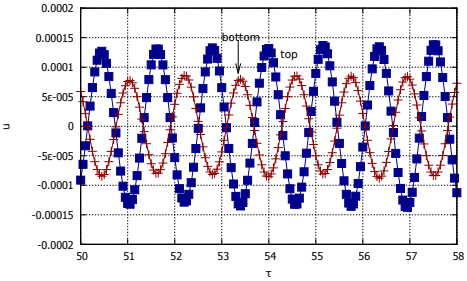

(d) Two-oscillator model out-of-phase. detail.

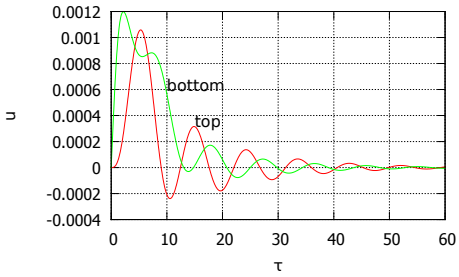

(e) Stable two-oscillator model.

Figure 4.2.5: Time response for 2-oscillator model systems located at: (a) and (b) $(a, b) = (6.9, 2.96)$, (c) and (d) $(a, b) = (3.45, 2.96)$, and (e) $(a, b) = (0.35; 0.3)$.

To understand the phase rule between the oscillators, we define the eigenvalues as $z = x + iy$, $x, y \in \mathbb{R}$ and describe the solutions by:

$$u_1 = U_1 e^{zt+i\phi_1}$$

$$u_2 = U_2 e^{zt+i\phi_2}.$$

Substituting the above equations into Equation (4.2.1) we obtain the following non-linear system of equations:

$$
\begin{aligned}
&x^2 - y^2 + 4\alpha(2 - r\cos\phi) = 0 \\
&xy - 2\alpha r \sin\phi = 0 \\
&x^2 - y^2 + 4\alpha(1 - r^{-1}\cos\phi) + 2b(1 - e^{-x}\cos x) = 0 \\
&2xy + 4\alpha r^{-1}\sin\phi + 2be^{-x}\sin x = 0,
\end{aligned}
$$

with $r = U_1/U_2$ and $\phi = \phi_1 - \phi_2$. For $\mathcal{L}_1$ and $\mathcal{L}_2$, we know the right-most eigenvalues values (x, y). Solving the above system for ϕ yields:

$$\cot\phi = \frac{x^2 - y^2 + 8\alpha}{2xy}$$

From Figures 4.2.4a and 4.2.4b we note that x is $\mathcal{O}\left(10^{-1}\right)$ and y is $\mathcal{O}\left(10^{1}\right)$ at the right ends of $\mathcal{L}_1$ and $\mathcal{L}_2$. It means that $\phi \to 0$ or $\phi \to \pi$. Specially when z_1 is the dominant mode, x is $\mathcal{O}\left(10^{-2} - 10^{-3}\right)$, α and y are $\mathcal{O}\left(10^{0}\right)$ and $\mathcal{O}\left(10^{1}\right)$, respectively. When z_2 presents real and imaginary parts of the same order of magnitude, both z_1 and z_2 are stable. Then the imaginary part of z_1 is $\mathcal{O}\left(10^{0}\right)$. Hence, the masses can oscillate only in or out-of-phase.

4.3 Axial Motion of 3-DOF System

The perturbed equations of motion were derived so as to keep the overall mass and stiffness constant, as done before. Parameter ϵ establishes the relation between total and individual masses and stiffnesses. The equation of motion can be written as:

$$
\begin{Bmatrix} \ddot{u}_1(t) \\ \ddot{u}_2(t) \\ \ddot{u}_3(t) \end{Bmatrix} + \mathbf{K} \begin{Bmatrix} u_1(t) \\ u_2(t) \\ u_3(t) \end{Bmatrix} + \mathbf{B} \begin{Bmatrix} u_1(t-1) \\ u_2(t-1) \\ u_3(t-1) \end{Bmatrix} = \begin{Bmatrix} 0 \\ 0 \\ 0 \end{Bmatrix} \tag{4.3.1}
$$

$$
\mathbf{K} = \begin{bmatrix} \frac{2\kappa_d}{\epsilon^2} & -\frac{\kappa_d}{\epsilon^2} & 0 \\ -\frac{\kappa_d}{\epsilon^2} & \frac{2\kappa_d}{\epsilon^2} & -\frac{\kappa_d}{(1-2\epsilon)\epsilon} \\ 0 & -\frac{\kappa_d}{(1-2\epsilon)^2} & \frac{1}{1-2\epsilon}\left(\frac{\kappa_d}{1-2\epsilon} + n_b\psi\right) \end{bmatrix}, \mathbf{B} = \begin{bmatrix} 0 & 0 & 0 \\ 0 & 0 & 0 \\ 0 & 0 & \frac{n_b\psi}{1-2\epsilon} \end{bmatrix}.
$$

In this case it, is not easy to apply the Pontrjagin conditions for the stability analysis. Hence, the D-Subdivision method was applied to determine the conditions for which a conjugate eigenvalue pair crosses the imaginary axis. Then, using a numerical MatLab package [63], we search for the number of unstable exponents inside each region defined by the D-Curves. The resulting stability chart is depicted in Figure 4.3.1 below. For comparison, the case with only one mass is presented by the black line.

We note again that for small value of ϵ the system behaves almost like the 1-DOF presented earlier (but the stable area is reduced compared to the 2-DOF case). When the three oscillators are identical, the stable region reduces even more when compared to the 2-DOF case, leaving a narrow stable area.

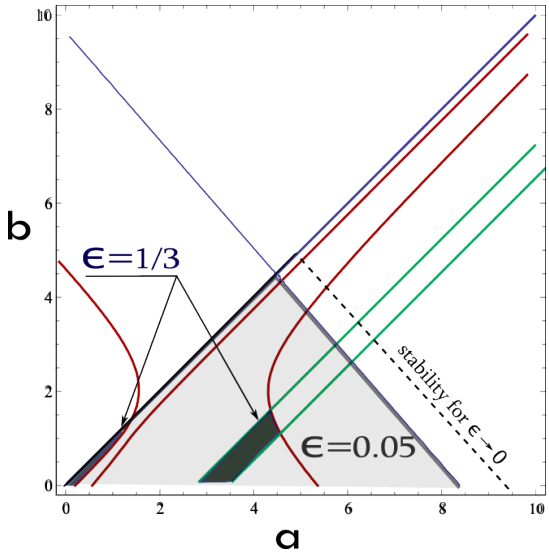

Figure 4.3.1: Stability chart for 3-DOF system with two different configurations.

Time simulations for 3-DOF also show phase locking. If the system parameters are close to the line $a = \pi^2 - b$, which is the right boundary of the stable region for $\epsilon \to 0$ in Figure 4.3.1, all oscillators are in phase. If the system is located more on the left side, close to the line $a = b$, the oscillators are out-of-phase. During transient motion, the motions of the oscillators

are delayed compared to each other. It means that a compressional wave is propagating through them. After that, the oscillations follow eventually an in or out-of-phase pattern.

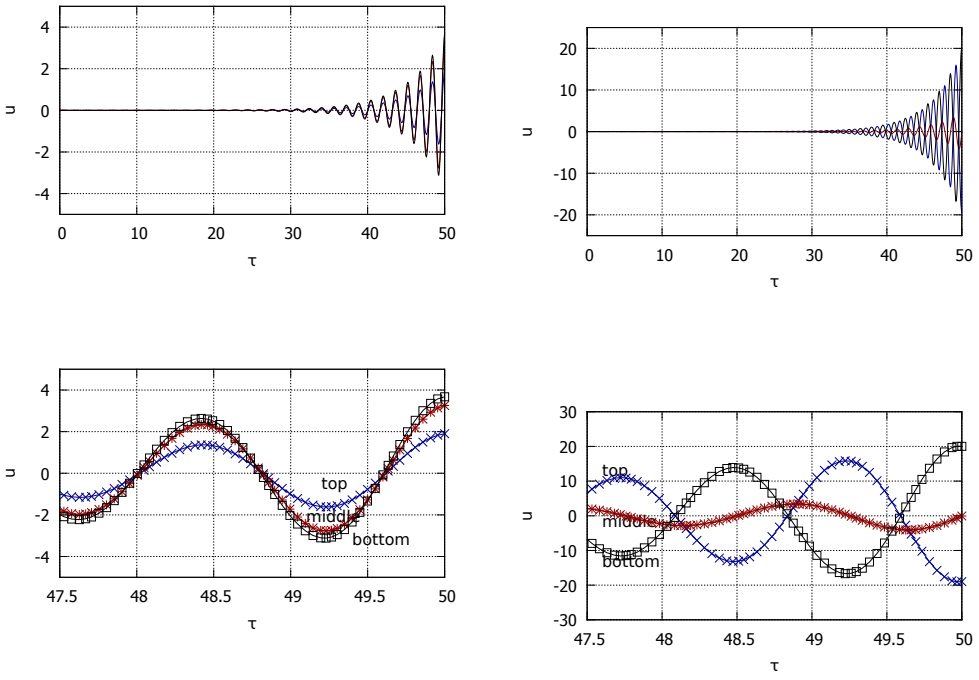

(a) (b)

Figure 4.3.2: Time response for 3-DOF system located at: (a) $(a, b) = (6.9, 2.96)$, (b) $(a, b) = (3.45, 2.96)$.

4.4 Axial Motion of Multi-DOF System

Suppose that we have a system with N oscillators. The individual masses are $M_i = \epsilon_1 M$ for $i = 1, 2, .., N-1$, and the bottom mass $M_N = (1-(N-1)\epsilon_1) M$, conserving the system total mass. The same is done for the spring stiffness connecting the masses, $k_i = EA_d/(L_d \epsilon_2)$ for $i = 1, 2, .., N-1$ and the bottom spring is $k_N = EA_d/(1-(N-1)\epsilon_2) L_d$. The system of equations of motion is written in terms of the dimensionless perturbed displacements u_i,

$i = 1, 2, .., N$ as:

$$\begin{Bmatrix} \ddot{u}_1 \\ \ddot{u}_2 \\ \vdots \\ \ddot{u}_{N-1} \\ \ddot{u}_N \end{Bmatrix} + \mathbf{K} \begin{Bmatrix} u_1 \\ u_2 \\ \vdots \\ u_{N-1} \\ u_N \end{Bmatrix} - \mathbf{B} \begin{Bmatrix} \tilde{u}_1 \\ \tilde{u}_2 \\ \vdots \\ \tilde{u}_{N-1} \\ \tilde{u}_N \end{Bmatrix} = \begin{Bmatrix} 0 \\ 0 \\ \vdots \\ 0 \\ 0 \end{Bmatrix}, \tag{4.4.1}$$

with the non-zeros entries for matrices $\mathbf{K}$ and $\mathbf{B}$ written as:

$$\mathbf{K} = \begin{bmatrix} \frac{2\kappa_d}{\epsilon_1\epsilon_2} & \frac{-\kappa_d}{\epsilon_1\epsilon_2} & 0 & ... & 0 \\ \frac{-\kappa_d}{\epsilon_1\epsilon_2} & \frac{2\kappa_d}{\epsilon_1\epsilon_2} & \frac{-\kappa_d}{\epsilon_1\epsilon_2} & ... & 0 \\ ... & ... & ... & ... & ... \\ & & & \frac{\kappa_d}{\epsilon_1}\left[\frac{1}{\epsilon_2} + \frac{1}{1-(N-1)\epsilon_2}\right] & \frac{-\kappa_d}{\epsilon_1 - (N-1)\epsilon_1\epsilon_2} \\ & & & \frac{-\kappa_d /}{[1-(N-1)\epsilon_1][1-(N-1)\epsilon_2]} & \frac{1}{1-(N-1)\epsilon_1}\left(\frac{\kappa_d}{1-(N-1)\epsilon_2} + n_b\psi\right) \end{bmatrix}$$

$$\mathbf{B} = \begin{bmatrix} 0 & 0 & 0 & ... & 0 \\ 0 & 0 & 0 & ... & 0 \\ 0 & 0 & 0 & ... & 0 \\ ... & ... & ... & ... & ... \\ 0 & 0 & 0 & ... & \frac{n_b\psi}{1-(N-1)\epsilon_1} \end{bmatrix}.$$

The semi-analytical stability analysis is not presented here for $N \geq 4$, due to its complexity and also because a stability analysis of a system of three identical oscillators shows that there is almost no stable area. The dynamics for a system with 10 identical oscillators ($\epsilon_1 = \epsilon_2 = 0.1$) also presents a synchronous pattern, as shown in Figure 4.4.1. For some systems, all the oscillators are in-phase (Figure 4.4.1a). But for other systems (as in Figure 4.4.1b), there exists two groups of oscillators, a lower and upper one which are internally in phase, but the two groups are out-of-phase. In both cases, the transient vibrations reflect the propagation of a wave. The excitation from the bit/rock interface propagates up and down through the oscillators, which eventually become synchronized.

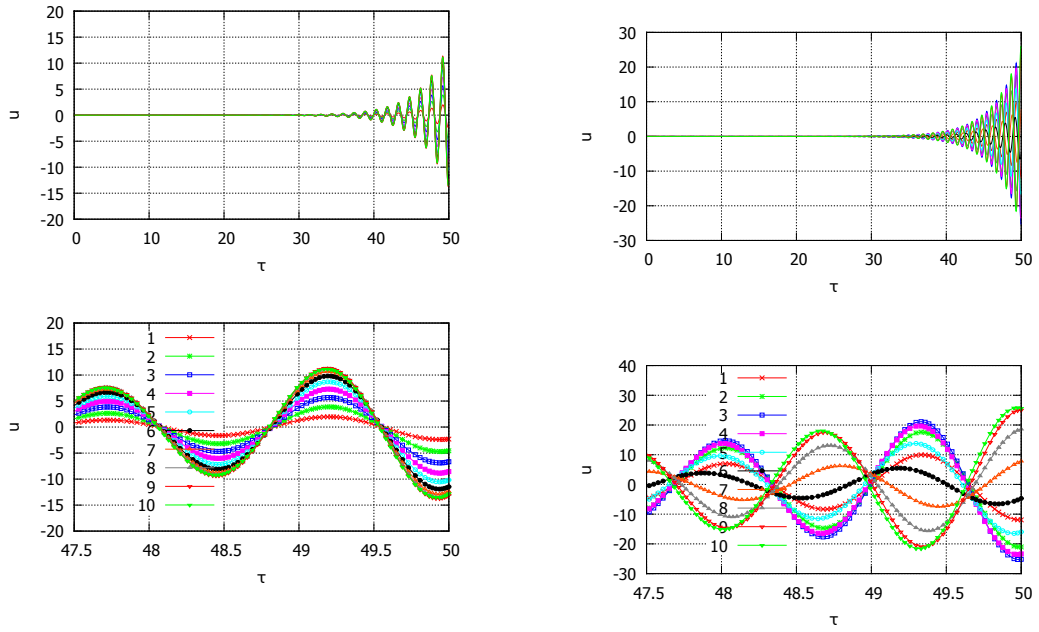

(a)

(b)

Figure 4.4.1: Masses displacement time evolution for 10-DOF system located at: (a) $(a, b) = (6.9, 2.96)$, (b) $(a, b) = (3.45, 2.96)$. In the first case, all masses are closely in-phase, while in the second case are two different clusters moving out-of-phase, with masses within each cluster moving in-phase. Masses M_1 to M_5 composes one in-phase cluster, while the others composes other cluster.

4.5 Discussion

In this chapter, we studied how the spatial discretization of a given drilling system affects the overall dynamical behavior. Based on the time scale separation between the axial and torsional dynamics, the axial dynamics of the drilling system with a sharp bit was uncoupled from the angular dynamics, and hence studied separately. The semi-analytic stability study of the drilling system showed that the system axial stability changes within the same parameter space, when

refining its discrete spatial representation. For instance, for two equivalent 2-DOF systems, where the masses, springs, and eigenfrequencies were the same, but with elements swapping position in relations to the BC's, the stability analysis showed a considerable change in the stable area. Moreover, increasing the number of DOF's, for instance from 2 to 3, resulted in a more unstable system. Although the Pontrjagin's conditions make it possible to study the stability of a characteristic exponential-polynomial of any order, the complexity faced to study the axial system with 3-DOF did not encourage us to perform the same analytic study to assess system stability with larger number of DOF's.

For a system represented by a 2-DOF model with equal masses and springs, the evolution of the right-most eigenvalues when varying linearly the system parameters was studied. This study showed the possibility of phase locking between oscillators, i.e. the phase difference between oscillators remains constant over time during the steady-state response. Even more interesting, the studied showed that the oscillators are able to be approximately in- or 180^oout-of-phase.

The time simulation of the drill string axial motion showed that phase-lock pattern, also for a larger number of DOF's. For cases with 3 and 10 DOF's, two interesting motion patterns occurred. In the first one, all masses were in phase. In the second pattern, the drill string top and bottom were in out-of-phase motion. We can make a parallel between the 3-DOF and 10-DOF models response. For the 10 DOF model, the top masses cluster presented an in-phase motion, as well as the bottom masses cluster. But these two cluster were in an out-of-phase motion compared to each other. Compared to the 3-DOF model representation, it means that the top cluster in the 10-DOF model is represented by the top mass in the 3-DOF model. The same occurred for the bottom cluster, represented by the bottom mass in the 3-DOF model. But in both cases, there was a mass located at the center (mass 2 in the 3-DOF, and mass 6 in the 10-DOF models) with minimum displacement compared to the others.

Now, we have to look if the stability of a coupled system is also affected by the spatial discretization, and if there is any phase locking pattern, which is the subject of the next chapter.

Chapter 5

Coupled Dynamics of Discrete Drilling Models

In this chapter, we study the coupled axial and torsional dynamics of a discrete representation of the drilling system that consists of two axial and two torsional oscillators, as depicted in Figure 5.1.1. This system has four DOF's and is analyzed in detail in Section 5.1. We also present in Section 5.2 a limiting case system, consisting of a semi-infinite drill-string with a lower BC corresponding to the bit/rock interface law. The latter study bears relevance for the top BC that avoids wave reflection (both axially and torsionally). Herewith we can investigate how such BC affects the drill-string dynamics with the down-hole bit/rock interface law.

5.1 Coupled dynamics of a two-oscillator system

The drilling system is modeled as two identical axial and torsional oscillators, *i.e.*, $M_1 = M_2 = \frac{1}{2}M$, $k_1 = k_2 = 2k$, $I_1 = I_2 = \frac{1}{2}I$, $k_1 = k_2 = 2k_{dp}$, and $C_1 = C_2 = 2C_{dp}$. The imposed surface BC are constant axial and angular velocities, and the bottom BC is defined by the bit/rock interface law. The axial and torsional displacements are denoted by U_i and Φ_i, respectively.

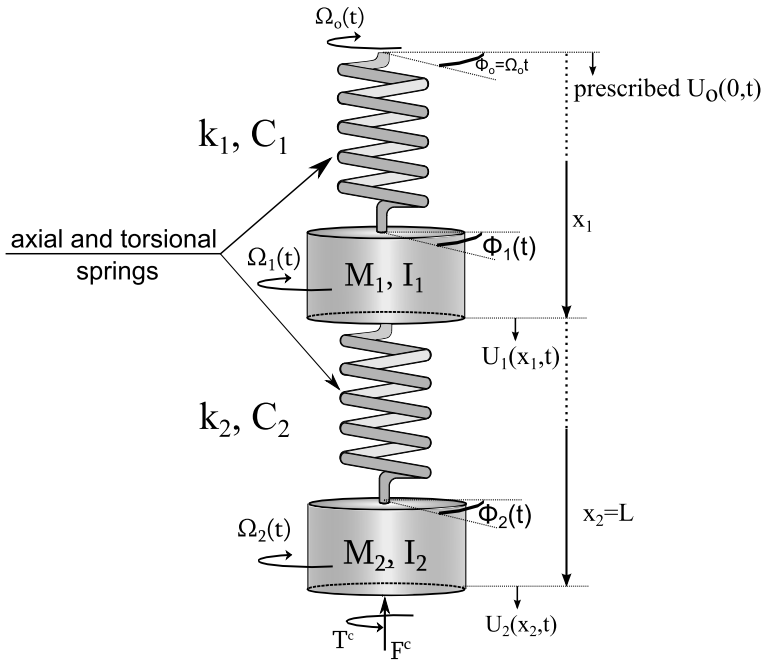

Figure 5.1.1: Two oscillators discrete model for coupled axial-torsional vibrations. Axial and torsional springs and masses are identical, and defined in such a way as to maintain the system axial and torsional compliances, mass and inertia.

For a discrete system with equal masses and compliances the dimensionless perturbation EOM reads:

$$\left\{ \begin{array}{c} \ddot{u}_1(\tau) \\ \ddot{u}_2(\tau) \\ \ddot{\varphi}_1(\tau) \\ \ddot{\varphi}_2(\tau) \end{array} \right\} = \mathbf{A_o} \left\{ \begin{array}{c} u_1(\tau) \\ u_2(\tau) \\ \varphi_1(\tau) \\ \varphi_2(\tau) \end{array} \right\} + \mathbf{A_1} \left\{ \begin{array}{c} u_1(\tau - \tau_1) \\ u_2(\tau - \tau_1) \\ \varphi_1(\tau - \tau_1) \\ \varphi_2(\tau - \tau_1) \end{array} \right\} + g(v)\,\lambda \left\{ \begin{array}{c} 0 \\ 1 \\ 0 \\ \beta \end{array} \right\}, \tag{5.1.1}$$

where $\mathbf{u} = \{u_1, u_2, \varphi_1, \varphi_2\}^T$ represents the perturbations of the motion of the oscillators with

respect to the steady-state solution. The matrices $\mathbf{A_o}$ and $\mathbf{A_1}$ are defined as follows:

$$\mathbf{A_o} = \begin{bmatrix} -8\kappa_d & 4\kappa_d & 0 & 0 \\ 4\kappa_d & -2\left(2\kappa_d + n_b\psi\right) & 0 & 2n_b\psi\alpha_o \\ 0 & 0 & -8 & 4 \\ 0 & -2n_b & 4 & -2\left(2 + n_b\alpha_o\right) \end{bmatrix}$$

$$\mathbf{A_1} = \begin{bmatrix} 0 & 0 & 0 & 0 \\ 0 & 2n_b\psi & 0 & 2n_b\psi\alpha_o \\ 0 & 0 & 0 & 0 \\ 0 & 2n_b & 0 & -2n_b\alpha_o \end{bmatrix},$$

with $\alpha_o = \upsilon_o/\omega_o$. Since $\mathbf{A_o}$ and $\mathbf{A_1}$ are time-invariant, the linear approximation associated with the system presents exactly the same system of equations, except for the last term on the RHS of Equation (5.1.1), which is related to the contact force and torque at the wear flat. It happens because the friction force is assumed constant around the nominal solution.

A numerical tool based on spectral analysis [63] was used to assess the stability of the equilibrium (zero) solution of Equation (5.1.1) (without the last term); the result is presented in Figure 5.1.2. For comparison purposes, the stability boundaries for a single axial and torsional oscillator are also presented in Figure 5.1.2; the system is stable if the pair (υ_o, ω_o) is inside the region bounded by the solid lines. For comparison purpose, the stability of the RGD model based on time scale separation derived by [52] is presented in the same figure by the dashed curve. The linearized equations of motion in this case reads (see [11]):

$$\frac{\partial^2 u}{\partial \tau^2} + \kappa_d u = -\psi n_b \left[u\left(1,\tau\right) - u\left(1,\tau-\tau_1\right) - \alpha_o\varphi\left(1,\tau\right) + \alpha_o\varphi\left(1,\tau-\tau_1\right)\right], \tag{5.1.2}$$

$$\frac{\partial^2 \varphi}{\partial \tau^2} + \varphi = -n_b \left[u\left(1,\tau\right) - u\left(1,\tau-\tau_1\right) - \alpha_o\varphi\left(1,\tau\right) + \alpha_o\varphi\left(1,\tau-\tau_1\right)\right]. \tag{5.1.3}$$

First, compared to the system represented by a single axial and torsional oscillator, the stable area shrinks for the two coupled oscillators, as already shown for a system of axial oscillators in this thesis and in accordance with the results of [40]. The system studied in [30] was our benchmark case to study the oscillators stability since it contains all necessary data, as the geometry of the drill-pipe section, for instance.

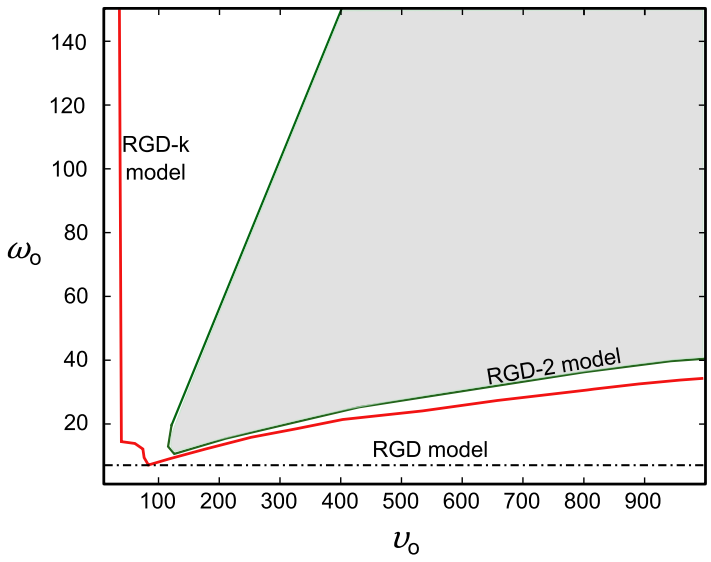

Figure 5.1.2: Stability region in v_o-ω_o space for the two coupled oscillators discrete system. Shaded area inside curves represents stability. The dashed line denoted by RGD model defines the critical angular velocity ω_o^c for $\psi = 13.79$ and $n_b = 4$. The model denoted by RGD-k is the RGD model but with an axial spring, as in [11].

Time domain simulations were carried out based on [52], for the RGD model and two axial and two torsional oscillators, called here the RGD-2 model. The parameters governing the problem are $\psi = 50$, $\mathcal{W}_o = 7$, $\lambda = 5$, $n_b = 6$, $\omega_o = 5$, and two different β values: 0.3 and 1.3. Figure 5.1.3 shows the evolution of the lower oscillator velocity, as well as the evolution of the perturbed displacement of the two oscillators. The velocity history of the lower oscillator is shown in Figure 5.1.3a and is in agreement with the results from [52]. Figure 5.1.3b shows the axial and angular displacement of the two "mixed" oscillators are in phase.

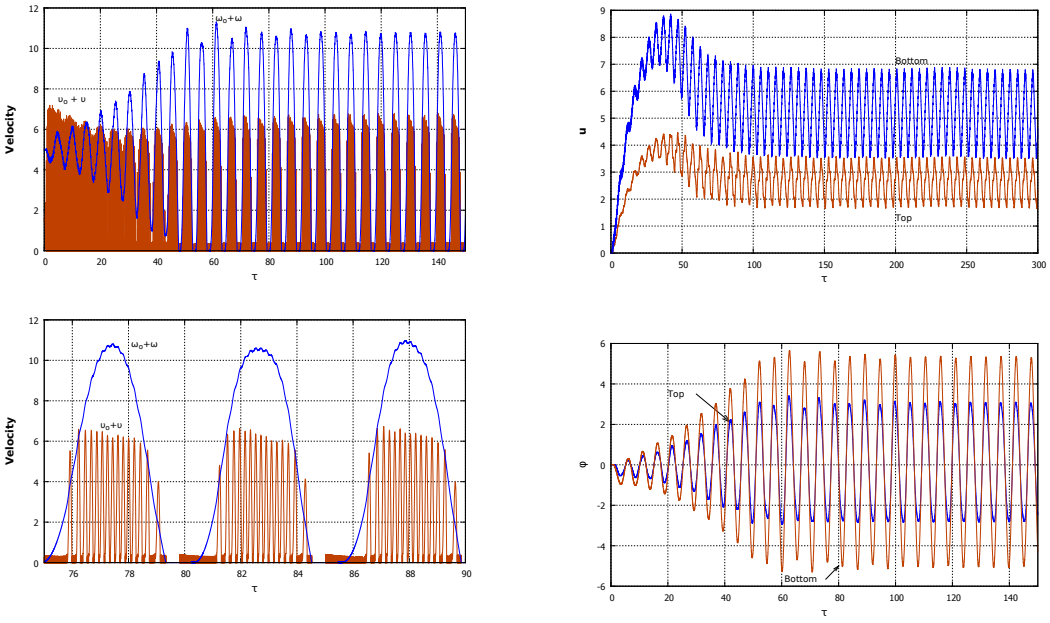

(a) (b)

Figure 5.1.3: Velocity and perturbed displacement evolution for two-oscillator model ($\psi = 50$, $\mathcal{W}_o = 7$, $\lambda = 5$, $n_b = 6$, $\omega_o = 5$, $\beta = 0.3$): (a) bottom mass axial and angular velocities has a similar pattern to RGD model, and (a) the oscillator are in axial (top) and torsional (bottom) phase.

For $\beta = 1.3$, the model still presents a phase locking in torsional mode, and the angular velocity response of the lower oscillator is also close to the RGD model.

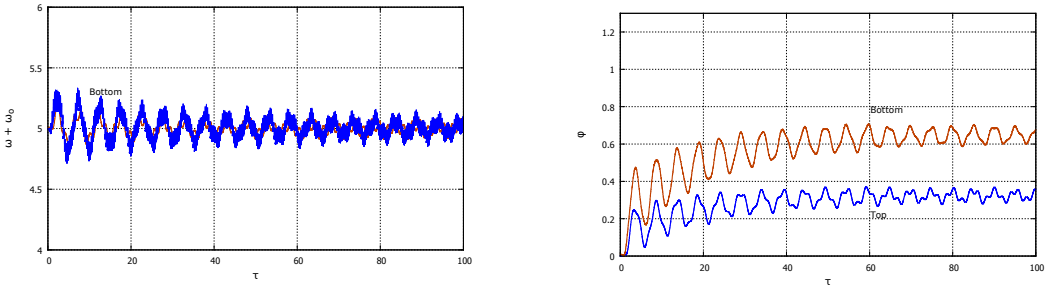

(a) (b)

Figure 5.1.4: Angular velocity and perturbed displacement evolution for 2 model ($\psi = 50$, $\mathcal{W}_o = 7$, $\lambda = 5$, $n_b = 6$, $\omega_o = 5$, $\beta = 1.3$): (a) bottom mass angular velocity has a similar pattern to the RGD model, and (b) the masses are in angular phase.

For comparison purposes, the RGD responses are depicted in Figure 5.1.5, where it is possible to see a good correlation with the response of the two oscillator system. When presenting stick-slip, the axial vibration and stick phase time can be larger in the two oscillator model compared to the RGD model. The change in axial dynamics comes from the kinematic nature of the surface BC considered as well as the introduction of and additional axial stiffness and the compliance representing the top axial oscillator, in addition to the compliance between masses, changes the axial dynamics.

The larger stick phase in the two-oscillators model comes from the fact that the torque build up necessary to make the bit free takes longer compared to the RGD model. Immediately before the stick phase, the lower oscillator can present larger angular position compared to the top one, as depicted in Figure 5.1.6. Hence, the time taken to develop the necessary torque to overcome the bit-rock reacting torque increases.

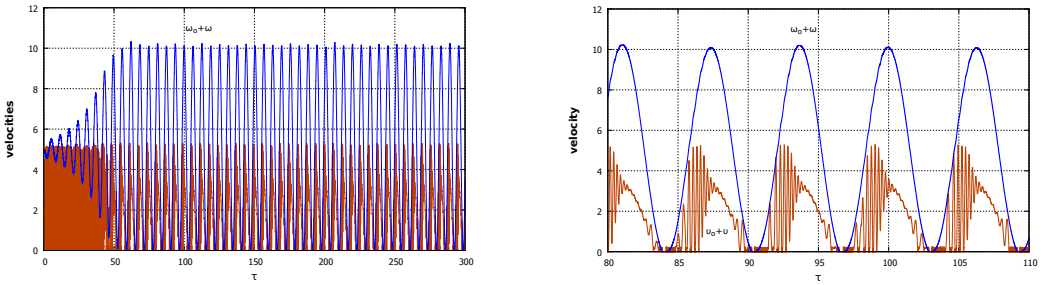

(a)

(b)

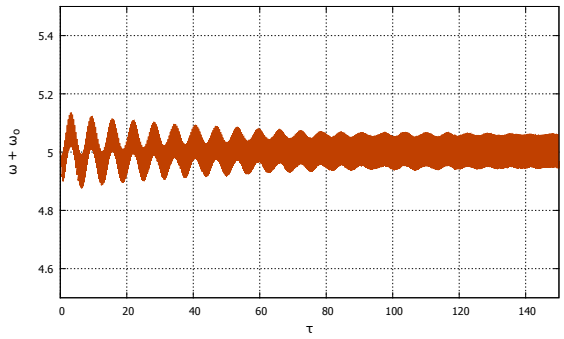

(c)

Figure 5.1.5: RGD model response ($\psi = 50$, $\mathcal{W}_o = 7$, $\lambda = 5$, $n_b = 6$, $\omega_o = 5$) from [52]: (a) axial and angular velocities for $\beta = 0.3$, with (b) detailed velocities behavior, and (c) angular velocity behavior for $\beta = 1.3$.

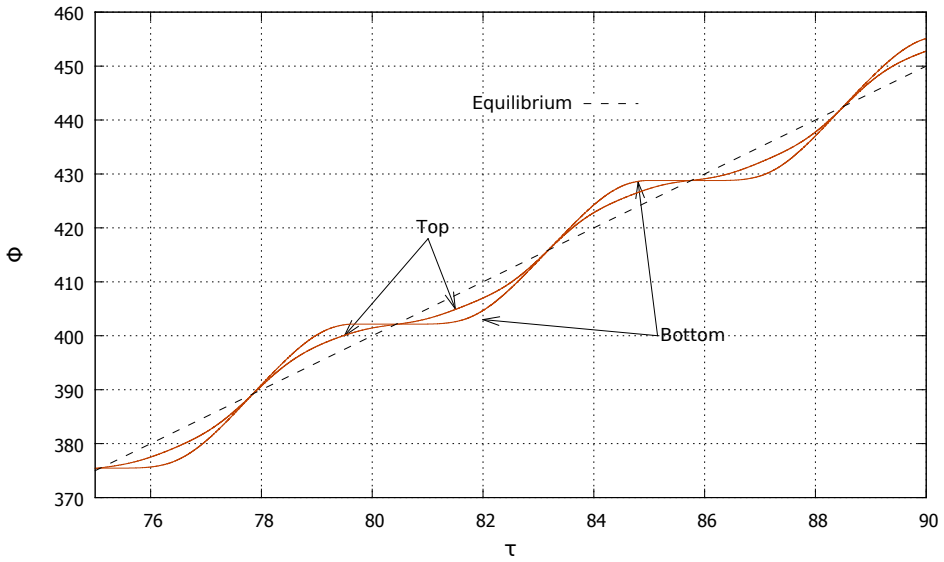

Figure 5.1.6: Total angular evolution Φ for both masses. Before the stick phase, the bottom mass can be ahead of the top mass in terms of angular motion, resulting in longer stick phase.

5.2 Stability Analysis for a Theoretical Semi-Infinite Drill String

If the drill-string is sufficiently long, the system dynamics may evolve before any wave (reflected at the surface) hits the bit. Such a system could thus be seen, in the limiting case, as a semi-infinite drill-string.

Figure 5.2.1 depicts a schematic view of the idealized system. The representation of the semi-infinite drill string is done by the imposition of the radiation BC above the bit, which can be written as a force proportional to the bit velocity. Therefore, we can replace the drill-string by a damper BC, which will not have any reflection back to the bit. No reflection means that there is no torque build up through the drill pipes when the bit sticks. Hence, once the bit sticks it remains stuck. For this reason this model can only be used to assess the system stability of

the nominal operation conditions (constant hook load and angular velocity), in contrast to the FEM and discrete models presented earlier.

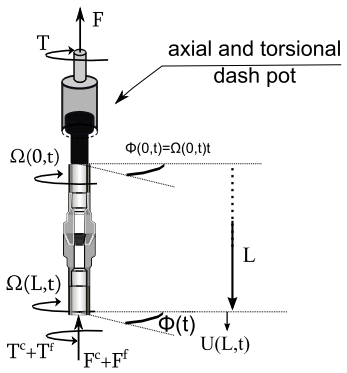

Figure 5.2.1: Idealized model of a semi-infinite drill-string.

The forces acting on the system are the weight and torque on bit (W and T), and the force F and torque T at the drill pipes. At $x = 0$, these forces and torques must be balanced. *i.e.* $W = \int f_u dx - F$ and $T = T^c + T^f$, with f_u being the drill pipes self weight per unit length. For the equilibrium solution U_o and Φ_o, torque and forces are constant, and $W_o = \int f_u dx - F^o$. From the semi-infinite drill string without dispersion, we can relate the force F and torque T perturbation to the bit velocity as follow:

$$\frac{\partial (U - U_o)}{\partial t} = -c_u \frac{\partial (U - U_o)}{\partial x} = -c_u \frac{\delta F}{AE}, \tag{5.2.1}$$

$$\frac{\partial (\Phi - \Phi_o)}{\partial t} = -c_\varphi \frac{\partial (\Phi - \Phi_o)}{\partial x} = -c_\varphi \frac{\delta T}{GJ}. \tag{5.2.2}$$

The terms δF and δT denote perturbations in the weight-on-bit and torque-on-bit generated at the bit/rock interface, i.e.,

$$\delta F = W_o - \left(W^c + W^f\right) \tag{5.2.3}$$

$$\delta T = T_o - \left(T^c + T^f\right). \tag{5.2.4}$$

These perturbations propagated upward in the drillstring while remaining shape-invariant in view of the assumptions of a semi-infinite homogeneous elastic drillstring.

Expressions for WOB and TOB cutting and frictions components were previously presented in Equations (2.2.6), (2.2.7), (2.2.8), and (2.2.9). We can write the dimensionless perturbed linear and angular momentum balances equations. Defining a new dimensionless time $\tau' = t/t_s$, where t_s is the characteristic wave traveling time $t_s = L/c_u$, and substituting (5.2.1), and (5.2.2) into Equations (5.2.3) and (5.2.4), we have:

$$\frac{\partial}{\partial \tau} u\left(1,\tau'\right) = -\psi_u n_b \left[u\left(1,\tau'\right) - u\left(1,\tau' - \tau_1'\right) + \upsilon_o' \hat{\tau}_1' + \lambda g\left(\upsilon'\right)\right], \tag{5.2.5}$$

$$\vartheta_\varphi \frac{\partial}{\partial \tau} \varphi\left(1,\tau'\right) = -\psi_\varphi n_b \left[u\left(1,\tau'\right) - u\left(1,\tau' - \tau_1'\right) + \upsilon_o' \hat{\tau}_1' + \lambda \beta g\left(\upsilon'\right)\right]. \tag{5.2.6}$$

with the dimensionless groups ϑ_φ, ψ_u, and ψ_φ and dimensionless nominal axial velocity υ_o' defined by:

$$\psi_u = \frac{\zeta \varepsilon a d_*}{AE} = \frac{W_*}{AE},\ \upsilon_o' = \frac{V_o t_s}{d_*},\ \omega_o' = \Omega_o \tag{5.2.7}$$

$$\psi_\varphi = \frac{\varepsilon a^2 d_*^2}{2GJ},\ \vartheta_\varphi = \frac{c_u}{c_\theta}. \tag{5.2.8}$$

The linear stability analysis is performed based on [35], in which the system of delayed differential equations $\dot{\mathbf{x}} = \mathbf{g}\left(\mathbf{x}\left(\tau\right), \mathbf{x}\left(\tau - \tau_1\right), \tau\left(\mathbf{x}\right)\right)$ has the linear approximation around the equilibrium point $\mathbf{x} = \bar{\mathbf{x}}$ given by:

$$\begin{aligned} \delta\dot{\mathbf{x}} \quad = \quad & D_1\mathbf{g}\left(\bar{\mathbf{x}}\left(\tau'\right), \bar{\mathbf{x}}\left(\tau' - \tau_1'\right), \tau_1\left(\bar{\mathbf{x}}_{\tau'}\right)\right)\mathbf{y}\left(\tau'\right) + D_2\mathbf{g}\left(\bar{\mathbf{x}}\left(\tau'\right), \bar{\mathbf{x}}\left(\tau' - \tau_1'\right), \tau_1'\left(\bar{\mathbf{x}}_{\tau'}\right)\right)\mathbf{y}\left(\tau' - \tau_1'\right) \\ & + D_3\mathbf{g}\left(\bar{\mathbf{x}}\left(\tau'\right), \bar{\mathbf{x}}\left(\tau' - \tau_1'\right), \tau_1'\left(\bar{\mathbf{x}}_{\tau'}\right)\right) D\tau_1'\left(\bar{\mathbf{x}}_{\tau'}\right)\mathbf{y}\left(\tau'\right), \end{aligned}$$

where $D_j\mathbf{g}$ denotes the derivative of $\mathbf{g}$ with respect to the j-th argument of $\mathbf{g}$, and $D\tau_1'$ denotes the Fréchet derivative [1] of the time delay with respect to $\bar{\mathbf{x}}_{\tau'}$, and $\mathbf{y}$ representing the perturbation around the equilibrium solution. Using Equation (2.4.14) to replace $\hat{\tau}_1' = \left[-\varphi\left(1,\tau'\right) + \varphi\left(1,\tau' - \tau_1'\right)\right]/\omega_o'$, with $\omega_o' = \Omega_o t_s$, all DDE's have constant coefficients and no time delay explicitly involved. Therefore $D_1\mathbf{g}$ and $D_2\mathbf{g}$ are constant, and $D\tau' = 0$.

Let u and φ denote perturbations around the equilibrium point; the linear system of equations governing the evolution of these perturbations reads:

[1] The Fréchet derivative is commonly used to generalize the derivative of a real-valued function of a single real variable to the case of a vector-valued function. Similarly to the derivative of real-valued functions, Fréchet differential of τ_1 can be understood as the best local linear approximation of $\tau_1\left(\bar{\mathbf{x}}_\tau\right)$ [38].

$$\frac{\partial}{\partial\tau}u\left(1,\tau'\right)=-\psi_u n_b\left[u\left(1,\tau'\right)-u\left(1,\tau'-\tau'_{1,0}\right)+\alpha_1\varphi\left(1,\tau'-\tau'_{1,0}\right)-\alpha_1\varphi\left(1,\tau'\right)\right], \quad (5.2.9)$$

$$\vartheta_\varphi\frac{\partial}{\partial\tau}\varphi\left(1,\tau'\right)=-\psi_\varphi n_b\left[u\left(1,\tau'\right)-u\left(1,\tau'-\tau'_{1,0}\right)+\alpha_1\varphi\left(1,\tau'-\tau'_{1,0}\right)-\alpha_1\varphi\left(1,\tau'\right)\right], \quad (5.2.10)$$

with $\alpha_1=\upsilon'_o/\omega'_o$, and $\tau'_{1,0}$ representing the nominal constant time delay.

Numerical techniques for the computation of the eigenvalues of DDE's was used [63] to assess the stability of the above system. The study in the parameter space υ_o-ω_o $(\nu'_o-\omega'_o)$ shows that increasing angular velocity (or decreasing time delay) enhances system stability, as shown in Figure 5.2.2.

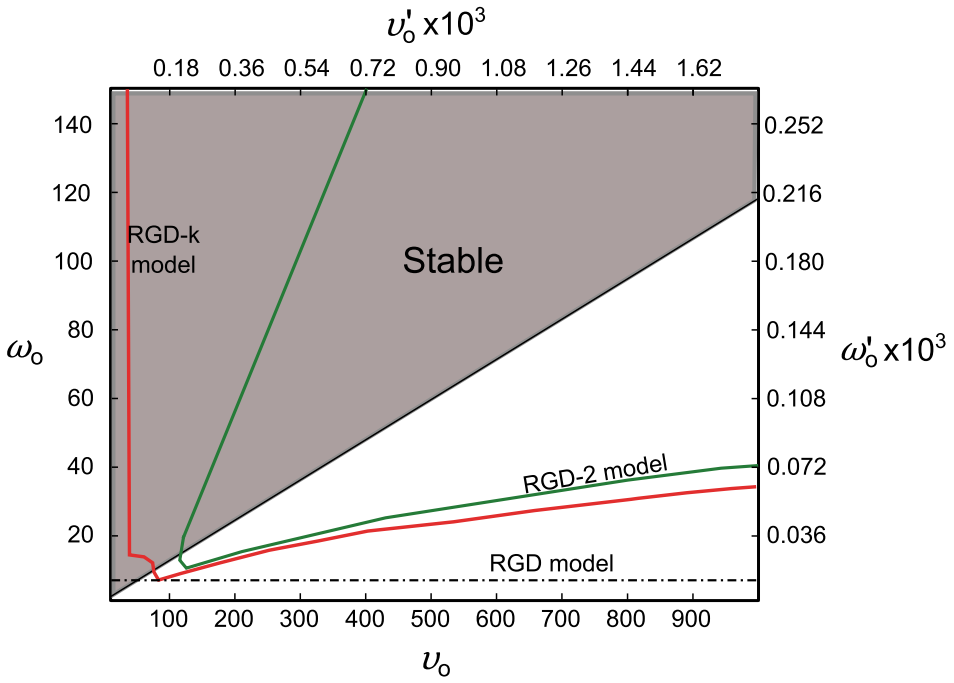

Figure 5.2.2: Limit case stability chart in ν_o-ω_o $(\nu'_o-\omega'_o)$ space parameter for $n_b=4$, $\psi_u=5.32\times10^{-5}$, and $\psi_\varphi=2.64\times10^{-3}$ Stable region is highlighted by the shaded area, and the critical angular velocity from RGD model, and stability boundaries of RGD-k, and RGD-2 model cases are presented as reference.

5.3 Discussion

The stability of the linearized system representing the original drilling system modeled as two identical axial-torsional oscillators was assessed by means of stability analysis and numerical simulation. The analysis shows that the 2-oscillator representation (RGD-2) has a reduced stability region area in the parametric space of the dimensionless velocities, compared to the original RGD model Time simulations showed that the overall dynamic response of the 2-oscillator representations agrees with the 1-oscillator representation, with a larger stick phase in 2-mass model due to the difference between angular positions of the top and bottom masses. The 2-mass model presented a phase-lock pattern between masses in both axial and torsional motion.

The theoretical semi-infinite model (with no mass) did not bring any additional stability, but changed the stable region in the parametric space.

Chapter 6

Conclusions

6.1 Contributions of the thesis

6.1.1 Finite element model formulation

A recent publication [41] suggests that increasing the number of elements/nodes in the spatial discretization of the dynamical model of a drill string decreases the stability region of the discrete system. Based on these results, it seemed likely that the finite element model used by Germay *et. al.* [30] would always be unstable, independent of the imposed parameters, drill-bit design, or drilling system geometries. This results imposes an additional difficulty to understand and find an effective way to mitigate stick-slip, and the follow question arose: how it is possible to mitigate stick-slip in a drilling system which is likely to be always unstable? The consideration of the drive system with angular velocity control, the Soft-Torque, could be the answer. Time-domain numerical simulation of the developed finite element model including bit/rock interaction were performed to compare the standard and ST drive system for a benchmark case.

Both time domain simulations (standard and ST drive systems) exhibited the same pattern, with fast development of axial oscillations compared to the angular velocity oscillations. The bit presented axial and angular stick with the standard drive system. However, the ST only delayed the angular speed oscillations growth, not mitigating it, and finished with backward rotation. This study shows that Soft Torque can not stabilize this model, which is due to the fact that i)

Soft Torque only damps the first torsional resonance mode, and ii) higher flexibility modes play a dominant role in the dynamics. Motivated by these observations, we subsequently studied discretized models aiming to understand the key dynamics responsible for such instability and stick-slip oscillations.

6.1.2 Spatial discretization problem

The role of the model spatial discretization is the most important outcome of this thesis, and must be further investigated. It is not clear if the pronounced instability is an inherent property of the continuous system or if it is just related to the discrete representation itself. If it is a system inherent property, system changes must be done to provide stability. Otherwise, the reasons behind the discrete representation instability must be understood, and proper representation should be proposed.

According to numerical results from the eigenvalues evolution study for axial 2-DOF model, the masses can approximately be in-phase or 180^oout-of-phase, which suggests an interesting pattern result. The time simulations results agreed with such results, and the two oscillators were either in- or out-of-phase for the considered cases. The same also occurred for the axial models with 3 DOF and 10 DOF. But now, the in- or out-of-phase happened between groups or clusters, at the top and bottom of the system. When comparing the out-of-phase response from these latter two cases, there is an oscillator located at an intermediate position with minimum displacement compared to the others, establishing the phase inversion location. Basically, all three models time responses presented a good correlation among themselves.

In Chapter 5, we studied the effect of the coupling between axial and torsional modes. The stability area reduced when comparing the 2 oscillators model to the single one. It is in accordance to the observations made for the axial models, and also to the results presented in [41]. But it seems that coupled motion resulted in a smaller reduction of the stability area compared to that observed for the models describing the axial dynamics only. Time domain simulation revealed that the responses are in good agreement between themselves.

6.2 Suggestions for future work

Certain assumptions and limitations are associated with the present study, which should be addressed in future work. But the main research should be addressed to answer the following:

- Evaluate stability analysis for continuous models, for both axial and coupled dynamics;
- Understand the discretization importance to assess the drilling system stability

Also a better representation of the boundary conditions can also be addressed, as:

- Actual drill bits are not characterized by a continuous cutter surface distributed over identical blades with an even angular distribution. The cutters distribution over the blades is in fact quite complex, resulting in non-homogeneous depth-of-cuts. This depth-of-cut variation comes from the alignment among the cutters, which results in multiple delays per one particular bit design;
- The contact stress acting underneath the cutter shall be changed for the most representative case developed by Zhou and Detournay [64];
- The bit-rock interface law describes well the average cutting behavior under quasi-static conditions. This behavior may represent well the interface law for low frequency waves hitting the drill bit. But for high frequencies, there is no clear evidence of what happens;
- A proper controller for the Soft-Torque should be included. Or, in the other way around, if the continuous system is always unstable, the controller can be designed to bring proper system stability;
- Imposed axial velocity is assumed as surface BC. But the actual system is a composed of a dead load suspended by cables what introduces a non-linear BC;

Bibliography

[1] Presentation electroproject - EPST. www.softorque.com.

[2] Tesco 750 esi top drive. Technical report.

[3] ElectroProject Aandrijftechniek. EPST - Electroproject Soft Torque System information. Technical report, 1033 RH Amsterdan, August 2010.

[4] Y. Altintas. *Manufacturing Automation - Metal Cutting Mechanics, Machine tool vibrations, and CNC design.* Cambridge University Press, 2000.

[5] Y. Altintas. *Manufacturing Automation - Metal Cutting Mechanics, Machine tool vibrations, and CNC design.* Cambridge University Press, Englewood Cliffs, N.J., 2000.

[6] ASCE-IABSE. *A method of computation for structural dynamics.* J. of Eng Mech Division, October 1958.

[7] R. Baker. *A primer of oilwell drilling: a basic text of oil and gas drilling.* 6th Edition. Petroleum Extension Service, Austin, TX, 2001.

[8] K. J. Bathe and G. Noh. Insight into an implict time integration scheme for structural dynamics. *Computer and Structures*, pages 1–6, 2012.

[9] A. Bellen and M. Zennaro. *Numerical Methods for Delay Differential Equations.* Numerical Mathematics and Scientific Computation. Oxford Science Publications, 2003.

[10] R. Bellman and K. L. Cooke. *Diferential-Difference Equations.* Academic Press, New York, 1963.

[11] B. Besselink, N. van de Wouw, and H. Nijmeijer. A semi-analytical study of stick-slip oscillations in drillling systems. *Journal of Computational and Nonlinear Dynamics*, 6:02100–1, 2011.

[12] S. J. Bhatt and C. S. Hsu. Stability criteria for second-order dynamical systems with time lag. *ASME Journal of Applied Mechanics*, 33(1):113–118, 1966.

[13] A.T. Bourgoyne Jr., K.K. Millheim, M.E. Chevernet, and F.S. Young Jr. *Applied Drilling Engineering*. SPE Textbook series. Society of Petroleum Engineers, Richardson, TX, 1991.

[14] J. Brehme and J.T.Travis Jr. Total BHA reliability - an improved method to measure success. *IADC/SPE*, March 2008.

[15] J.F. Brett. The genesis of torsional drillstring vibrations. 7(21943-PA):168–174, 1992.

[16] R.M. Corless and N. Fillion. *A Graduate Introduction to Numerical Methods: From the Viewpoint of Backward Error Analysis*. Springer, 2013.

[17] D. Dareing, J. Tlusty , and C. Zamudio. Self-excited vibrations induced by drag-bits. *Transactions of ASME*, 112:54–61, March 1990.

[18] A. Depouhon, V. Denoël, and E. Detournay. A drifting impact oscillator with periodic impulsive loading: Application to percussive drilling. *Physica D*, 258:1–10, 2013.

[19] A. Depouhon and E. Detournay. Apparent coexistence of multiple regimes of self-excited vibrations in drilling systems. In V. Denoël and E. Detournay, editors, *First International Colloquium on Non-Linear Dynamics of Deep Drilling Systems*, pages 59–63, Liege, Belgium, March 2009.

[20] A. Depouhon and E. Detournay. Instability regimes and self-excited vibrations in deep drilling systems. *Journal of Sound and Vibration*, April 2013.

[21] A. Depouhon and E. Detournay. Instability regimes and self-excited vibrations in deep drilling systems. *Journal of Sound and Vibration*, 333(7):2019–2039, July 2014.

[22] E. Detournay and P. Defourny. A phenomenological model for the drilling action of drag bits. *International Journal of Rock Mechanics and Mining Sciences and Geomechanics Abstracts*, 29(1):13–23, 1992.

[23] L.E. Dickson. *First course in theory of equations.* Braunworth & Co. Inc, 2009.

[24] S. Divenyi, M. A. Wiercigroch, and E. Pavlovskaia. Drill-string vibration analysis using non-smooth dynamics approach. *Nonlinear Dynamics*, 70:1017–1030, 2012.

[25] F.E. Dupriest and W.L. Koederitz. Maximizing real drill rates with real time surveillance of mechanical specific energy. *SPE/IADC Drilling Conference*, 2005.

[26] T. Erneux. *Applied Delay Differential Equations*, volume 3 of *Surveys and Tutorials in the applied mathematical sciences.* Springer, 2009.

[27] L.F.P Franca. Drilling action of roller-cone bits: modeling and experimental validation. *Journal of Energy Resources Technology*, 132, 2010.

[28] C. Gatlin. *Petroleum Egineering - drilling and well completion.* Prentice Hall Inc., Englewood Cliffs, N.J., 1960.

[29] C. Germay, V. Denoël, and E. Detournay. Self-excited vibrations of a drilling system with drag bits, 2006. Submitted in September 2006.

[30] C. Germay, V. Denoël, and E. Detournay. Multiple mode analysis of the self-excited vibrations of rotary drilling systems. *Journal of Sound and Vibration*, 325:362–381, 2009.

[31] C. Germay, N. van de Wouw, H. Nijmeijer, and R. Sepulchre. Nonlinear drillstring dynamics analysis. *SIAM Journal On Applied Dynamical Systems*, 8:527–553, 2009.

[32] C. Germay, N van de Wouw, R. Sepulchre, and H. Nijmeijer. Axial stick-slip limit cycling in drill-string dynamics with delay. In *Proceedings of the 5th EUROMECH Nonlinear Oscillations Conference (ENOC)*, pages 1136–1143, Eindhoven, Netherlands, 2005.

[33] C. S. Hsu and S. J. Bhatt. Stability charts for second-order dynamical systems with time lag. *ASME Journal of Applied Mechanics*, 33(1):119–124, 1966.

[34] T. Insperger and G. Stépán. *Semi-discretization for time-delay sistems: Stability and Engineering Applications.* Springer, 2011.

[35] T. Insperger, G. Stepan, and J. Turi. State-dependent delay model for regenerative cutting processes. In *Proceedings of Fifth EUROMECH Nonlinear Dynamics Conference, ENOC 2005*, pages 1124–1129, Eindhoven, Netherlands, August 2005.

[36] T. Insperger, G. Stepan, and J. Turi. State-dependent delay in regenerative turning processes. *Nonlinear Dynamics*, 47:275–283, 2007.

[37] J. D. Jansen and L. van den Steen. Active damping of self-excited torsional vibrations in oil-well drillstrings. *Journal of Sound and Vibration*, 179(4):647–668, 1995.

[38] Debnath L. and P. Mikusinski. *An Introduction to Hilbert Spaces with applications.* Elsevier Academic Press, 3rd edition, January 2005.

[39] C.J. Langeveld. Pdc bit dynamics (suplement to iadc/spe 23867). In SPE/IADC, editor, *IADC/SPE Drilling Conference*, number SPE 23873, 1992.

[40] X. Liu, N. Vlajic, X. Long, G. Meng, and B. Balachandran. State-dependent delay influeced drill string dynamics and stability analysis. In *International Design Engineering Technical Conferences and Computers and Information in Engineering Conference*, Portland, USA, 2013.

[41] X. Liu, N. Vlajic, X. Long, G. Meng, and B. Balachandran. Multiple regenerative effects in cutting process and nonlinear oscillations. *International Journal of Dynamic Control*, pages 160–168, 2014.

[42] K. Nandakumar and M. Wiercigroch. Stability analysis of a state dependent delayed, coupled two DOF model of drill-string vibration. *Journal of Sound and Vibration*, 332:2575–2592, 2013.

[43] F. Ng. Recommendations for MWD toll reliability statistics. *SPE*, October 1989.

[44] Zienkiewicz O.C., R.L.Taylor, and J.Z.Zhu. *The Finite Element Method: Its Basis and Fundamentals.* Elsevier, 7 edition, September 2013.

[45] L.S. Pontryagin. On the zeros of some eleelement transcendental functions,. *American Mathematical society translations*, 1(2):95–110, 1955.

[46] H. Reckmann, P. Jogi, F. Kpetehoto, S. Chandrasekaran, and J. Mcpherson. MWD failure rates due to drilling dynamics. *IADC/SPE*, February 2010.

[47] J.N. Reddy. *An Introduction to the Finite Element Method*. McGraw-Hill Book Co, 1st edition edition, 1984.

[48] T. Richard. *Self-Excited Stick-Slip Oscillations of Drag Bits*. Ph. D. Thesis, Faculty of the Graduate School of the University of Minnesota, Minneapolis, Minnesota, U.S.A., December 2001.

[49] T. Richard and E. Detournay. Stick-slip vibrations of PDC bits. In J. Girard, M. Liebman, C. Breeds, and T. Doe, editors, *Pacific Rocks 2000: Rock Around the Rim*, pages 33–40. Balkema, 2000.

[50] T. Richard, E. Detournay, B. Miller, M. Fear, R. Clayton, and O. Matthews. Influence of bit-rock interaction on stick-slip vibrations of PDC bits. In *SPE Annual Technical Conference and Exhibition*, number SPE 77616, pages 1–12, San Antonio, Texas, U.S.A., September-October 2002. Society of Petroleum Engineers.

[51] T. Richard, C. Germay, and E. Detournay. Self-excited stick-slip oscillations of drill bits. *Comptes Rendus Mecanique*, 332(8):619–626, 2004.

[52] T. Richard, C. Germay, and E. Detournay. A simplified model to explore the root cause of stick-slip vibrations in drilling systems with drag bits. *Journal of Sound and Vibration*, 305(3):432–456, 2007.

[53] H.G. Schuster and P. Wagner. Mutual entrainment of two limit cycle oscillatiors with time delay coupling. *Progress of Theoretical Physics*, 81(5):939–945, September 1989.

[54] L.F. Shampine. Solving {ODEs} and {DDEs} with residual control. *Applied Numerical Mathematics*, 52(1):113 – 127, 2005.

[55] G. Stépán. *Retarded dynamical systems: stability and characteristic functions.* Longman, 1989.

[56] D.A. Stephenson and J. S. Agapiou. *Metal cutting theory and practice.* 2nd Edition. CRC Press, 2006.

[57] S. H. Strogatz. From kuramoto model to crawford: exploring the onset of synchronization in populations of coupled oscillators. *Physica D.*, 143:1–20, 2000.

[58] S.A. Tobias. Vibration of machine tools. In *Cranfield Conf. Paper*, volume 43 (12), pages 599–608. Cranfield Conference Paper, 1964.

[59] R.W. Tucker and C. Wang. An integrated model for drill-string dynamics. *Journal of Sound and Vibration*, 224(1):123–165, 1999.

[60] T.G.M. Vromen, N. van de Wouw, A. Doris, P. Astrid, and H. Nijmeijer. Output-feedback control to eliminate torsional drill string vibration. In *53rd IEEE Conference on Decision and Control, LA, CA, U.S.A,*, 2014.

[61] P. Wand, M. Bible, and I. Silvester. Risk-based reliability engineering enables improved rotary-steerable-system performance and defines new industry performance metrics. *IADC/SPE*, February 2006.

[62] S.F. Wolf, M. Zacksenhoue, and A. Arian. Field measurements of downhole drillstring vibrations. *IADC/SPE*, September 1985.

[63] Z. Wu and W. Michiels. Reliably computing all characteristic roots of delay diferential-difference equations in a given right half plane using a spectral method. Technical report, Department of Computer Science, K.U. Leuven, October 2011.

[64] Y. Zhou and E. Detournay. Analysis of the contact forces on a blunt PDC bit. 2014.

[65] O.C. Zienkiewicz, R.L. Taylor, and P. Nithiarasu. *The Finite Element Method for Fluid Dynamics.* Butterworth-Heinemann, Oxford, seventh edition edition, 2014.

Appendix A

Appendices

A.1 Finite element formulation for wave equation

In this appendix we show briefly the finite element formulation (see [47, 65]) for drill string dynamics defined by Equations (2.4.8) and (2.4.9). First we rewrite Equations (2.4.8) and (2.4.9) in their original perturbed form. Equations (2.4.8) and (2.4.9) in perturbed coordinates reads:

$$\rho A\frac{\partial^2 u}{\partial t^2}+A\varsigma_u\frac{\partial u}{\partial t}-E\frac{\partial}{\partial x}\left[A\left(x\right)\frac{\partial u}{\partial x}\right]=0 \tag{A.1.1}$$

$$\rho J\frac{\partial^2 \varphi}{\partial t^2}+J\varsigma_\phi\frac{\partial \varphi}{\partial t}-G\frac{\partial}{\partial x}\left[J\left(x\right)\frac{\partial \varphi}{\partial x}\right]=0 \tag{A.1.2}$$

Pipe cross section geometry is piece-wise constant with $A\left(x\right)=A_p$, $J\left(x\right)=J_p$ for $0\leq x\leq L_p$, and $A\left(x\right)=A_B$, $J\left(x\right)=J_B$ for $L_p\leq x\leq L$. We can integrate the above equations over length L as follow:

$$\int_0^{Lp}\left(\rho A_p\frac{\partial^2 u}{\partial t^2}+A_p\varsigma_u\frac{\partial u}{\partial t}-EA_p\frac{\partial^2 u}{\partial x^2}\right)dx+\int_{Lp}^{L}\left(\rho A_B\frac{\partial^2 u}{\partial t^2}+A_b\varsigma_u\frac{\partial u}{\partial t}-EA_B\frac{\partial^2 u}{\partial x^2}\right)dx=0 \tag{A.1.3}$$

$$\int_0^{Lp}\left(\rho J_p\frac{\partial^2\varphi}{\partial t^2}+J_p\varsigma_\phi\frac{\partial\varphi}{\partial t}-GJ_p\frac{\partial^2\varphi}{\partial x^2}\right)dx+\int_{Lp}^{L}\left(\rho J_B\frac{\partial^2\varphi}{\partial t^2}+J_B\varsigma_\phi\frac{\partial\varphi}{\partial t}-GJ_p\frac{\partial^2\varphi}{\partial x^2}\right)dx=0 \tag{A.1.4}$$

We can rewrite above equations in dimensionless form as:

$$\int_0^{\xi p}\left(\mathcal{G}_u\frac{\partial^2 u}{\partial\tau^2}+\chi_u\frac{\partial u}{\partial\tau}-\frac{\partial^2 u}{\partial\xi^2}\right)d\xi+\frac{A_B}{A_p}\int_{\xi p}^{1}\left(\mathcal{G}_u\frac{\partial^2 u}{\partial\tau^2}+\chi_u\frac{\partial u}{\partial\tau}-\frac{\partial^2 u}{\partial\xi^2}\right)d\xi=0 \tag{A.1.5}$$

$$\int_0^{\xi p}\left(\mathcal{G}_\varphi\frac{\partial^2\varphi}{\partial\tau^2}+\chi_\varphi\frac{\partial\varphi}{\partial t}-\frac{\partial^2\varphi}{\partial x^2}\right)d\xi+\frac{J_B}{J_p}\int_{\xi p}^{1}\left(\mathcal{G}_\phi\frac{\partial^2\varphi}{\partial\tau^2}+\chi_\varphi\frac{\partial\varphi}{\partial t}-\frac{\partial^2\varphi}{\partial x^2}\right)d\xi=0 \tag{A.1.6}$$

The dimensionless parameters $\mathcal{G}_u=\rho L^2/Et_*^2$ and $\mathcal{G}_\varphi=\rho L^2/Gt_*^2$, coordinate system $\xi=x/L$, and time $\tau=t/t_*$ where previously presented by [30]. Dimensionless damping parameters are $\chi_u=\varsigma_u L^2/t_*E$ and $\chi_\varphi=\varsigma_\phi L^2/t_*G$. Since the first and second integrands are the same, we can derive a general finite element formulation and take into account the geometry multiplier factor ($\frac{A_B}{A_p}$ and $\frac{J_B}{J_p}$) for the equations representing the i-th nodes ($i=n_p,...,n$) located at $\xi_i\in[\xi_p,1]$. Multiplying Equations (A.1.5) and (A.1.6) by an arbitrary function ψ and integrating by parts the latter integrand term we obtain:

$$\mathcal{G}_u\int_{\mathscr{D}}\frac{\partial^2 u}{\partial\tau^2}\psi d\xi+\chi_u\int_{\mathscr{D}}\frac{\partial u}{\partial\tau}\psi d\xi+\int_{\mathscr{D}}\frac{\partial u}{\partial\xi}\frac{\partial\psi}{\partial\xi}d\xi-\left[\frac{\partial u}{\partial\xi}\psi\right]_{\xi_i}^{\xi_{i+1}}=0 \tag{A.1.7}$$

$$\mathcal{G}_\varphi\int_{\mathscr{D}}\frac{\partial^2\varphi}{\partial\tau^2}\psi d\xi+\chi_\varphi\int_{\mathscr{D}}\frac{\partial\varphi}{\partial\tau}\psi d\xi+\int_{\mathscr{D}}\frac{\partial\varphi}{\partial\xi}\frac{\partial\psi}{\partial\xi}d\xi-\left[\frac{\partial\varphi}{\partial\xi}\psi\right]_{\xi_i}^{\xi_{i+1}}=0 \tag{A.1.8}$$

For notation simplicity, let us assume that the functions u and φ are the approximation of the real solution defined by $u\approx\sum_{i=1}^{n}u_i\psi_i$ and $\varphi\approx\sum_{i=1}^{n}\varphi_i\psi_i$, where $\psi(\xi)$ is called the interpolation (or weight) function. Figure A.1.1 shows two interpolation functions (ψ) examples. The values u_i and φ_i represent the actual nodal values for the approximation at the nodes located at ξ_i ($0\leq\xi_i\leq1$), with $i=1,2,..,n$ and n representing the total number of nodes in the semi-discrete formulation.

$$\sum_{i=1}^{n}\left[\mathcal{G}_u\int_{\mathscr{D}}\frac{\partial^2 u_i}{\partial\tau^2}\psi_i\psi_j d\xi+\chi_u\int_{\mathscr{D}}\frac{\partial u_i}{\partial\tau}\psi_i\psi_j d\xi+\right.$$
$$\left.+\int_{\mathscr{D}}u_i\frac{\partial\psi}{\partial\tau}\frac{\partial\psi_j}{\partial\xi}d\xi-P_{i+1}\psi_j\left(\xi_{i+1}\right)-P_i\psi_j\left(\xi_i\right)\right]=0 \tag{A.1.9}$$

$$\sum_{i=1}^{n}\left[\mathcal{G}_\varphi\int_{\mathscr{D}}\frac{\partial^2\varphi_i}{\partial\tau^2}\psi_i\psi_j d\xi+\chi_\varphi\int_{\mathscr{D}}\frac{\partial\varphi_i}{\partial\tau}\psi_i\psi_j d\xi+\right.$$
$$\left.+\int_{\mathscr{D}}\varphi_i\frac{\partial\psi_i}{\partial\tau}\frac{\partial\psi_j}{\partial\xi}d\xi-Q_{i+1}\psi_j\left(\xi_{i+1}\right)-Q_i\psi_j\left(\xi_i\right)\right]=0 \tag{A.1.10}$$

The terms $P_i=\left.\frac{\partial u_i}{\partial\xi}\right|_{\xi_i}$ and $Q_i=\left.\frac{\partial\varphi_i}{\partial\xi}\right|_{\xi_i}$ are internal force and torque at i-th node respectively.

Integrals defined in Equations (A.1.9) and (A.1.10) are nonzero only in $\mathscr{D}\in[\xi_i,\xi_{i+1}]$, which allow us to rewrite the equations above per element. For the i-th element, Equations (A.1.9) and (A.1.10) are written in matricial form as follow:

$$\mathcal{G}_u\mathbf{M}^{(e)}\ddot{\mathbf{u}}^{(e)}+\chi_u\mathbf{D}^{(e)}\dot{\mathbf{u}}^{(e)}+\mathbf{K}^{(e)}\mathbf{u}^{(e)}=\mathbf{F}^{(e)} \tag{A.1.11}$$

$$\mathcal{G}_\varphi\mathbf{J}^{(e)}\ddot{\mathbf{\Phi}}^{(e)}+\chi_\varphi\mathbf{E}^{(e)}\dot{\Phi}^{(e)}+\mathbf{C}^{(e)}\Phi^{(e)}=\mathbf{T}^{(e)} \tag{A.1.12}$$

with $\mathbf{u}^{(e)}=\{u_i,u_{i+1}\}^T$ and $\mathbf{\Phi}^{(e)}=\{\varphi_i,\varphi_{i+1}\}^T$ being the nodal displacements at nodes i and $i+1$. The element matrices representing the mass and inertia $\mathbf{M}$ and $\mathbf{J}$, axial and torsional damping and stiffness $\mathbf{D}$, $\mathbf{E}$, $\mathbf{K}$, and $\mathbf{C}$ can be written as:

$$\mathbf{M}^{(e)}=\mathbf{D}^{(e)}=\sum_{i=1}^{n}\int_{\xi_i}^{\xi_{i+1}}\psi_i\psi_j d\xi,\ \mathbf{J}^{(e)}=\mathbf{E}^{(e)}=\sum_{i=1}^{N}\int_{\xi_i}^{\xi_{i+1}}\psi_i\psi_j d\xi$$

$$\mathbf{K}^{(e)}=\sum_{i=1}^{n}\int_{\xi_i}^{\xi_{i+1}}\frac{\partial\psi_i}{\partial\xi}\frac{\partial\psi_j}{\partial\xi}d\xi,\ \mathbf{C}^{(e)}=\sum_{i=1}^{N}\int_{\xi_i}^{\xi_{i+1}}\frac{\partial\psi_i}{\partial\xi}\frac{\partial\psi_j}{\partial\xi}d\xi$$

The vectors $\mathbf{F}^{(e)}=\{F_i,F_{i+1}\}^T$ and $\mathbf{T}^{(e)}=\{T_i,T_{i+1}\}^T$ can encompass the external applied loads (force f or torque f_φ) and natural boundary conditions and internal forces at the nodal points ξ_i and ξ_{i+1} and are defined by:

$$\mathbf{F}^{(e)}=\int_{\xi_i}^{\xi_{i+1}}f\psi_j d\xi+P_{i+1}\psi_j\left(\xi_{i+1}\right)+P_i\psi_j\left(\xi_i\right) \tag{A.1.13}$$

and

$$\mathbf{T}^{(e)}=\int_{\xi_i}^{\xi_{i+1}}f_\varphi\psi_j d\xi+Q_{i+1}\psi_j\left(\xi_{i+1}\right)+Q_i\psi_j\left(\xi_i\right) \tag{A.1.14}$$

For the i-th element ($i = n_p, ..., n-1$) formed by nodes located at $\xi_i \in [\xi_p, 1]$ mass (inertia), damping, stiffens matrices and forces (torques) shall be multiplied by $\frac{A_B}{A_p}$ or $\frac{J_B}{J_p}$ to keep Equations (A.1.1) and (A.1.2) valid for $0 < \xi < 1$.

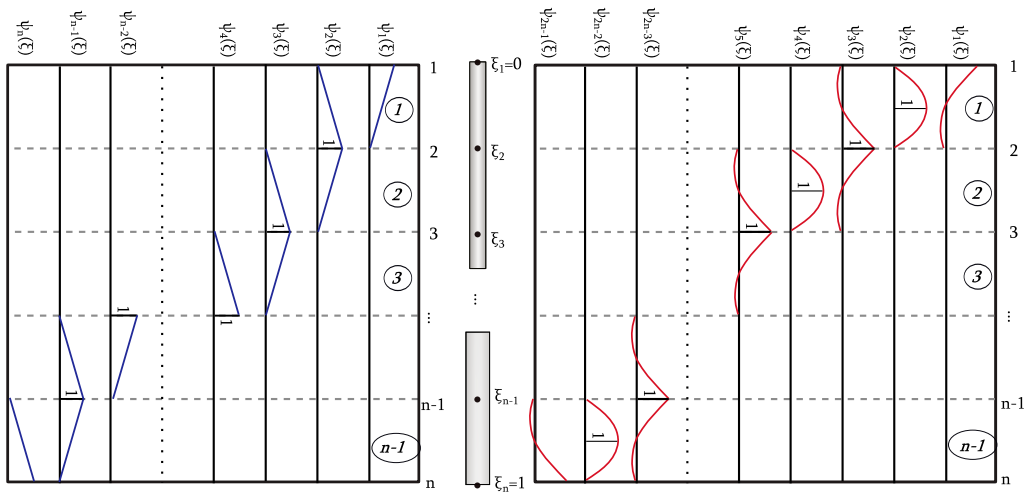

Figure A.1.1: Interpolation functions showing the linear (left) and second order (right) approximations. The elements numbers are presented inside the circles

The choice of basis functions $\psi_i(\xi)$ shall meet the natural boundary conditions requirements and is a function of the problem we want to solve. In our particular case, where we are looking for displacements, the linear basis functions (left in Figure A.1.1) are a good option (noting that the forces and torques present discontinuities at nodes). The approximation linear functions over one element of length $\triangle\xi_i = \xi_{i+1} - \xi_i$ are:

$$\begin{cases} \psi_1(\xi) := \frac{\xi_{i+1} - \xi}{\xi_{i+1} - \xi_i}, & \\ \psi_2(\xi) := \frac{\xi - \xi_i}{\xi_{i+1} - \xi_i}, & \xi \in [\xi_i, \xi_{i+1}] \\ \psi_1(\xi) = \psi_2(\xi) = 0, & \xi \notin [\xi_i, \xi_{i+1}] \end{cases}$$

which results in the following matrices components for i-th element with nodes i and $i+1$:

$$M_{kk}^{(e)} = a_1 \frac{\triangle\xi_i}{3},\ J_{kk}^{(e)} = a_2 \frac{\triangle\xi_i}{3},\ k = 1, 2$$

$$M_{kl}^{(e)} = a_1 \frac{\triangle\xi_i}{6},\ J_{kl}^{(e)} = a_2 \frac{\triangle\xi_i}{6},\ k, l = 1, 2,\ k \neq l$$

$$D_{kk}^{(e)} = a_1 \frac{\triangle \xi_i}{3},\ E_{kk}^{(e)} = a_2 \frac{\triangle \xi_i}{3},\ k = 1, 2$$

$$D_{kl}^{(e)} = a_1 \frac{\triangle \xi_i}{6},\ E_{kl}^{(e)} = a_2 \frac{\triangle \xi_i}{6},\ k, l = 1, 2,\ k \neq l$$

$$K_{kk}^{(e)} = \frac{a_1}{\triangle \xi_i},\ C_{kk}^{(e)} = \frac{a_2}{\triangle \xi_i},\ k = 1, 2$$

$$K_{kl}^{(e)} = \frac{-a_1}{\triangle \xi_i},\ C_{kl}^{(e)} = \frac{-a_2}{\triangle \xi_i},\ k, l = 1, 2,\ k \neq l$$

The Constants a_1, a_2, are equal to unit for elements in DP, or (A_B/A_p and J_B/J_p) for elements in the BHA.

The nodal forces and torques can also be re-written applying the values of weight functions at nodes i and $i+1$ of the i-th element. Applying the values $\psi_1(\xi_i) = \psi_2(\xi_{i+1}) = 1$ and $\psi_1(\xi_{i+1}) = \psi_2(\xi_i) = 0$ in Equations (A.1.13) and (A.1.14), force and torque vectors for the i-th element are written as:

$$F_i = \int_{\xi_i}^{\xi_{i+1}} f \psi_i d\xi + P_i \tag{A.1.15}$$

$$T_i = \int_{\xi_i}^{\xi_{i+1}} f_\varphi \psi_i d\xi + Q_i \tag{A.1.16}$$

Assembling all matrices including the element geometric properties contribution for node n_d (node located at ξ_d representing the transition between drill pipes and drill collars), assuring the continuity conditions. The mass and inertia, and stifinesses matrices, in terms of i-th element length $\triangle \xi_{i-1} = \xi_i - \xi_{i-1}$ are assembled in the following form:

$$\mathbf{M} = \begin{bmatrix} \frac{\triangle \xi_1}{3} & \frac{\triangle \xi_1}{6} & 0 & \ldots & 0 & 0 & 0 \\ \frac{\triangle \xi_1}{6} & \frac{\triangle \xi_1 + \triangle \xi_2}{3} & \frac{\triangle \xi_2}{6} & \ldots & & & \\ & & & \ldots & & & \\ 0 & \ldots & \frac{\triangle \xi_d}{6} & \frac{\triangle \xi_d + a_1 \triangle \xi_{d+1}}{3} & \frac{a_1 \triangle \xi_{d+1}}{6} & \ldots & 0 \\ & & & \ldots & & & \\ & & & \ldots & \frac{\triangle \xi_{n-2}}{6} & \frac{\triangle \xi_{n-2} + \triangle \xi_{n-1}}{3} & \frac{\triangle \xi_{n-1}}{6} \\ & & & \ldots & 0 & \frac{\triangle \xi_{n-1}}{6} & \frac{\triangle \xi_{n-1}}{3} \end{bmatrix} \tag{A.1.17}$$

$$\mathbf{J} = \begin{bmatrix} \frac{\triangle\xi_1}{3} & \frac{\triangle\xi_1}{6} & 0 & ... & 0 & 0 & 0 \\ \frac{\triangle\xi_1}{6} & \frac{\triangle\xi_1+\triangle\xi_2}{3} & \frac{\triangle\xi_2}{6} & ... & & & \\ & \frac{\triangle\xi_2}{6} & & ... & & & \\ 0 & ... & \frac{\triangle\xi_d}{6} & \frac{\triangle\xi_d+a_2\triangle\xi_{d+1}}{3} & \frac{a_2\triangle\xi_{d+1}}{6} & ... & 0 \\ & & & ... & & & \\ & & & ... & \frac{\triangle\xi_{n-2}}{6} & \frac{\triangle\xi_{n-2}+\triangle\xi_{n-1}}{3} & \frac{\triangle\xi_{n-1}}{6} \\ & & & ... & 0 & \frac{\triangle\xi_{n-1}}{6} & \frac{\triangle\xi_{n-1}}{3} \end{bmatrix} \quad \text{(A.1.18)}$$

$$\mathbf{K} = \begin{bmatrix} \frac{1}{\Delta\xi_1} & \frac{-1}{\Delta\xi_1} & 0 & ... & 0 & 0 & 0 \\ \frac{-1}{\Delta\xi_1} & \frac{1}{\Delta\xi_1}+\frac{1}{\Delta\xi_2} & \frac{-1}{\Delta\xi_2} & ... & 0 & 0 & 0 \\ & & & ... & & & \\ 0 & ... & \frac{-1}{\Delta\xi_{d-1}} & \frac{1}{\Delta\xi_{d-1}}+\frac{a_1}{\Delta\xi_d} & -\frac{a_1}{\Delta\xi_d} & ... & 0 \\ & & & ... & & & \\ 0 & 0 & 0 & ... & \frac{-1}{\Delta\xi_{n-2}} & \frac{1}{\Delta\xi_{n-2}}+\frac{1}{\Delta\xi_{n-1}} & \frac{-1}{\Delta\xi_{n-1}} \\ 0 & 0 & 0 & ... & 0 & \frac{-1}{\Delta\xi_{n-1}} & \frac{1}{\Delta\xi_{n-1}} \end{bmatrix} \quad \text{(A.1.19)}$$

$$\mathbf{C} = \begin{bmatrix} \frac{1}{\Delta\xi_1} & \frac{-1}{\Delta\xi_1} & 0 & ... & 0 & 0 & 0 \\ \frac{-1}{\Delta\xi_1} & \frac{1}{\Delta\xi_1}+\frac{1}{\Delta\xi_2} & \frac{-1}{\Delta\xi_2} & & & & \\ & & & ... & & & \\ 0 & ... & \frac{-1}{\Delta\xi_{d-1}} & \frac{1}{\Delta\xi_{d-1}}+\frac{a_2}{\Delta\xi_d} & -\frac{a_2}{\Delta\xi_d} & .... & 0 \\ & & & ... & & & \\ 0 & 0 & 0 & & \frac{-1}{\Delta\xi_{n-2}} & \frac{1}{\Delta\xi_{n-2}}+\frac{1}{\Delta\xi_{n-1}} & \frac{-1}{\Delta\xi_{n-1}} \\ 0 & 0 & 0 & & 0 & \frac{-1}{\Delta\xi_{n-1}} & \frac{1}{\Delta\xi_{n-1}} \end{bmatrix} \quad \text{(A.1.20)}$$

with $a_1 = A_B/A_p$ and $a_2 = J_B/J_p$. One can note that the geometric factors actually affect the equations related to elements connected to node n_d only. It is possible to simplify the inter element boundaries P_i and Q_i to:

$P_i = \frac{\partial u_i}{\partial\xi}\Big|_{\xi_i}^{i-1} + \frac{\partial u_i}{\partial\xi}\Big|_{\xi_i}^{i}$, and $Q_i = \frac{\partial\varphi_i}{\partial\xi}\Big|_{\xi_i}^{i-1} + \frac{\partial\varphi_i}{\partial\xi}\Big|_{\xi_i}^{i}$ for $i = 1, ...n_{d-1}, n_{d+1}, ...N-1$ and,

$$P_i = \left.\frac{\partial u_i}{\partial \xi}\right|_{\xi_i}^{i-1} + a_1 \left.\frac{\partial u_i}{\partial \xi}\right|_{\xi_i}^{i}, \text{ and } Q_i = \left.\frac{\partial \varphi_i}{\partial \xi}\right|_{\xi_i}^{i-1} + a_2 \left.\frac{\partial \varphi_i}{\partial \xi}\right|_{\xi_i}^{i} \text{ for } i = n_d.$$

with subscript $i-1$ and i representing the elements interconnected by the i-th node located at ξ_i.

Appendix B

Lumped Models

B.1 Models Description

This section presents some lumped models used to simulate the drill-string dynamics subjected to bit-rock interface law and different surface BC's. First we assumed that only the drill pipes matters for the drilling dynamics, and was described in Section 5.2. Then the BHA is introduced by means of a lumped mass, with a drive system that damps all axial and torsional waves. Next model considers that only torsional waves are damped, with imposed axial displacement. The last model assumes a lumped model with axial and torsional wave reflection as another delayed term. The time delay is the wave traveling time from bit to the driven system, and coming back to the bit again. The lumped models were named as follow:

- Model I - lumped BHA with drill pipes compliance and perfectly damper at driven system;
- Model II - lumped BHA with drill pipes compliance, and driven system with perfect damper for torsional modes. Imposed constant vertical force as surface axial BC,
- Model III - lumped BHA with drill pipes compliance, with delayed force and torque from surface reflection.

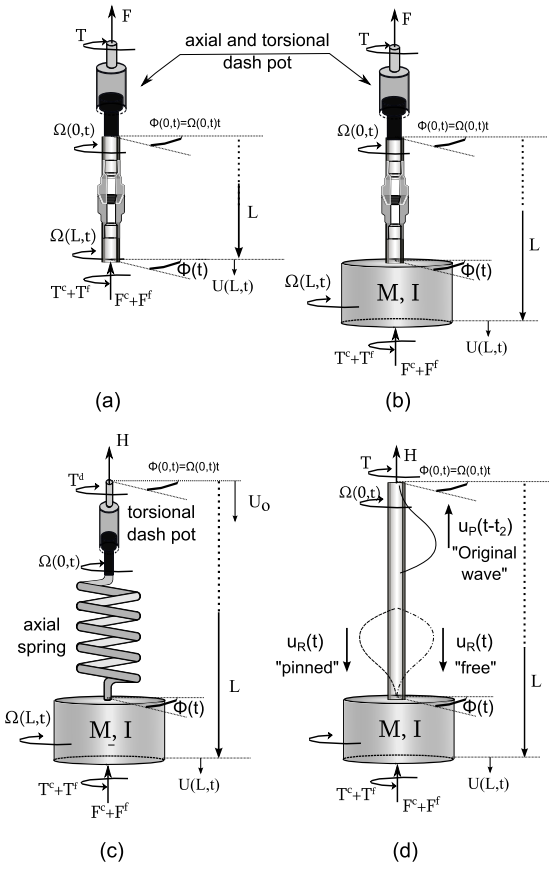

Figure B.1.1: Models: (a) only drill pipes, and (b) lumped BHA with drill pipes, both with perfect damping system at surface, and (c) lumped BHA with axial spring representing the DP and perfect torsional damper at surface, and (d) reflected axial and torsional waves acting over the bit.

B.2 Mathematical models

Herein the models are aimed to simulate the axial and torsional dynamics of the drill pipe, with bit rock interface law acting at the drill pipe lower end. The surface BC simulates a perfect damper, or imposed velocity. The vertical forces acting on the system are: weight and torque on

bit (W and T), the force F_d and torque T_d at the drill pipes. At $x = 0$, these forces and torques must be balanced. *i.e.* $W = \int f_u dx - F_d$ and $T = T_d$, with f_u being the drill pipes self weight per unit length. For the equilibrium solution U_o and Φ_o, torque and forces are constant, and $W_o = \int f_u dx - F_d^o$ and $T_o = T_d^o$. If the drill pipe - dash pot system behaves like a semi-infinite media, we can relate the damping force F and torque T perturbation as follow:

For the model with the lumped mass, we have:

$$M\ddot{U} = -\delta F_d + W_o - \left(W^c + W^f\right), \tag{B.2.1}$$

$$I\ddot{\Phi} = -\delta T_d + T_o - \left(T^c + T^f\right). \tag{B.2.2}$$

and combining Equations (2.4.7), (5.2.1), and (5.2.2) with Equations (5.2.3) and (5.2.4), the resulting equation of motions for dimensionless displacement perturbations are:

$$\epsilon_u \frac{\partial^2 u}{\partial \tau^2} + \vartheta_u \frac{\partial u}{\partial \tau} = -\psi_u n_b \left[u\left(1,\tau\right) - u\left(1,\tau-\tau_1\right) + \upsilon_o \hat{\tau}_1 + \lambda g\left(\upsilon\right)\right], \tag{B.2.3}$$

$$\epsilon_\varphi \frac{\partial^2 \varphi}{\partial \tau^2} + \vartheta_\varphi \frac{\partial \varphi}{\partial \tau} = -\psi_\varphi n_b \left[u\left(1,\tau\right) - u\left(1,\tau-\tau_1\right) + \upsilon_o \hat{\tau}_1 + \lambda\beta g\left(\upsilon\right)\right]. \tag{B.2.4}$$

with $\epsilon_u = Md_*/AEt_*^2$, $\epsilon_\varphi = Id_*/GJt_*^2$, $\psi_u = \zeta\varepsilon a d_*/AE$, $\psi_u \epsilon_u^{-1} = \psi = \zeta\varepsilon a d_*/(MC)$ from [48] and $\psi_\varphi \epsilon_\varphi^{-1} = 1$. For $M \to 0$, Equations (B.2.3) and (B.2.4) become Equations (5.2.5) and (5.2.6).

For the system with an axial spring, only the axial equation of motion change, which writes as $M\ddot{U} = -\Delta H - \left(W^c + W^f - W_o\right)$, with $\Delta H = K_s\left(U - U_o\right)$. The equations of motion are written in the dimensionless axial and torsional displacement perturbations forms:

$$\epsilon_u \frac{\partial^2 u}{\partial t^2} + \kappa u\left(\tau\right) = -\psi_u n_b \left[u\left(1,\tau\right) - u\left(1,\tau-\tau_1\right) + \upsilon_o \hat{\tau}_1 + \lambda g\left(\upsilon\right)\right], \tag{B.2.5}$$

$$\epsilon_\varphi \frac{\partial^2 \varphi}{\partial \tau^2} + \vartheta_\varphi \frac{\partial \varphi}{\partial \tau} = -\psi_\varphi n_b \left[u\left(1,\tau\right) - u\left(1,\tau-\tau_1\right) + \upsilon_o \hat{\tau}_1 + \lambda\beta g\left(\upsilon\right)\right]. \tag{B.2.6}$$

where Equation (B.2.6) was written only for the sake of system completeness, with $\kappa = d_*/L$, and κ/ϵ_u representing the scaled drill pipes compliance.

The last model considers that the axial and torsional waves of perturbations are reflected at the surface, but there overall shape does not change because there is no dissipation. It means that Equations (5.2.1) and (5.2.2) holds. The nature of the wave of perturbations reflection depends on the type of the BC. Axial BC must respect $\partial u\left(0,t\right)/\partial\xi = 0$ for imposed constant

hook load H_o, or $u(0,t) = 0$ for constant axial velocity v_o. Torsional BC was always assumed such that wave reflection must respect$\varphi(0,t) = 0$. Figure depicts the reflected shape of a triangular wave facing both BC.

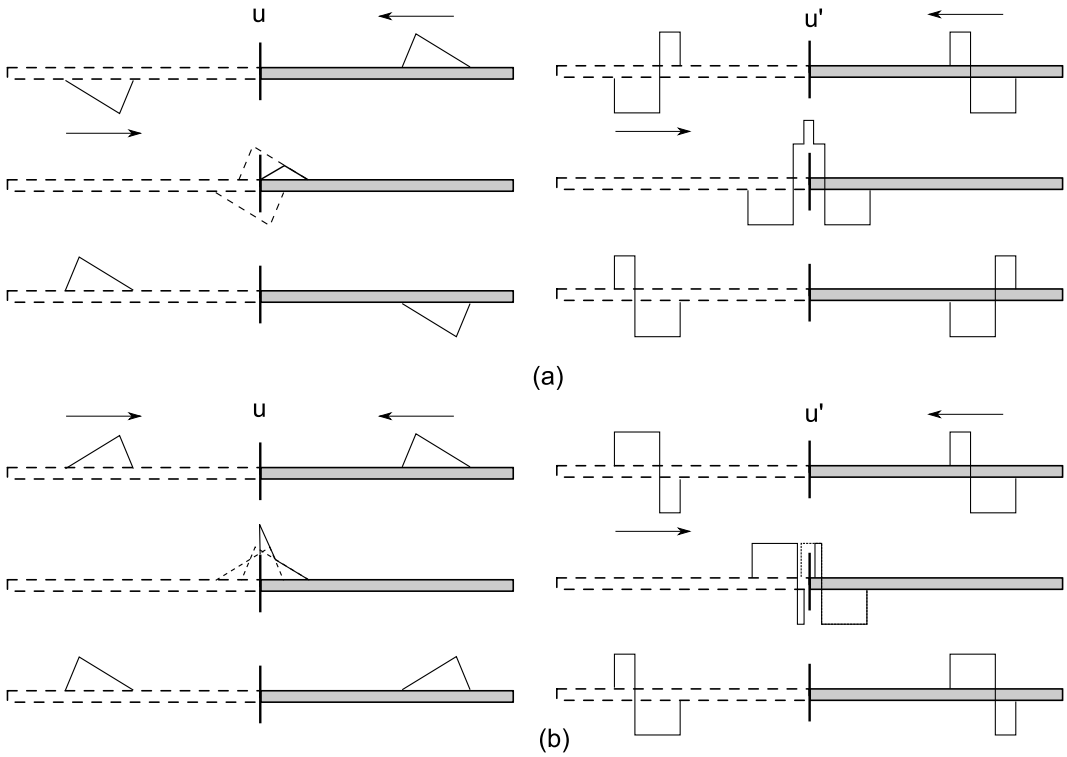

Figure B.2.1: Wave reflection pattern for (a) fixed type BC, and (b) free type BC. Since there is no dissipation the wave shape remains the same, changing only the orientation depending on the assumed BC.

The time taken for axial and torsional waves to get the bit are different, due to difference in wave propagation speeds c_u and c_ϕ. Then the coupled model introduces two additional time delays, namely τ_2 and τ_3. The first one reflects the time taken for the axial wave of perturbations traveling, and the second reflects the torsional one. The time delays are constant for a given

drilling depth, and written in the following form:

$$\tau_2 = \frac{2L_d}{c_u t_*},\ \tau_3 = \frac{2L_d}{c_\phi t_*}.$$

and the equations of motions reads:

$$\epsilon_u \frac{\partial^2 u}{\partial \tau^2} + \vartheta_u \frac{\partial u(\tau - \tau_2)}{\partial \tau} = -\psi_u n_b \left[u(1,\tau) - u(1,\tau-\tau_1) + \upsilon_o \hat{\tau}_1 + \lambda g(\upsilon) \right], \tag{B.2.7}$$

$$\epsilon_\varphi \frac{\partial^2 \varphi}{\partial \tau^2} + \vartheta_\varphi \frac{\partial \varphi(\tau - \tau_3)}{\partial \tau} = -\psi_\varphi n_b \left[u(1,\tau) - u(1,\tau-\tau_1) + \upsilon_o \hat{\tau}_1 + \lambda \beta g(\upsilon) \right]. \tag{B.2.8}$$

This system is equivalent to the system described by Equations (B.2.3) and (B.2.4). In the previous case, since there is no reflections, the damping force acts (like) instantaneously, while in the latter there is a time delay related to the wave propagation. Before the waves are able to hit the bit back, there is no applied force, therefore $\partial u(L,\tau)/\partial \xi = 0$ for $\tau < \tau_2$ and $\partial \varphi(L,\tau)/\partial \xi = 0$ for $\tau < \tau_3$.

B.3 Lumped models linear stability

Following the linearization process described in Section 5.2, the linearized models are written as:

Model I

$$\epsilon_u \frac{\partial^2 u}{\partial \tau^2} + \vartheta_u \frac{\partial u}{\partial \tau} = -\psi_u n_b \left[u(1,\tau) - u(1,\tau-\tau_1) + \alpha_o \varphi(1,\tau-\tau_1) - \alpha_o \varphi(1,\tau) \right], \tag{B.3.1}$$

$$\epsilon_\varphi \frac{\partial^2 \varphi}{\partial \tau^2} + \vartheta_\varphi \frac{\partial \varphi}{\partial \tau} = -\psi_\varphi n_b \left[u(1,\tau) - u(1,\tau-\tau_1) + \alpha_o \varphi(1,\tau-\tau_1) - \alpha_o \varphi(1,\tau) \right]. \tag{B.3.2}$$

Model II

$$\epsilon_u \frac{\partial^2 u}{\partial t^2} + \kappa u(\tau) = -\psi n_b \left[u(1,\tau) - u(1,\tau-\tau_1) + \alpha_o \varphi(1,\tau-\tau_1) - \alpha_o \varphi(1,\tau) \right], \tag{B.3.3}$$

$$\epsilon_\varphi \frac{\partial^2 \varphi}{\partial \tau^2} + \vartheta_\varphi \frac{\partial \varphi}{\partial \tau} = -\psi_\varphi n_b \left[u(1,\tau) - u(1,\tau-\tau_1) + \alpha_o \varphi(1,\tau-\tau_1) - \alpha_o \varphi(1,\tau) \right]. \tag{B.3.4}$$

Model III

$$\epsilon_u \frac{\partial^2 u}{\partial \tau^2} + \vartheta_u \frac{\partial u(\tau - \tau_2)}{\partial \tau} = -\psi_u n_b \left[u(1,\tau) - u(1,\tau-\tau_1) + \alpha_o \varphi(1,\tau-\tau_1) - \alpha_o \varphi(1,\tau) \right], \tag{B.3.5}$$

$$\epsilon_\varphi \frac{\partial^2 \varphi}{\partial \tau^2} + \vartheta_\varphi \frac{\partial \varphi(\tau - \tau_3)}{\partial \tau} = -\psi_\varphi n_b \left[u(1,\tau) - u(1,\tau-\tau_1) + \alpha_o \varphi(1,\tau-\tau_1) - \alpha_o \varphi(1,\tau) \right]. \tag{B.3.6}$$

Following the numerical approach described in Chapter 3, the stability charts for models II and III are presented below in the parameter space υ_o-ω_o. Model IV did not present any stable region, revealing that the inclusion of the time delay into damping like terms $\partial u\left(\tau-\tau_2\right)/\partial\tau$ and $\partial\varphi\left(\tau-\tau_3\right)/\partial\tau$ resulted in a fully unstable system, for both imposed surface axial BC (constant force or constant velocity).

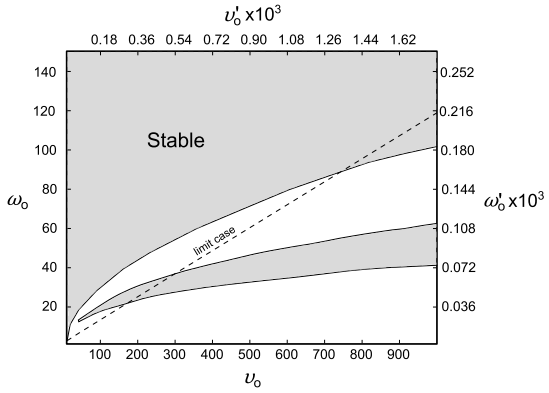

Figure B.3.1: Stability charts for: (a) lumped model II, and (b) lumped model III in space parameter $\nu_o-\omega_o$ $(\nu_o'-\omega_o')$.

Appendix C

Pontrjagin criteria for DDE stability

C.1 2DOF System

Consider that the characteristic equation is described by the transcendental equation $H(x) = h(x, e^x)$ and that $h(x, z)$ is a polynomial. The principal term of $h(x, z) = \sum_{m,n} a_{mn} x^m z^n$ is defined as $a_{rs} x^r z^s$ if $a_{rs} \neq 0$ and the exponents r and s attain their maximum [45]. Therefore r and s are such that for all other terms $a_{mn} x^m z^n$ we have one of the following conditions:

i.$r > m$ and $s > n$, or

ii.$r = m$ and $s > n$, or

iii.$r > m$ and $s = n$.

For example $h(x, z) = x^3 z + x^2 z + xz + x^2 + 1$ presents principal term with $a_{rs} = 1$, $r = 3$, and $s = 1$, with r and s corresponding to the maximum m and n exponents respectively. But $h(x, z) = x^3 + x^2 z + x^2 + 1$ does not present a principal term.

We can rewrite $H(iy) = F(y) + iG(y)$, $y \in \mathbb{R}$. If $H(x)$ has principal term then all roots of $H(x)$ have negative real part if the following conditions are satisfied [45] (herein called Pontryagin conditions):

1. All zeros of $F(y)$ (or $G(y)$) are real, and;

2. For every zero of $F(y)$ (or $G(y)$) , $F'(y) G(y) < 0$ (or $F(y) G'(y) > 0$) holds.

The necessary and sufficient conditions that the function $F(y)$ (or $G(y)$) present only real roots is that in the interval $-2k\pi+\epsilon \leq y \leq 2k\pi+\epsilon$, $F(y)$ (or $G(y)$) has exactly $4sk+r$ zeros, starting with sufficiently large k.

For 2-DOF system under consideration, the polynomial $h(x,z)$ reads:

$$\begin{aligned} h(x,z) &= x^4 z + \left[\frac{\alpha}{(1-\epsilon)^2} + \frac{\alpha}{\epsilon^2} + \frac{\alpha}{(1-\epsilon)\epsilon} + \frac{b_o}{1-\epsilon}\right] x^2 z + \\ &+ \left[\frac{\alpha^2}{(1-\epsilon)^2\epsilon^2} + \frac{\alpha b_o}{(1-\epsilon)^2\epsilon} + \frac{\alpha b_o}{(1-\epsilon)\epsilon^2}\right] z + \\ &- \frac{b_o}{1-\epsilon} x^2 - \frac{\alpha b_o}{(1-\epsilon)\epsilon^2} - \frac{\alpha b_o}{(1-\epsilon)^2\epsilon}, \end{aligned}$$

which present a principal term with $r=4$ and $s=1$. The function $G(y)$ now writes $G(y) = g_1(y)\sin(y)$. The function $g_1(y)$ is a forth order polynomial. First let's assume that $g_1(y)$ has four distinct roots (see Equation (C.1.1)). If these roots y_i, $i=1,2,3,4$ are such that $y_i \neq \ell\pi$, $\ell = 0, \pm1, \pm2, \pm3..$, then $G(y) = g_1(y)\sin(y)$ can present $4k+4$ zeros within $-2k\pi+\epsilon \leq y \leq 2k\pi+\epsilon$ with appropriated choice of ϵ, and all zeros of $G(y)$ are real. Then we have to study the properties of the function $g_1(y)$, which is written as:

$$\begin{aligned} g_1(y) &= y^4 - \left(\frac{\alpha}{(1-\epsilon)^2} + \frac{\alpha}{\epsilon^2} + \frac{\alpha}{(1-\epsilon)\epsilon} + \frac{b_o}{1-\epsilon}\right) y^2 + \frac{\alpha^2}{(1-\epsilon)^2\epsilon^2} + \\ &+ \frac{\alpha b_o}{(1-\epsilon)\epsilon^2} + \frac{\alpha b_o}{(1-\epsilon)^2\epsilon} \end{aligned} \qquad \text{(C.1.1)}$$

and can be rewritten as $\left(y^2 + c/2\right)^2 = (c/2)^2 - e$. Therefore the roots of $g_1(y)$ are defined by:

$$y_i = \pm\sqrt{-\frac{c}{2} \pm \sqrt{\left(\frac{c}{2}\right)^2 - e}} \qquad i = 1,2,3,4$$

If $(c/2)^2 - e > 0$, for $e > 0$ we have $|c/2| > \sqrt{(c/2)^2 - e}$. The sufficient condition for that $g_1(y)$ presents four real and distinct roots is then that the polynomial $D = (c/2)^2 - e > 0$, given that $c < 0$. The term D for some discrete ϵ values ($\epsilon = 0.05$, 0.02 and 0.5), named as D_i, $i=1,2,3$ for increasing ϵ reads:

$$\begin{aligned} D_1 &= 44111.7\alpha^2 - 221.023\alpha b_o + 0.277008 b_o^2 \\ D_2 &= 230.103\alpha^2 - 18.5547\alpha b_o + 0.390625 b_o^2 \\ D_3 &= 20.\alpha^2 - 4.\alpha b_o + b_o^2 \end{aligned}$$

The parameters α and b_o are $\mathcal{O}\left(10^0 - 10^2\right)$ and $\mathcal{O}\left(10^0 - 10^1\right)$, respectively. With these parameters D_i are always positive. Then $g_1(y)$ has four real and distinct roots and Pontryagin condition I holds.

Another Approach First we introduce the discriminant Δ (see [23]) which is defined as the product of the squared roots difference, *i.e.*

$$\Delta = (y_1 - y_2)^2 (y_1 - y_3)^2 (y_1 - y_4)^2 (y_2 - y_3)^2 (y_2 - y_4)^2 (y_3 - y_4)^2 .$$

For a general quartic equation on the form $ay^4 + by^3 + cy^2 + dy + e$, if $\Delta > 0$, all roots are distinct. They also real if $P = 8a \cdot c - 3b^2$ and $D = 64a^3e - 16a^2c^2 + 16ab^2c - 16a^2bd - 3b^4$ are negative. The discriminant Δ can be written as:

$$\Delta = -4p^3 - 27q^2,\ p = -\frac{c^2}{3} + bd - 4e,\ q = -\frac{2c^3}{27} + \frac{bcd}{3} - d^2 - b^2e + \frac{8ce}{3}$$

The $g_1(y) = y^4 + cy^2 + e$ discriminant Δ and polynomials P and D are written as:

$$\begin{aligned} \Delta(g_1) &= 256e^3 - 128c^2e^2 + 16c^4 \cdot e \\ P &= 8c \\ D &= 64e - 16c^2 \end{aligned}$$

The polynomial P is always negative ($c < 0$). Also note that the polynomial D is the same as before, but with opposite sign. Therefore we are going to look for $\triangle$ and D behavior for some discrete ϵ values ($\epsilon = 0.01, 0.2$, and 0.5), named as Δ_i, D_i, $i = 1, 2, 3$ for increasing ϵ:

$$\begin{aligned} \Delta_1 &= 1.69878 \times 10^{21}\alpha^6 + 1.6981 \times 10^{21}\alpha^5 b_o - 6.79475 \times 10^{17}\alpha^4 b_o^2 + \\ &\quad +1.0194 \times 10^{14}\alpha^3 b_o^3 - 6.79695 \times 10^9 \alpha^2 b_o^4 + 169945.\alpha b_o^5 \\ D_1 &= -1.63216 \times 10^9 \alpha^2 + 326464.\alpha b_o - 16.3249 b_o^2 \end{aligned}$$

$$\begin{aligned} \Delta_2 &= 1.69878 \times 10^{21}\alpha^6 + 1.6981 \times 10^{21}\alpha^5 b_o - 6.79475 \times 10^{17}\alpha^4 b_o^2 + \\ &\quad +1.0194 \times 10^{14}\alpha^3 b_o^3 - 6.79695 \times 10^9 \alpha^2 b_o^4 + 169945.\alpha b_o^5 \\ D_2 &= -14726.6\alpha^2 + 1187.5\alpha b_o - 25.b_o^2 \end{aligned}$$

$$\begin{aligned}\Delta_3 &= 5.29472\times10^8\alpha^6 + 4.44082\times10^8\alpha^5 b_o - 8.01492\times10^7\alpha^4 b_o^2 + \\ &\quad +5.09548\times10^6\alpha^3 b_o^3 - 143433.\alpha^2 b_o^4 + 1525.88\alpha b_o^5 \\ D_3 &= -1280.\alpha^2 + 256.\alpha b_o - 64.b_o^2\end{aligned}$$

The parameters α and b_o are $\mathcal{O}\left(10^0 - 10^2\right)$ and $\mathcal{O}\left(10^0 - 10^1\right)$ respectively. With these parameters Δ_i are always positive and D_i are always negative; $g_1(y)$ has four real and distinct roots and Pontryagin condition I holds. Therefore, to look for the system stability, we just have to find regions in the parametric space that condition II also holds.

C.2 3DOF System

For 3-DOF system under consideration, the polynomial $h(x,z)$ reads:

$$\begin{aligned}h(x,z) = \; & -x^6 z + \frac{x^4 z a_o}{(1-2\epsilon)^2} + \frac{4x^4 z a_o}{\epsilon^2} - \frac{3x^2 z a_o^2}{\epsilon^4} - \frac{4x^2 z a_o^2}{(1-2\epsilon)^2\epsilon^2} + \frac{x^2 z a_o^2}{(1-2\epsilon)^3\epsilon} \\ & + \frac{3z a_o^3}{(1-2\epsilon)^2\epsilon^4} - \frac{2z a_o^3}{(1-2\epsilon)^3\epsilon^3} - \frac{x^4 z b_o}{(1-2\epsilon)^2} - \frac{x^4 b_o}{1-2\epsilon} + \frac{x^4 z b_o}{1-2\epsilon} + \\ & - \frac{4x^4 z b_o}{\epsilon^2} + \frac{6x^2 z a_o b_o}{\epsilon^4} + \frac{8x^2 z a_o b_o}{(1-2\epsilon)^2\epsilon^2} + \frac{4x^2 a_o b_o}{(1-2\epsilon)\epsilon^2} - \frac{4x^2 z a_o b_o}{(1-2\epsilon)\epsilon^2} - \\ & \frac{2x^2 z a_o b_o}{(1-2\epsilon)^3\epsilon} - \frac{9z a_o^2 b_o}{(1-2\epsilon)^2\epsilon^4} - \frac{3a_o^2 b_o}{(1-2\epsilon)\epsilon^4} + \frac{3z a_o^2 b_o}{(1-2\epsilon)\epsilon^4} + \frac{6z a_o^2 b_o}{(1-2\epsilon)^3\epsilon^3} + \\ & - \frac{3x^2 z b_o^2}{\epsilon^4} - \frac{4x^2 z b_o^2}{(1-2\epsilon)^2\epsilon^2} - \frac{4x^2 b_o^2}{(1-2\epsilon)\epsilon^2} + \frac{4x^2 z b_o^2}{(1-2\epsilon)\epsilon^2} + \frac{x^2 z b_o^2}{(1-2\epsilon)^3\epsilon} + \\ & + \frac{9z a_o b_o^2}{(1-2\epsilon)^2\epsilon^4} + \frac{6a_o b_o^2}{(1-2\epsilon)\epsilon^4} - \frac{6z a_o b_o^2}{(1-2\epsilon)\epsilon^4} - \frac{6z a_o b_o^2}{(1-2\epsilon)^3\epsilon^3} - \frac{3z b_o^3}{(1-2\epsilon)^2\epsilon^4} + \\ & - \frac{3b_o^3}{(1-2\epsilon)\epsilon^4} + \frac{3z b_o^3}{(1-2\epsilon)\epsilon^4} + \frac{2z b_o^3}{(1-2\epsilon)^3\epsilon^3}\end{aligned}$$

Function $G(y)$ reads:

$$G(y) = -\left(y^4 - \frac{4y^2 a_o}{\epsilon^2} + \frac{3a_o^2}{\epsilon^4} + \frac{4y^2 b_o}{\epsilon^2} - \frac{6a_o b_o}{\epsilon^4} + \frac{3b_o^2}{\epsilon^4}\right)\frac{\sin(y)\, b_o}{1-2\epsilon}$$

We note that we have a more complicated fourth order function that we need to study the roots. Hence, for 3-DOF system, the D-Curves were used, with numerical evaluation of the eigenvalues, to establish the system stability.

Appendix D

Drilling system properties data

D.1 Drilling Data Description

This section shows the main parameter defining the drilling system studied in Chapter 3 and (to be added chapter). Drill pipes and BHA characteristic range lengths are shown in Table D.1.1 . In Chapter 3 the maximum lengths were used ($L_b = 200$ m and $L_d = 1000$ m).

Parameter	Quantity	unity
L_b	$[100, 200]$	m
L_d	$[200, 1000]$	m
R_b	0.0762	m
r_b	0.0286	m
A_b	0.0156	m^2
J_b	5.19×10^{-5}	m^4
I_b	41.5	$kg.m^2$
M_b	12541	kg
R_d	0.0635	m
r_d	0.053975	m
A_d	0.00351	m^2
J_d	1.22×10^{-5}	m^4
a	0.10795	m
W_o	1.5×10^4	N
Ω_o	12.57	rad/s
C	4700	$N.m$
ε	60	GPa
σ_f	60	GPa
ℓ	3	$mm/blade$
t_*	0.3	s
d_*	2.66	mm
W_*	5.22×10^4	N
T_*	$2.82E+03$	$N.m$
ζ	0.6	
γ	1	
μ	0.6	

Table D.1.1: Drilling system properties used within this thesis.